LBNL-40451
UC-404

ERNEST ORLANDO LAWRENCE
BERKELEY NATIONAL LABORATORY

Hydrogen Local Vibrational Modes in Semiconductors

Matthew D. McCluskey
Materials Sciences Division

June 1997
Ph.D. Thesis

LBNL-40451
UC-404

Hydrogen Local Vibrational Modes in Semiconductors

Matthew Douglas McCluskey

Department of Physics
University of California, Berkeley

and

Center for Advanced Materials
Materials Sciences Division
Ernest Orlando Lawrence Berkeley National Laboratory
University of California
Berkeley, California 94720

Ph.D. Thesis

June 1997

This work was supported by US NSF grant DMR-94 17763 and in part by the Director, Office of Energy Research, Office of Basic Energy Sciences, Materials Sciences Division, of the U.S. Department of Energy under Contract No. DE-AC03-76SF00098.

Hydrogen Local Vibrational Modes in Semiconductors

by

Matthew Douglas McCluskey

Abstract

Hydrogen Local Vibrational Modes in Semiconductors

by

Matthew Douglas McCluskey

Doctor of Philosophy in Physics

University of California, Berkeley

Professor Eugene E. Haller, Cochair

Professor Peter Y. Yu, Cochair

Following a review of experimental techniques, theory, and previous work, the results of local vibrational mode (LVM) spectroscopy on hydrogen-related complexes in several different semiconductors are discussed. Hydrogen is introduced either by annealing in a hydrogen ambient, exposure to a hydrogen plasma, or during growth. The hydrogen passivates donors and acceptors in semiconductors, forming neutral complexes. When deuterium is substituted for hydrogen, the frequency of the LVM decreases by approximately the square root of two. By varying the temperature and pressure of the samples, the microscopic structures of hydrogen-related complexes are determined.

For group II acceptor-hydrogen complexes in GaAs, InP, and GaP, hydrogen binds to the host anion in a bond-centered orientation, along the [111] direction, adjacent

to the acceptor. The temperature dependent shift of the LVMs are proportional to the lattice thermal energy *U(T)*, a consequence of anharmonic coupling between the LVM and acoustical phonons. In the wide band gap semiconductor ZnSe, epilayers grown by metalorganic chemical vapor phase epitaxy (MOCVD) and doped with As form As-H complexes. The hydrogen assumes a bond-centered orientation, adjacent to a host Zn.

In AlSb, the DX centers Se and Te are passivated by hydrogen. The second, third, and fourth harmonics of the wag modes are observed. Although the Se-D complex has only one stretch mode, the Se-H stretch mode splits into three peaks. The anomalous splitting is explained by a new interaction between the stretch LVM and multi-phonon modes of the lattice. As the temperature or pressure is varied, an anti-crossing is observed between the LVM and phonon modes.

Table of Contents

List of Figures

Acknowledgments

Writing this thesis has reminded me how much I have relied on the expertise and generous help of dozens of people. At the top of the list is my advisor, Prof. Eugene Haller, whose enthusiastic guidance, no-nonsense scientific approach, and excellent editing skills have tremendously benefited my research experience. I also thank my co-advisors, the late Prof. Leo Falicov and Prof. Peter Yu, for sharing their insights into solid state physics. The many hours spent talking (and guffawing) with Dr. Wladek Walukiewicz were especially enlightening. I have enjoyed many fruitful collaborations with Dr. Noble Johnson and Jack Walker from Xerox Palo Alto Research Center (PARC) and Dr. Peter Becla (MIT).

In addition to their continual help, the graduate students and post-docs of the Haller group have provided endless lunch-time entertainment (sometimes at my expense)! Among the many graduate students whom I would like to thank, Leonardo Hsu receives highest honors for cheerfully fixing my mistakes and bailing me out on innumerable occasions. I have benefited from helpful discussions with O. Dubon, W. Knowlton, and J. Wolk, as well as J. Beeman, who among other things constructed the Ge:Cu photoconductor. J. Krüger and G. Elliot supplied GaAs and GaP samples, respectively. Our secretary, David Hom, has provided efficient help with a healthy dose of humor. I would also like to thank Prof. Peter Berck (Dept. of Agricultural and Resource Economics) for helping out when my hard drive decided to take early retirement.

I would like to thank my parents, John and Linda, for their love and encouragement. Finally, I thank my wife, Jill, for her unconditional love and for bringing our daughter, Lauren Jennifer, into the world on Feb. 12, 1997. Before then, I learned the truth behind the saying, "Some days you're the Louisville slugger, and some days you're the ball." Whatever the day, I'll always know that Jill and Lauren are the two most important people in the world.

Although I have benefited from the careful scrutiny of my thesis committee, all errors contained herein are mine.

This work was supported in part by USNSF grant DMR-94 17763 and in part by the Director, Office of Energy Research, Office of Basic Energy Sciences, Materials Science Division of the U.S. Department of Energy under Contract No. DE-AC03-76SF00098.

1. Introduction

Since the invention of the transistor in 1949, the integrated circuit in 1959, and the subsequent growth of the semiconductor industry (Braun and MacDonald, 1978), a great deal of research has focused on the physics of semiconductors. The ability to manipulate the conductivity of these materials over more than fifteen orders of magnitude through controlled doping has made them indispensable in electronics applications (Seeger, 1989). Impurities and structural defects drastically affect the electrical and optical properties of semiconductors, both beneficially and detrimentally. In this thesis, I will concentrate on hydrogen-related defects.

A semiconductor crystal such as silicon is composed of atoms arranged in a periodic lattice, with covalent bonds between neighboring atoms. A specific minimum amount of energy is required to excite a valence electron out of the *valence band* and into the *conduction band*, where the electron can move freely and carry current. The "missing electron" in the otherwise filled valence band is called a *hole* and has a positive charge. Analogous to an electron, a hole can move freely in the valence band. The minimum energy difference between the conduction and valence bands is known as the *band gap*, and for silicon it is 1.1 eV. At room temperature, only a small fraction of the intrinsic electrons (holes) are in the conduction (valence) band, so an intrinsic semiconductor is semi-insulating. The band gap of an intrinsic semiconductor may be determined by measuring the thermal population of electrons (holes) in the conduction (valence) band as a function of temperature. An Arrhenius plot of the logarithm of the free carrier concentration yields the band gap energy. The band gap may also be measured by optical absorption, in which a photon excites an electron into the conduction band. The band gaps of semiconductors such as germanium (Newman and Tyler, 1959) and GaAs (Moss and Hawkins, 1962) have been measured in this way.

The band structure of a solid arises from the periodicity of the atomic potentials in the lattice. According to Bloch's theorem, the translational symmetry of a lattice leads to electronic wavefunctions that have a well-defined wavevector $\mathbf{k}$ (Yu and Cardona, 1996). In all diamond and zincblende semiconductors, the valence band maximum occurs at $\mathbf{k} = 0$ (Kittel and Mitchell, 1954). If the conduction band minimum also occurs at $\mathbf{k} = 0$, then the semiconductor has a *direct* band gap. Otherwise, the band gap is *indirect*. A simple model of a one-dimensional periodic potential was offered by Kronig and Penney (1930). The Kronig-Penney model consists of an infinite series of square wells and yields allowed and forbidden energy bands that depend on the height and spacing of the wells.

Detailed band structure calculations have been performed for semiconductors using the tight-binding, or linear combination of atomic orbitals (LCAO) approach (Chadi and Cohen, 1975). Alternatively, the orthogonalized plane wave (OPW) method uses a plane-wave basis set, with the atomic core electron wavefunctions subtracted from the plane waves (Herring 1940). The pseudopotential model (Cohen and Heine, 1976) replaces the rapidly varying part of the wavefunction near the nucleus with a smooth function. The theory of *ab initio* pseudopotentials was developed (Louie *et al.*, 1977; Starkoff and Joannopoulos, 1977; Zunger and Cohen, 1978; Hamann *et al.*, 1979; Kerker 1980) to model, from first principles, the interaction of the valence electron with the core electrons.

Introducing impurities into a semiconductor can increase the free electron or hole concentration. A donor such as phosphorus in silicon has one more valence electron than the silicon atom that it replaces. The additional electron is bound to the positively charged phosphorus ion, forming a hydrogenic system. In the case of phosphorus in silicon, the electron binding energy is 45 meV, which is sufficiently low such that practically all the electrons are ionized into the conduction band at room temperature. An impurity such as boron has one less valence electron than silicon, so it is an acceptor. The hole is bound to the negatively charged B ion and it can be excited into the valence band.

Hydrogenic impurities are described well by the effective mass theory (Luttinger and Kohn, 1955; Kohn 1957). In a direct gap semiconductor, the energy of an electron in the conduction band is approximated by

$$E = E_{CBM} + \hbar^2 k^2 / 2m^*, \tag{1.1}$$

where E_{CBM} is the conduction band minimum and m^* is the effective electron mass. In general, the effective mass of an electron or hole is inversely proportional to the curvature of the conduction or valence band. If an electron is bound to a donor, it forms a hydrogenic system, with the electron wavefunction centered around the positively charged donor. The binding energy is given by

$$E_B = 13.6 \text{ eV } (m^*/m_e\varepsilon^2) \qquad (1.2)$$

and the effective Bohr radius is given by

$$a_0 = 0.5 \text{ Å } (\varepsilon\, m_e / m^*), \qquad (1.3)$$

where ε is the spatially averaged dielectric constant, m_e is the free-space electron mass, and m^* is the effective mass defined in Eq. 1.1. Since $\varepsilon \gg 1$ and $m^* < m_e$ in most diamond and zincblende semiconductors, the effective Bohr radius is typically much larger than 0.5 Å. In GaAs, for example, $m^* = 0.066\ m_e$ and $\varepsilon = 12.5$, yielding effective mass theory values of $a_0 = 95$ Å and $E_B = 5.7$ meV (Kohn 1957; Lanno and Bourgoin, 1981). The large radius means that the electron wavefunction samples many atoms, thereby justifying the use of a uniform dielectric constant.

The addition of impurities to a semiconductor introduces energy levels into the band gap. For donors, this impurity level is below the conduction band by an amount equal to the binding energy E_B. For acceptors, the level is above the valence band by E_B. Doping a pure semiconductor with acceptors or donors makes the semiconductor p- or n-type, respectively. As discussed in Sec. 1.1, hydrogen is a particularly important impurity because it neutralizes, or *passivates*, donor and acceptor levels. The impurity levels are removed from the band gap.

In addition to altering the electronic properties of semiconductors, impurities such as hydrogen can also affect the vibrational properties. As discussed in Sec. 2.2, atoms in a crystalline solid can collectively oscillate about their equilibrium positions, resulting in quantized vibrational modes called *phonons*. Einstein (1907) first treated the problem of phonons by assuming that the atoms in a solid vibrate independently of one another. Debye (1912) improved upon the Einstein model by treating a solid as an elastic continuum. The Debye approximation is good for long wavelength phonons but it breaks down as the wavelength approaches the lattice spacing. To remedy this situation, an arbitrary cut-off frequency is introduced (Sec. 2.2.3). The cut-off frequency is typically expressed as a temperature and is known as the *Debye temperature*. The Debye temperatures for numerous cubic crystals have been measured by Betts, Bhatia, and Wyman (1956).

As in the case of electrons in a perfect lattice, phonons in a perfect lattice have a well-defined wavevector q. The ω vs. q dispersion relation can be experimentally determined via neutron scattering (Brockhouse and Iyengar, 1958). When an impurity is introduced, the translational symmetry is broken and one or more new vibrational modes may appear. If a mass defect replaces a heavier host atom, for example, its vibrational frequency will lie above the phonon frequency range. As discussed in Sec. 2.3, the vibrational mode of the defect is localized in real space and frequency space, and is referred to as a *local vibrational mode* (LVM). Hydrogen, with its low mass, typically has LVM frequencies 5-10 times the maximum phonon frequency and has narrow infrared absorption peaks (Sec. 2.4).

In the following sections, I discuss hydrogen passivation and the microscopic structure of impurity-hydrogen complexes. In addition, I briefly describe the methods of hydrogenation that I used in this study.

1.1 Hydrogen Passivation

In germanium, hydrogen has been found to activate the isoelectronic impurities C and Si (Sec. 1.2). Hydrogen is also important because it neutralizes, or *passivates*, electrically active impurities by supplying the additional electron needed to complete the Lewis octet. In hydrogen passivation, the impurity level is removed from the band gap, resulting in a decrease in the free carrier concentration. In addition, since neutral complexes are formed, the decrease in ionized impurity scattering increases the mobility. Passivation is not the same as compensation. The latter results in a decrease in both the free carrier concentration and the mobility. Hydrogen passivation has both beneficial and detrimental effects. Hydrogen passivation of deep levels increases the minority carrier lifetime. However, the omnipresence of hydrogen in growth processes can hinder reliable p- or n-type doping of semiconductors.

The passivation process is shown schematically Figure 1.1 for the case of Si:B. The hydrogen acts as a donor, its electron annihilating a free hole (b). The proton feels the Coulomb attraction of the negatively ionized boron acceptor. As will be explained in Sec. 1.3.1, the hydrogen assumes a bond-centered orientation, between a silicon and boron, forming a neutral complex. The electrostatic energy is minimized when the proton sits in the covalent bond.

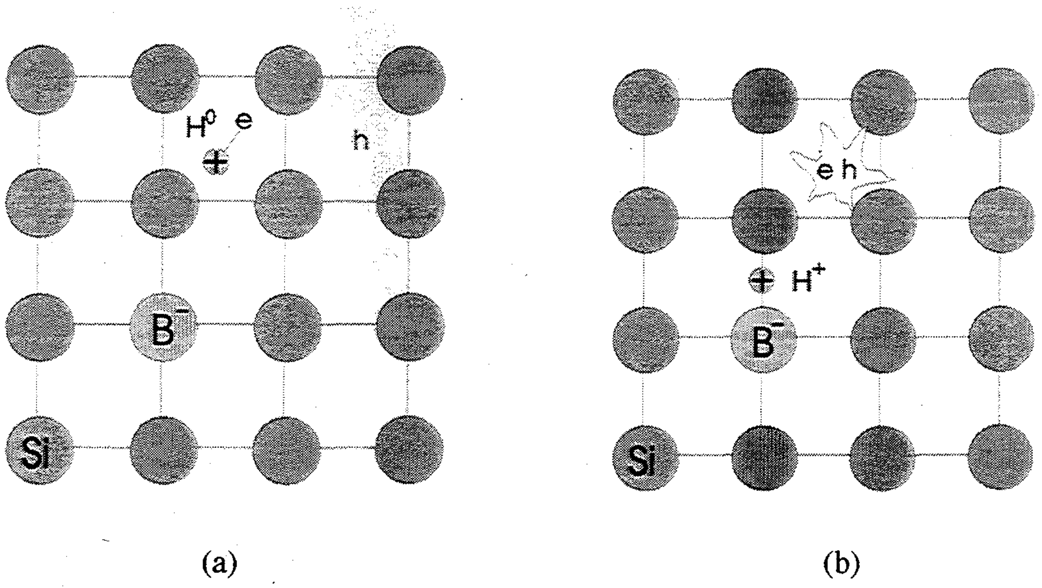

Figure 1.1. Hydrogen passivation of p-type silicon.

In the case of an n-type semiconductor such as Si:P, the hydrogen acts as an acceptor (Figure 1.2). An electron in the conduction band (a) ionizes the hydrogen, forming H^- (b). Then, the H^- feels the Coulomb attraction of the positively ionized phosphorus donor. The hydrogen assumes an anti-bonding orientation (c), attached to a silicon in a direction opposite to the donor (Sec. 1.3.3). The bond-centered orientation is energetically unfavorable because the electrostatic repulsion of the electrons is too high.

To summarize, hydrogen is an amphoteric defect that can passivate donors as well as acceptors. The formation of neutral complexes occurs by *compensation followed by passivation*.

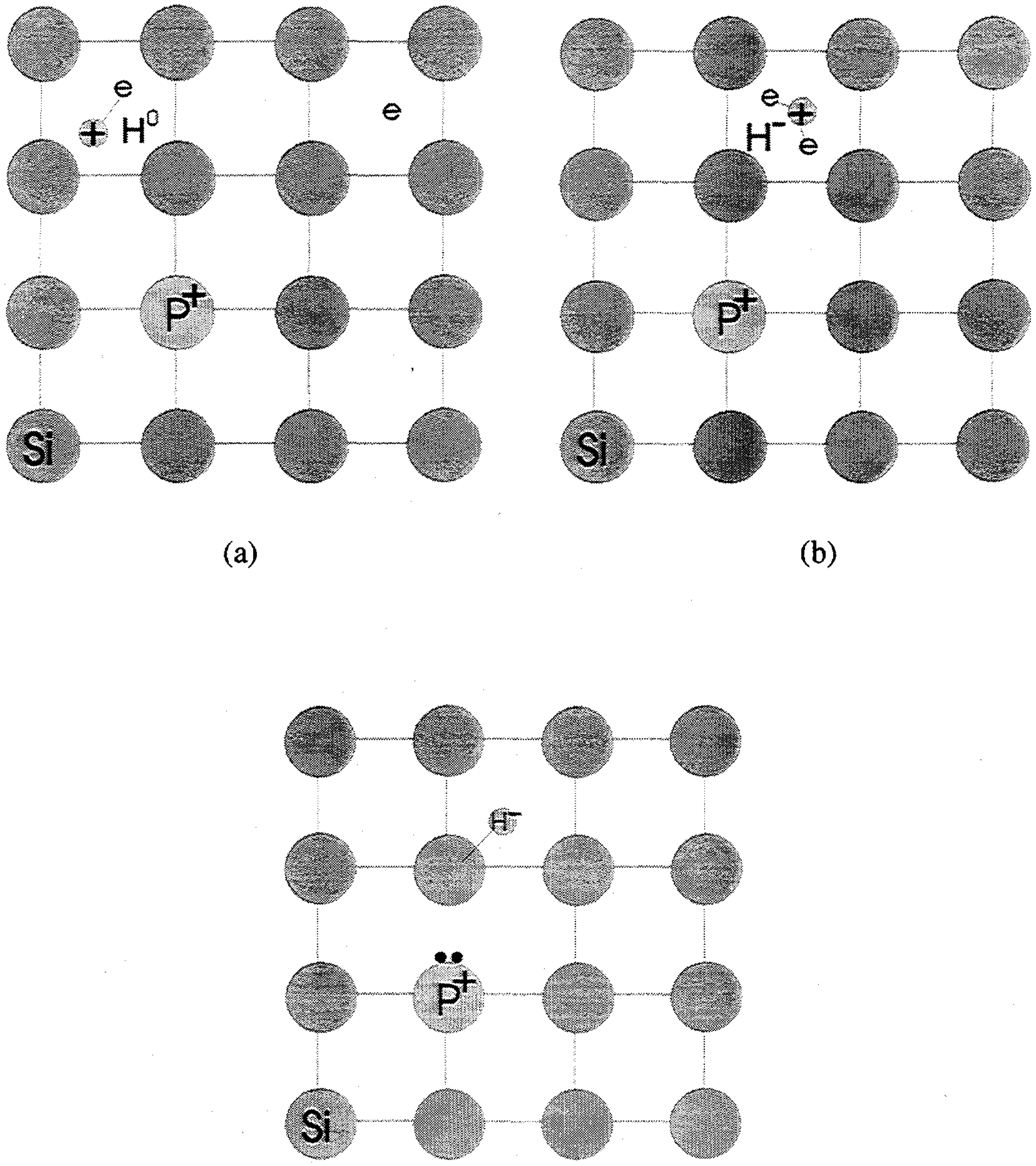

(a)

(b)

(c)

Figure 1.2. Hydrogen passivation of n-type silicon.

1.2 Hydrogen in Germanium

Hydrogen plays many interesting roles in crystalline semiconductors. Hydrogen-related centers were first discovered and studied in ultra-pure Ge (Haller and Hansen 1974, Haller 1978) which was grown for use in radiation detectors. During Ge crystal growth, ambient hydrogen saturates the Ge melt in the crucible and enters the bulk as atomic hydrogen. It passivates electrically active defects and impurities, especially deep level centers, resulting in improved mobility and minority carrier lifetime.

The first hydrogen-related complexes that were discovered, however, were electrically active (Haller 1991). Hydrogen was found to activate the neutral isoelectronic impurities silicon (Hall 1974; Haller *et al.*, 1980), carbon (Haller *et al.*, 1980), and interstitial bond-centered oxygen (Haller 1978; Joós *et al.*, 1980). The concentration of electrically active hydrogen-related complexes in ultra-pure Ge is as low as 10^{11} cm^{-3}. The only way to study such low concentrations is with photothermal ionization spectroscopy (PTIS) (Lifshits and Nad, 1965; Haller *et al.*, 1974, 1975; Kogan and Lifshits, 1977). In PTIS, an incoming photon promotes a dopant-bound electron or hole from the ground state to a bound excited state. Bound excited states in pure semiconductors have lifetimes which are sufficiently long for the carrier to be thermally ionized into the nearest band at temperatures between 6 - 10 K. When the electron (hole) has reached the conduction (valence) band, an applied bias produces a current. The current is plotted as a function of photon wave numbers, yielding a spectrum of the excited states of the complex. PTIS has the advantages that it is highly selective and sensitive.

Using PTIS, Kahn *et al.* (1987) determined from ground state splitting that the Si-H and C-H acceptor complexes have trigonal C_{3v} symmetry, with the hydrogen oriented along a [111] crystallographic axis. In the O-H donor complex, tunneling of the hydrogen between equivalent [111] sites results in a complicated manifold of 1s states. Upon substitution of deuterium for hydrogen, the O-H and Si-H ground states shift downward by 51 μeV and 21 μeV, respectively. The isotope shift was the first conclusive evidence that these complexes are hydrogen-related.

The double acceptors Be and Zn, and the triple acceptor Cu, are partially passivated by hydrogen. The Be-H and Zn-H complexes are shallow acceptors with binding energies of 11.29 and 12.53 meV, respectively, with C_{3v} symmetry (Haller *et al.*, 1977; McMurray *et al.*, 1987; Kahn *et al.*, 1987). The lowering of the symmetry from T_d to C_{3v} leads to a splitting of the ground state. Cu binds two hydrogen atoms and is also a shallow acceptor with a binding energy of 17.81 meV (Kahn *et al.*, 1986). Like the O-H complex, the Cu-H_2 complex exhibits hydrogen tunneling that splits the 1s state into a broad manifold of states. In Ge:Cu samples grown in a deuterium ambient, a Cu-D_2 complex is found, with a binding energy of 18.20 meV. The heavier mass hinders tunneling so the 1s state does not broaden as in the Cu-H_2 complex. When Ge:Cu samples are grown in an ambient of hydrogen *and* deuterium, a new set of transition lines appears, corresponding to a Cu-HD complex with a binding energy of 18.10 meV (Haller *et al.*, 1977). In general, the appearance of new electronic or vibrational peaks in a sample exposed to hydrogen and deuterium is a strong indicator of a multi-hydrogen complex.

1.3 Hydrogen in Silicon

1.3.1 Acceptor-Hydrogen Complexes

The semiconductor industry became very interested in hydrogen when it was found by Sah *et al.* (1983) that hydrogen neutralizes boron acceptors in silicon. They demonstrated that hydrogen from water-related molecular species in the oxide layer in metal-oxide-semiconductor (MOS) capacitors diffuses into the silicon and passivates the acceptors. Spreading resistance profiles of silicon samples exposed to a hydrogen plasma show that the boron acceptors are neutralized to a depth of 1-2 μm (Pankove *et al.*, 1984). When the samples are annealed at temperatures above 200°C, the boron-hydrogen complexes dissociate and the resistivities decrease to the as-grown values. Johnson (1985) used secondary ion mass spectrometry (SIMS) to measure the concentration profile of deuterium and boron in Si:B exposed to a deuterium plasma. The deuterium and boron concentrations are nearly identical to a depth of 0.6 μm, suggesting the presence of B-D pairs.

Compelling evidence for boron-hydrogen complexes came from the infrared spectra of hydrogenated Si:B samples. In addition to a reduction in the free carrier absorption, Pankove *et al.* (1985) discovered an infrared absorption peak at 1870 cm^{-1} in Si:B samples exposed to a hydrogen plasma. Upon substitution of deuterium for hydrogen, the peak shifts to a frequency of 1360 cm^{-1} (Johnson 1985). The isotopic frequency ratio is $r = \nu_H/\nu_D = 1.375$, which is close to the square root of the reduced mass ratio (Sec. 2.3.3) of 1.395 expected for the bond-stretching mode of a diatomic Si-H molecule.

Using cluster methods, DeLeo and Fowler (1985) found that the total energy of the B-H complex is a minimum when the hydrogen is oriented along the [111] axis in a bond-centered configuration (Figure 1.3). To test this model, Stavola *et al.* measured the local vibrational modes (LVMs) of the acceptor-hydrogen complexes B-H, Al-H, and Ga-H at liquid helium temperatures to be 1907, 2201, and 2171 cm^{-1}, respectively. The vibrational frequencies are fairly close to the predicted values.

The bond-centered model received further support when Pajot *et al.* (1988) discovered that the B-H LVM frequency increases by 0.8 cm^{-1} when ^{10}B is substituted for ^{11}B, in agreement with theoretical calculations (Estreicher *et al.*, 1989) that predicted a weak B-H bond. The B-D mode shifts by 3.3 cm^{-1} when ^{10}B is substituted for ^{11}B, over four times the shift of the B-H mode. The unusual shift of the B-D mode can be explained by a Fermi resonance, as explained below.

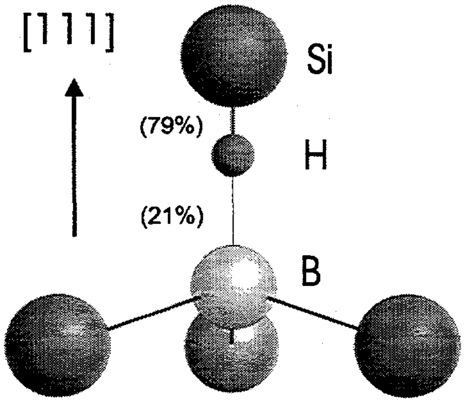

Figure 1.3. Bond centered model for acceptor-hydrogen complexes in silicon. The distribution of the bond between B-H and Si-H is shown (Estreicher *et al.*, 1989).

1.3.2 Fermi Resonance of B-H in Si

In addition to the B-H bond-stretching mode, the boron atom can oscillate transversely, with an LVM frequency of 652 or 680 cm^{-1} for ^{11}B or ^{10}B, respectively (Herrero and Stutzmann, 1988). The second harmonic of the ^{10}B mode is nearly degenerate with the D stretch mode. The two modes interact anharmonically and repel each other, so that the D stretch mode is pushed upward in frequency. The second harmonic of the ^{11}B mode is further from the D stretch mode, so the interaction is weaker. The H stretch mode, in contrast, is not degenerate with any modes, so the boron isotope shift is not enhanced by a Fermi resonance. The Fermi resonance was found by Watkins *et al.* (1990), who observed the ^{10}B and ^{11}B second harmonics near the D stretch modes. The anharmonic interaction between the B and D modes causes mode mixing which results in an increased intensity of the B modes.

1.3.3 Donor-Hydrogen Complexes

Passivation of donors in silicon was first demonstrated by Johnson *et al.* (1986), who showed that exposing an n-type layer of silicon to a hydrogen plasma at 150°C reduces the free carrier concentration and increases the mobility. The increase in the mobility is due to a decrease in ionized impurity scattering. The authors presented semiempirical calculations which predicted that the hydrogen attaches to a silicon atom in a [111] antibonding orientation. In contrast to the bond-centered model, the hydrogen in the antibonding orientation sits opposite to the donor. (Figure 1.4) Subsequent theoretical calculations agreed with the antibonding model (Chang and Chadi, 1988; Amore-Bonapasta *et al.*, 1989; Estreicher *et al.*, 1989; DeLeo and Fowler, 1989).

To test this model, silicon samples were implanted with the donors P, As, or Sb and exposed to a hydrogen or deuterium plasma for 6 hr at a temperature of 120°C (Bergman *et al.*, 1988). Hydrogen stretch modes were observed near 1500 cm^{-1} and wag modes at 809 cm^{-1}. The deuterium stretch and wag modes shift downward in frequency by a factors of 1.37 and 1.39, respectively. The frequencies are very insensitive to the donor species - the stretch and wag modes shift less than 10 and 1 cm^{-1}, respectively, from P to Sb. This insensitivity to the donor species is strong evidence in favor of the antibonding model, in which the hydrogen is well isolated from the donor.

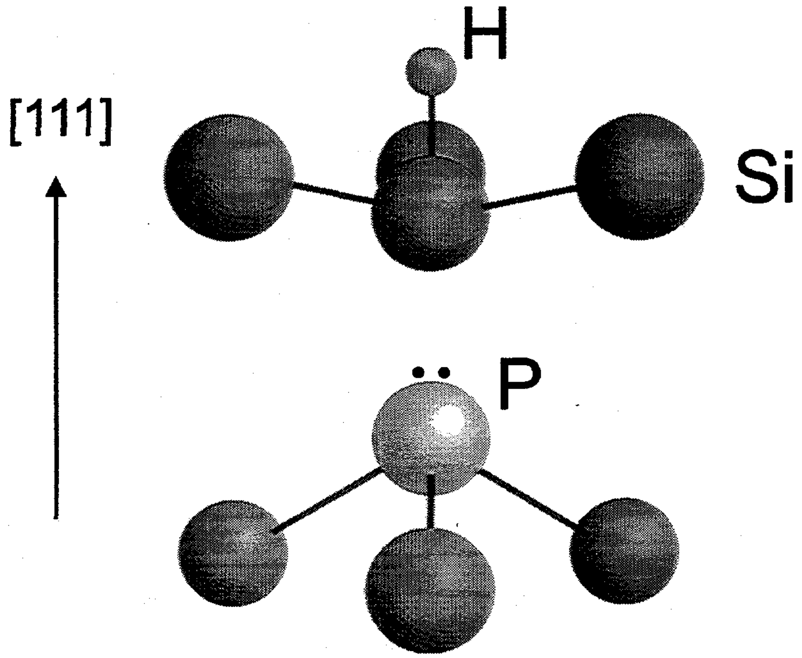

Figure 1.4. Antibonding model for donor-hydrogen complexes in silicon.

It has recently been pointed out that in these donor-hydrogen complexes, there exists a Fermi resonance between the second harmonic wag mode and the stretch mode (Zheng and Stavola, 1996). The second harmonic wag mode anharmonically interacts with the stretch mode. Since they are nearly degenerate, they split into modes which are linear combinations of a wag and a stretch. This is similar to the Fermi resonance in the B-D mode described in Sec. 1.3.2. In Chapter 5, I describe a new kind of resonant interaction, between a Se-H stretch mode and a multi-phonon mode in AlSb.

1.4 Hydrogen in GaAs and InP

Since the discovery of hydrogen passivation of acceptors (Johnson *et al.*, 1985) and donors (Chevallier *et al.*, 1991) in GaAs, a great deal of research has been done on hydrogen in compound semiconductors. In hydrogenated n-type GaAs:Si, Pajot *et al.* (1988) observed infrared absorption peaks at 896.8 and 1717.2 cm^{-1}, corresponding to hydrogen wag and stretch modes, respectively. The ^{29}Si-H stretch frequency was found to be 0.64 cm^{-1} lower than the ^{28}Si-H stretch frequency, providing strong evidence that the hydrogen attaches directly to the silicon donor.

Infrared absorption measurements by Pajot *et al.* (1987) and Nandra *et al.* (1988) provided direct evidence for acceptor-hydrogen complexes in GaAs:Zn and GaAs:Be, respectively. An LVM peak was found in GaAs:Zn,H at 2145.0 cm^{-1}, a frequency similar to the As-H bond-stretching mode in AsH_3 (2116 cm^{-1}) (Shimanouchi 1972) but different from ZnH (1553 cm^{-1}) (Rosen 1970). The hydrogen is therefore believed to bind to the host arsenic. As in the case of acceptor-hydrogen complexes in silicon, the frequency shifts by ~100 cm^{-1} when the acceptor is changed, indicating a bond-centered orientation (Rahbi 1993). Additional evidence for the bond-centered model was provided by uniaxial stress measurements which demonstrated unambiguously that the GaAs:Be,H complex has C_{3v} symmetry.

Epitaxial layers of GaAs:C exposed to a hydrogen or deuterium plasma have stretch modes at 2635.2 and 1968.6 cm^{-1}, respectively, for an isotopic frequency ratio r = 1.3386 (Clerjaud *et al.*, 1990). The small r value is caused in part by the small mass of the carbon atom (Sec. 2.3.3). Replacing ^{12}C with ^{13}C results in a shift to lower frequency, indicating that the hydrogen attaches directly to the carbon acceptor. The ^{12}C complex has four modes, corresponding to combinations of longitudinal and transverse oscillations of hydrogen and carbon (Woodhouse *et al.*, 1993). For the isotopic combinations ^{12}C-H, ^{13}C-H, ^{12}C-D, and ^{13}C-D, there are sixteen modes, all of which have been observed experimentally (Davidson *et al.*, 1993).

In p-type InP exposed to a hydrogen or deuterium plasma, group II acceptor-hydrogen complexes were observed by Darwich *et al.* (1993). As in the case of GaAs, the hydrogen attaches to the host anion (P) in a bond-centered orientation. By measuring the overtones of the stretch modes and fitting the results to a Morse potential (Sec. 2.3.4), they found that as the impurity mass increased from Be to Cd, the anharmonicity decreased. The reduction in anharmonicity accounts at least in part for the increase in the isotopic frequency ratio r.

In Sec. 4.1 I extend the studies of acceptor-hydrogen complexes to GaP. The trends in LVM frequencies and *r* values are discussed, as well as the temperature dependent behavior of the vibrational modes.

1.5 Methods of Hydrogenation

Hydrogen can be introduced into a sample by boiling in water, electrolysis, implantation, exposure to a hydrogen plasma, or contamination during the growth process (Haller 1994). In general, the omnipresence of hydrogen makes contamination with the "simplest element" difficult to avoid. In Sec. 4.2, I discuss arsenic-hydrogen complexes in ZnSe:As grown by metalorganic chemical phase epitaxy (MOCVD), in which the hydrogen originates from the metalorganic molecules and the carrier gas. To obtain acceptor-hydrogen complexes in GaP, a hydrogen plasma was used (Sec. 4.1). Finally, in Sec. 4.3, I discuss annealing in a hydrogen ambient as a method of bulk passivation in AlSb. In the following two sections, I describe the methods of hydrogen plasma exposure and hydrogen annealing.

1.5.1 Annealing in Hydrogen

One of the simplest ways to introduce hydrogen into a semiconductor is to heat the sample in the presence of hydrogen gas. The sample is typically sealed in a quartz ampoule with H_2 and annealed in a vertical furnace. After completion of the annealing, the ampoule is rapidly quenched to room temperature by dropping it in ethylene glycol. Hydrogen annealing at a temperature of 1200°C was shown to passivate acceptors in silicon by Veloarisoa *et al.* (1991), but hydrogen annealing did not passivate donors. In AlSb, Se and Te donors were passivated by annealing in H_2 and D_2 for temperatures as low as 700°C (Chapter 4.3).

When an H_2 molecule hits the surface of a semiconductor, it can dissociate into two hydrogen atoms:

$$\mathrm{H}_2 \leftrightarrow 2\mathrm{H} \tag{1.4}$$

The law of mass action (Reif 1965) states

$$\frac{n_{\mathrm{H}_2}}{n_{\mathrm{H}}^{\ 2}} = k(T,V) \tag{1.5}$$

where n_{H_2} and n_{H} are the concentrations of molecular and atomic hydrogen, respectively. As discussed in Sec. 1.6, H_2 molecules are extremely immobile in semiconductors so they cannot diffuse. Atomic hydrogen, however, can diffuse quite rapidly. The concentration of atomic hydrogen is given by

$$n_{\mathrm{H}} = \sqrt{\frac{n_{\mathrm{H}_2}}{k(T,V)}}. \tag{1.6}$$

For a given temperature, therefore, the solubility of atomic hydrogen is proportional to the square root of the H_2 pressure. The solubility and transport of hydrogen in silicon was studied in detail by van Wieringen and Warmoltz (1956). The relation (Eq. 1.3) was recently shown experimentally for the case of hydrogen in p-type silicon (McQuaid *et al.*, 1993).

Annealing in hydrogen is an excellent method of introducing hydrogen into bulk semiconductors such as Si and AlSb. In many semiconductors, however, annealing is not an effective method of hydrogen passivation, since the solubility of hydrogen is too low and/or the hydrogen- related complexes are unstable at the annealing temperatures.

1.5.2 Plasma Exposure

Exposure to a hydrogen plasma is common method of introducing atomic hydrogen into semiconductors to a depth of a few microns. The first hydrogen plasmas used for semiconductor passivation were produced in glow discharge tubes (Boening 1982), in which a dc bias of several hundred volts is applied between a metal anode and the sample, which acts as the cathode. Energetic electrons ionize hydrogen molecules and the resultant protons travel toward the sample with a steady current of several mA. A disadvantage of this simple technique is that the protons impinge on the sample surface with an energies of several hundred eV, resulting in significant bombardment damage.

If an alternating electric field is used, however, the protons arrive at the surface with energies of only a few eV. The sample is typically located downstream from the radio frequency plasma to minimize charged particle bombardment damage. In a remote hydrogen plasma system (Johnson 1991), shown in Figure 1.5, hydrogen (or deuterium) and trace amounts of oxygen flow into the microwave cavity. Oxygen is used to suppress hydrogen recombination on the chamber walls, thereby increasing the fraction of atomic hydrogen (Kaufman 1969). The pressure in the chamber is kept at 2 Torr and the flow rates for the H_2 and O_2 are 50 and 0.3 sccm, respectively. The right-angle bends in the silica tube isolate the sample from UV radiation and charged particles.

Exposure to the low energy ions and neutral atoms introduces a subsurface layer of hydrogen which diffuses into the semiconductor. The concentration of the hydrogen near the surface depends on the hydrogen flux, surface absorption, diffusion rate, and the rate of recombination and desorption into H_2.

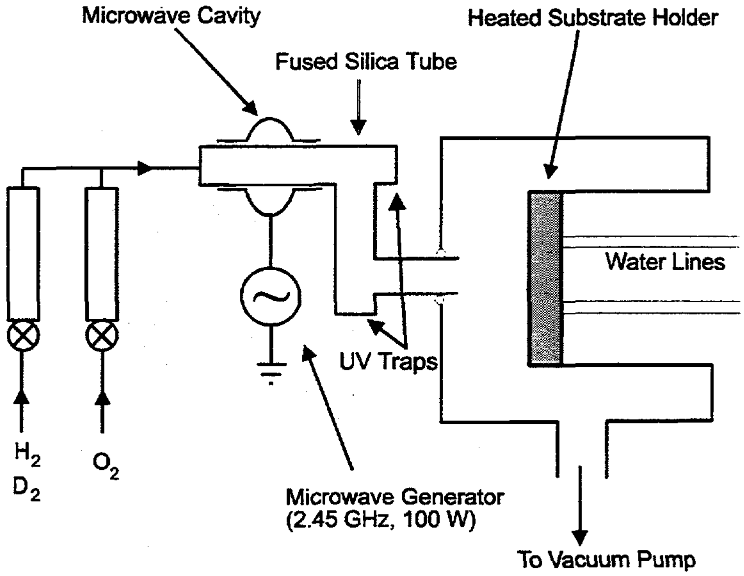

Figure 1.5. Schematic diagram of a remote hydrogen plasma system (from Johnson 1991).

1.6 Hydrogen Diffusion

Isolated hydrogen has been found to be an amphoteric impurity in several semiconductors. It diffuses interstitially as H^+, H^0, or H^-, depending on the position of the Fermi level. In p-type Si, for example, the isolated hydrogen atoms give up their electrons to the acceptors and diffuse as protons. They then feel the Coulomb attraction of the negatively charged acceptors and form neutral complexes. Since the protons repel each other, they do not recombine to form H_2. In n-type Si, the situation is reversed: diffusing H^- atoms form neutral complexes with positively charged donors. The discovery of donor passivation was delayed because H^- can more easily recombine to form H_2, which becomes immobile in the lattice.

In Si, hydrogen is believed to be a "negative-U" center (Johnson *et al.*, 1995): the $H^{0/+}$ donor level lies above the $H^{0/-}$ acceptor level. In their study of the formation of carbon-hydrogen complexes in GaAs, Clerjaud *et al.* (1990) determined the $H^{0/+}$ level to be $E_V + 0.5$ eV. In p-type GaAs, therefore, hydrogen atoms diffuse as protons, whereas in n-type GaAs, they diffuse as a mixture of H^o and H^-.

The positively charged hydrogen species in GaAs:Zn was observed in reverse bias annealing experiments (Tavendale, 1990). After the GaAs:Zn samples were passivated by a deuterium plasma, an aluminum Shottky barrier was evaporated onto the front face. Then, a reverse bias was applied while the samples were annealed at temperatures around 150°C. SIMS measurements and net dopant profiles show that the deuterium drifts out of the depletion region, along the direction of the applied electric field. It was thereby determined that at least some of the thermally dissociated deuterium atoms are positively charged.

The negative charge state of hydrogen was similarly measured in GaAs:Te (Yuan, 1991), GaAs:Se (Leitch, 1991), and GaAs:Si (Cho, 1991). The dissociation of donor-hydrogen complexes was shown to follow first-order kinetics. To accurately determine the dissociation energies and attempt frequencies, it is important to apply a reverse bias which can sweep the free hydrogen atoms out of the depletion region. If this is not done, the negatively (positively) charged hydrogen ions will readily recombine with the ionized donors (acceptors), leading to a value for the dissociation energy which is artificially high.

Many deuterium diffusion studies have been performed on n-type GaAs:Si. Secondary ion mass spectroscopy (SIMS) is used to measure the concentration of deuterium in the sample. In bulk GaAs:Si exposed to a capacitively coupled deuterium plasma, the deuterium concentration profiles at various temperatures closely follow complementary error functions (erfc). The diffusion coefficient is given by

$$D = D_o \exp\left(-E_A/kT\right), \tag{1.7}$$

where $D_o = 115\ \mathrm{cm/s^2}$ and $E_A = 1.38$ eV (Chevallier *et al.*, 1991).

In p-type compound semiconductors, diffusion studies have been performed on highly doped ($p > 10^{18}\ \mathrm{cm^{-3}}$) GaAs:Zn, GaAs:Si, and InP:Zn. Typically, the deuterium concentration profiles consist of a plateau region, where the deuterium concentration closely matches the acceptor concentration, followed by an abrupt decrease. The diffusion process is dominated by hydrogen trapping on shallow acceptors. An exception to this rule is the case of GaAs:Zn for hydrogenation temperatures above 250°C. The Zn-H complex in GaAs begins to decompose at 210°C, so hydrogen trapping at higher temperatures no longer plays a dominant role in the diffusion process. By way of comparison, the Zn-H complex in InP is stable for temperatures below 275°C.

2. Theory of Vibrational Modes in Semiconductors

2.1 The Harmonic Oscillator

The simple harmonic oscillator describes, to first order, the vibration of an object about a stable equilibrium point. A particle that resides in a local minimum of a potential *V(x)* can oscillate about its equilibrium position $x = 0$. For small deviations from equilibrium, the potential can be expanded in a Taylor series:

$$V(x) = V_0 + \frac{1}{2}\frac{\partial^2 V}{\partial x^2}\bigg|_0 x^2 + \cdots \tag{2.1}$$

where the equilibrium condition means that the first derivative is zero. Since it does not affect the equation of motion, the arbitrary constant V_0 may be set to zero. The harmonic potential is written

$$V(x) = \frac{1}{2}kx^2 \tag{2.2}$$

where

$$k = \frac{\partial^2 V}{\partial x^2}\bigg|_0 . \tag{2.3}$$

For sufficiently small displacements about equilibrium, any arbitrary potential can be approximated to first order as a harmonic potential.

2.1.1 Classical Treatment

Classically, the restoring force is given by

$$F = -dV/dx = -kx, \tag{2.4}$$

which is simply a restatement of Hooke's law. Eq. 2.4 is solved by the function

$$x(t) = A \cos(\omega t + \phi), \tag{2.5}$$

where

$$\omega = \sqrt{k/m} \tag{2.6}$$

and A and ϕ are parameters determined by the initial conditions. This simple harmonic oscillator equation describes a wide range of vibrational systems.

2.1.2 Quantum Mechanical Treatment

The quantum mechanical problem is solved via Schrödinger's equation

$$H\psi = E\psi, \tag{2.7}$$

where E is the energy eigenvalue and the Hamiltonian is given by

$$H = \frac{p^2}{2m} + \frac{1}{2}m\omega^2 x^2, \tag{2.8}$$

where m is the mass of the particle and p and x are the momentum and position operators, respectively. Since this is an eigenvalue equation, there exist a number of solutions in which wavefunctions are associated with specific eigenvalues. Following the treatment given by Gasiorowicz (1974), one can define the following operators

$$a = \sqrt{\frac{m\omega}{2}}x + i\frac{p}{\sqrt{2m\omega}} \tag{2.9}$$

$$a^{+} = \sqrt{\frac{m\omega}{2}}x - i\frac{p}{\sqrt{2m\omega}} \tag{2.10}$$

such that the Hamiltonian (2.8) can be written

$$H = \frac{1}{2}\hbar\omega + \omega a^{+}a \ , \tag{2.11}$$

where the fundamental relation

$$[x, p] = i\hbar \tag{2.12}$$

has been used. The bracketed term is a commutator and is defined by [A,B] = AB - BA. Two commutation relations can immediately be derived,

$$[H,a] = -\hbar\omega a \tag{2.13}$$

$$[H,a^{+}] = \hbar\omega a^{+} \tag{2.14}$$

When Eq. 2.13 acts on a wavefunction ψ, we have

$$Ha\psi - aH\psi = -\hbar\omega a\psi \ , \tag{2.15}$$

and inserting Eq. 2.7,

$$Ha\psi = (E - \hbar\omega)\, a\psi \ . \tag{2.16}$$

Thus, the wavefunction $a\psi$ has an energy eigenvalue that is $\hbar\omega$ less than that of the wavefunction ψ. a is therefore called a *lowering operator*, since it lowers the energy of a given state. It can similarly be shown that a^{+} is a *raising operator*, as it raises the energy of a state by $\hbar\omega$. Since the energy E must be positive, the lowering operator a will reach a limit when it hits the ground state. At the ground state ψ_o,

$$a\psi_o = 0\,. \tag{2.17}$$

The energy of the ground state is then given by

$$H\psi_0 = \left(\tfrac{1}{2}\hbar\omega + \omega\, a^+ a\right)\psi_0 = \tfrac{1}{2}\hbar\omega\psi_0\,. \tag{2.18}$$

Combining this result with the fact that the energy levels are quantized in units of $\hbar\omega$, the energy eigenvalues of a simple harmonic oscillator are given by

$$E = (n+1/2)\,\hbar\omega\,. \tag{2.19}$$

The wavefunctions corresponding to each energy eigenvalue can be derived by solving Schrödinger's equation:

$$\psi_n(x) = N_n H_n(x) e^{-x^2/2}, \tag{2.20}$$

where x is in units of $\sqrt{\hbar / m\omega}$, N_n is a normalization factor given by

$$N_n{}^2 = \frac{1}{2^n n!\sqrt{\pi}}, \tag{2.21}$$

and $H_n(x)$ is a Hermite polynomial, listed in Table 2.1.

Table 2.2. Hermite polynomials

n	$H_n(x)$
0	1
1	$2x$
2	$4x^2 - 2$
3	$8x^3 - 12x$
4	$16x^4 - 48x^2 + 12$
5	$32x^5 - 160x^3 + 120x$
6	$64x^6 - 480x^4 + 720x^2 - 120$

For a three dimensional harmonic oscillator, the Hamiltonian is given by

$$H=\frac{p^2}{2m}+\frac{1}{2}m\left(\omega_x{}^2x^2+\omega_y{}^2y^2+\omega_z{}^2z^2\right). \tag{2.22}$$

The solution is obtained by separating the wavefunction into the three normal coordinates,

$$\psi(x,y,z)=\psi_x(x)\psi_y(y)\psi_z(z)\,, \tag{2.23}$$

where $\psi_x(x)$ refers to the one-dimensional harmonic oscillator wavefunction. The energy eigenvalues of the three dimensional system are then obtained by adding the energies of the normal modes:

$$E=\hbar(n_x\omega_x+n_y\omega_y+n_z\omega_z+3/2)\,. \tag{2.24}$$

2.2 Lattice Vibrations

The constituent atoms of a crystalline solid occupy a set of equilibrium positions. The lattice displacement from a given atom's equilibrium position can be described by the vector $\mathbf{u}_{sl}$, where s labels an atom in the lth unit cell. Following the treatment given in Ziman (1972), the total kinetic energy of the solid is given by

$$\frac{1}{2}\sum_{s,l}M_s\dot{u}_{sl}{}^2\,, \tag{2.25}$$

where M_s is the mass of the sth atom. We assume that the potential energy of the solid is a function of the lattice displacements $\mathbf{u}_{sl}$. The potential energy can be expanded in a Taylor series about the equilibrium positions:

$$V = V_o + \sum_{slj} \frac{\partial V}{\partial u^j_{sl}}\bigg|_o u^j_{sl} + \frac{1}{2} \sum_{ss',ll',jj'} \frac{\partial^2 V}{\partial u^j_{sl} \partial u^{j'}_{s'l'}}\bigg|_o u^j_{sl} u^{j'}_{s'l'} + \cdots , \tag{2.26}$$

where j denotes the coordinates x,y,z. The derivatives are evaluated at the equilibrium positions.

The first term in this series is just a constant which can be neglected. The second term vanishes, since the system is at equilibrium. The third term is the *harmonic term*, which determines most of the vibrational properties of the crystal. Sec. (2.3.4) and Appendix B.2 deal with the effects of higher-order *anharmonic* terms.

To first order, the equations of motion are

$$M_s \ddot{u}^j_{sl} = -\sum_{s'l'j'} G^{jj'}_{sl,s'l'} u^{j'}_{s'l'} \tag{2.27}$$

where

$$G^{jj'}_{sl,s'l'} \equiv \frac{\partial^2 V}{\partial u^j_{sl} \partial u^{j'}_{s'l'}}\bigg|_o . \tag{2.28}$$

The coefficients $G^{jj'}_{sl,s'l'}$ are the components of a second rank Cartesian tensor, denoted $\mathbf{G}_{sl,s'l'}$. Eq. 2.27 can be written in matrix form:

$$M_s \ddot{\mathbf{u}}_{sl} = -\sum_{s'l'} \mathbf{G}_{sl,s'l'} \bullet \mathbf{u}_{s'l'} . \tag{2.29}$$

The translational invariance of the crystal demands that **G** cannot depend on the absolute positions of the lattice vectors l and l', but only on their relative positions. Eq. 2.29 can thus be written

$$M_s \ddot{\mathbf{u}}_{sl} = -\sum_{s'\mathbf{h}} \mathbf{G}_{ss'}(\mathbf{h}) \bullet \mathbf{u}_{s',l+\mathbf{h}} , \tag{2.30}$$

where $\mathbf{h} = \mathbf{l} - \mathbf{l}'$. The tensor $\mathbf{G}_{ss'}(\mathbf{h})$ gives the force on atom s due to the displacement of atom s' in a unit cell whose relative position is given by the vector **h**.

The lattice displacements $\mathbf{u}_{sl}$ which solve this system of equations are plane waves with wavevector **q** and frequency ω:

$$\mathbf{u}_{sl} = \mathbf{u}_{s\mathbf{q}} e^{i(\mathbf{q}\cdot\mathbf{l}-\omega t)} \ . \qquad (2.31)$$

Inserting Eq. 2.31 into Eq. 2.30 yields

$$-\omega^2 M_s \mathbf{u}_{s\mathbf{q}} = -\sum_{s'\mathbf{h}} \left[\mathbf{G}_{ss'}(\mathbf{h})\, e^{i\mathbf{q}\cdot\mathbf{h}} \right] \bullet \mathbf{u}_{s'\mathbf{q}} \, . \qquad (2.32)$$

If we define

$$\mathbf{G}_{ss'}(\mathbf{q}) \equiv \sum_{\mathbf{h}} \mathbf{G}_{ss'}(\mathbf{h})\, e^{i\mathbf{q}\cdot\mathbf{h}} , \qquad (2.33)$$

then Eq. 2.32 can be written

$$\sum_{s'} \left[\mathbf{G}_{ss'}(\mathbf{q}) - M_s \omega^{2} \delta_{ss'} \mathbf{I} \right] \bullet \mathbf{u}_{s'\mathbf{q}} = 0 \ , \qquad (2.34)$$

where **I** is the identity matrix and $\delta_{ss'}$ is the Kronecker delta function. $\mathbf{G}_{ss'}(\mathbf{q})$ is simply the Fourier transform of the force tensor $\mathbf{G}_{ss'}(\mathbf{h})$. This is a set of linear equations, one for each value of s, which can be solved by setting the determinant of the matrix in brackets to zero. The problem has been reduced from a many-body problem to one involving only $3n$ degrees of freedom, where n is the number of atoms in a unit cell. Additional assumptions, presented in the following sections, simplify the problem further.

2.2.1 Linear Chain Model

The simplest model is that of a linear chain of identical atoms which interact only via nearest-neighbor forces. The lattice constant is equal to the interatomic spacing a.

Only one spatial dimension is considered, so all the quantities in Eq. 2.34 are scalars. In addition, since there is one atom per unit cell, the subscripts *s* and *s'* can be dropped. We are left with the following:

$$\left[G(q) - M\omega^{2}\right] u = 0 \ . \tag{2.35}$$

The *n*th atom in the linear chain experiences forces from its two nearest neighbors, *n*-1 and *n*+1. The sum of the forces is

$$\begin{aligned} F &= k\left(u_{n+1} - u_{n}\right) + k\left(u_{n-1} - u_{n}\right) \\ &= k\left(u_{n+1} + u_{n-1} - 2u_{n}\right) \end{aligned} \ , \tag{2.36}$$

where *k* is the force constant. From this expression, the components of the force tensor can be derived:

$$G(h) = \begin{cases} 2k & h = 0 \\ -k & h = \pm a \\ 0 & \text{otherwise} \end{cases} \ . \tag{2.37}$$

Inserting this into Eq. 2.33 yields

$$\begin{aligned} G(q) &= k\left(2 - e^{iqa} - e^{-iqa}\right) \\ &= 2k\left[1 - \cos(qa)\right] \\ &= 4k \sin^{2}\left(qa/2\right) \end{aligned} \tag{2.38}$$

Finally, inserting Eq. 2.38 into Eq.2.35 yields the dispersion relation

$$\omega = 2\sqrt{\frac{k}{M}} \sin\left(qa/2\right) \ , \tag{2.39}$$

where the positive root is assumed without loss of generality (Figure 2.1). Because the atoms occupy discrete positions, a phonon wavelength of *a* is equivalent to *a*/2, *a*/3, etc. The range of wavevectors necessary to describe all the phonon modes is called the first

Brillouin zone. It the case of a linear chain, the first Brillouin zone consists of $|q| < \pi/a$. Wavevectors beyond the Brillouin zone edge can be "folded" back into the first Brillouin zone.

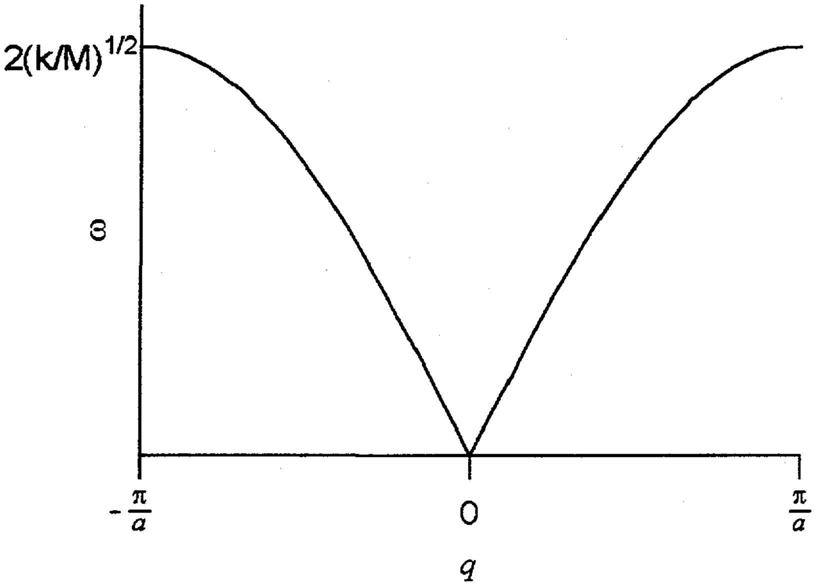

Figure 2.1. Dispersion relation in the first Brillouin zone for a monatomic linear chain.

2.2.2 Diatomic Linear Chain

A slightly more complicated system is a linear chain of atoms with alternating masses M_1 and M_2. Since there are two atoms per unit cell, the subscripts s and s' can each take on two values. The interatomic distance is $a/2$, the lattice constant is a, and atoms experience nearest-neighbor interactions with a force constant k. As in the previous case, only one spatial dimension is considered, so all the quantities in Eq. 2.34 are scalars:

$$\sum_{s'=1}^{2}\left[G_{ss'}(q)-M_s\omega^2\delta_{ss'}\right]u_{s'q}=0\ . \tag{2.40}$$

This is a set of two linear equations, corresponding to s=1 and s=2:

$$\begin{bmatrix} G_{11}(q)-M_1\omega^2 & G_{12}(q) \\ G_{21}(q) & G_{22}(q)-M_2\omega^2 \end{bmatrix}\begin{bmatrix} u_{1q} \\ u_{2q} \end{bmatrix}=0\ . \tag{2.41}$$

To evaluate the components of the force tensor $G_{ss'}$, we write down the forces acting on atoms 1 and 2 which are in the nth unit cell,

$$\begin{aligned} F_1 &= k\left(u_{2,n-1}+u_{2,n}-2u_{1,n}\right) \\ F_2 &= k\left(u_{1,n}+u_{1,n+1}-2u_{2,n}\right) \end{aligned}\ , \tag{2.42}$$

from which we obtain

$$\begin{aligned} &G_{11}(q)=2k \\ &G_{22}(q)=2k \\ &G_{12}(q)=-k\left(e^{-iqa}+1\right) \\ &G_{21}(q)=-k\left(e^{iqa}+1\right) \end{aligned} \tag{2.43}$$

To solve the set of linear equations 2.41, we set the determinant of the matrix equal to zero

$$\begin{vmatrix} 2k-M_1\omega^2 & -k\left(e^{-iqa}+1\right) \\ -k\left(e^{iqa}+1\right) & 2k-M_2\omega^2 \end{vmatrix}=0 \tag{2.44}$$

and solve the resultant quadratic equation

$$M_1M_2\omega^4-2k\left(M_1+M_2\right)\omega^2+2k^2\left[1-\cos(qa)\right]=0 \tag{2.45}$$

$$\Rightarrow \omega^2=k\left(\frac{1}{M_1}+\frac{1}{M_2}\right)\pm k\sqrt{\left(\frac{1}{M_1}+\frac{1}{M_2}\right)^2-\frac{4}{M_1M_2}\sin^2\left(qa/2\right)}\ . \tag{2.46}$$

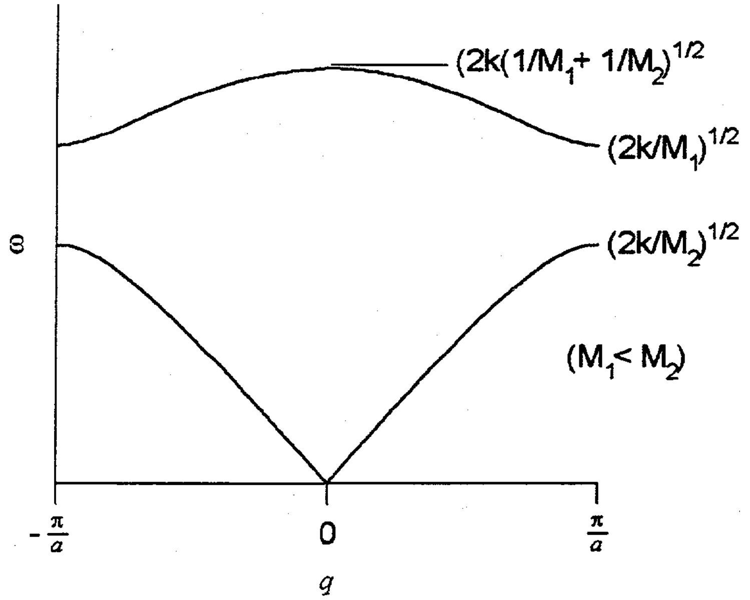

Figure 2.2. Dispersion relation in the first Brillouin zone for a diatomic linear chain. In this diagram, $M_2 = 2M_1$.

For each value of q, there are two values of ω. The two branches are plotted in Figure 2.2 for the first Brillouin zone. It is instructive to evaluate this expression for the center of the Brillouin zone, $q = 0$. The $\sin(qa/2)$ term vanishes and we have

$$\omega = 0, \sqrt{2k\left(\frac{1}{M_1}+\frac{1}{M_2}\right)}. \tag{2.47}$$

The normal mode eigenvector (u_{10}, u_{20}) can be obtained by inserting the corresponding frequency into Eq. 2.41. For the $\omega = 0$ case,

$$\begin{bmatrix} 2k & -2k \\ -2k & 2k \end{bmatrix}\begin{bmatrix} u_{10} \\ u_{20} \end{bmatrix} = 0. \tag{2.48}$$

The normalized eigenvector which solves this matrix equation is

$$\begin{bmatrix} u_{10} \\ u_{20} \end{bmatrix} = \frac{1}{\sqrt{2}} \begin{bmatrix} 1 \\ 1 \end{bmatrix}. \tag{2.49}$$

This means that the atomic displacements are in the same direction. The lower branch of the dispersion relation is called the *acoustic* branch because the atoms oscillate in phase, like a sound wave in an elastic continuum.

For the $\omega = \sqrt{2k(1/M_1 + 1/M_2)}$ case,

$$\begin{bmatrix} -2k\, M_1/M_2 & -2k \\ -2k & -2k\, M_2/M_1 \end{bmatrix} \begin{bmatrix} u_{10} \\ u_{20} \end{bmatrix} = 0 \tag{2.50}$$

and the normalized eigenvector is

$$\begin{bmatrix} u_{10} \\ u_{20} \end{bmatrix} = \frac{1}{\sqrt{M_1{}^2 + M_2{}^2}} \begin{bmatrix} M_2 \\ -M_1 \end{bmatrix}. \tag{2.51}$$

This corresponds to atomic displacements in opposite directions which are inversely proportional to the atomic mass. The upper branch of the dispersion relation is called the *optical* branch because adjacent atoms oscillate out of phase and can be optically excited.

In a real crystal, of course, there are three dimensions. If the number of atoms per unit cell is *n*, then a crystal will have 3 acoustical branches and 3*n* - 3 optical branches. A diatomic linear chain therefore has 3 optical branches and 3 acoustical branches. The branches are labeled according to whether the oscillations are longitudinal or transverse, so there are two transverse optical (TO) modes, one longitudinal optical (LO) mode, two transverse acoustical (TA) modes, and one longitudinal acoustical (TA) mode.

2.2.3 Thermal Properties

Although the dispersion relations for lattice waves are derived classically, quantum mechanics dictates that the energy of an oscillation must be quantized. If ω is the vibrational frequency, the energy is

$$E = \left(n + 1/2\right)\hbar\omega \qquad\qquad n = 0,1,2,... \tag{2.52}$$

One quantum of lattice vibrational energy is called a *phonon.* Following the treatment given in Kittel (1986), the thermal properties of phonons can be derived. The average number of phonons $\langle n \rangle$ is given by the Planck distribution

$$\langle n \rangle = \frac{1}{e^{\hbar\omega/k_BT} - 1} \ . \tag{2.53}$$

To find the total phonon energy U, we sum the modes from all the branches p and wavevectors $\mathbf{q}$:

$$U = \sum_{p} \sum_{\mathbf{q}} \left(\langle n_{\mathbf{q},p} \rangle + 1/2\right)\hbar\omega_{\mathbf{q},p} \, . \tag{2.54}$$

The 1/2 term is a constant which, for thermodynamical calculations, may be dropped. Inserting the Planck distribution function (2.53) into Eq. 2.54 yields

$$U = \sum_{p} \sum_{\mathbf{q}} \frac{1}{e^{\hbar\omega_{\mathbf{q},p}/k_BT} - 1} \hbar\omega_{\mathbf{q},p} \, . \tag{2.55}$$

The points in $\mathbf{q}$ space are extremely dense, so the sum over wavevectors may be converted to an integral

$$U = \sum_{\lambda} \int_{0}^{\infty} \frac{\hbar\omega}{e^{\hbar\omega/k_BT} - 1} D_\lambda(\omega) d\omega \ , \tag{2.56}$$

where $D_\lambda(\omega)d\omega$ is the number of modes between ω and $\omega + d\omega$, for a polarization λ (e.g., transverse or longitudinal).

To obtain an analytical expression for the phonon energy, the Debye model assumes that the dispersion relation for a solid is given by

$$\omega = v_s q \tag{2.57}$$

where v_s is the classical speed of sound. This model is good for the acoustical branch for small q, where the dispersion relation is approximately linear. The density of states is given by

$$\begin{aligned} D(\omega) &= \frac{1}{(2\pi)^3} 4\pi\, k^2 \frac{dk}{d\omega} \\ &= \frac{1}{2\pi^2 v_s^{\,3}} \omega^2 d\omega \end{aligned} \tag{2.58}$$

With the additional assumption that the three branches are degenerate, Eq. 2.56 becomes

$$U = \frac{3}{2\pi^2 v_s^{\,3}} \int_0^{\omega_D} \frac{\hbar\omega^3}{e^{\hbar\omega/k_B T} - 1} d\omega, \tag{2.59}$$

where ω_D , the Debye frequency, is the cut-off point at the Brillouin zone edge. Defining the dimensionless variable $x \equiv \hbar\omega / k_B T$ yields

$$U = \frac{3}{2\pi^2 v_s^{\,3} \hbar^3} (k_B T)^4 \int_0^{T_D/T} \frac{x^3}{e^x - 1} dx, \tag{2.60}$$

where $T_D \equiv \hbar\omega_D / k_B$ is the Debye temperature.

2.3 Local Vibrational Modes (LVMs)

2.3.1 Analytical Approach

The translational symmetry of a perfect lattice is broken when a defect is introduced. As a simple example, consider the monatomic linear chain described in Sec. 2.2.1, but where one lattice mass M is replaced by a smaller mass m. Following the treatment given by Kittel (1966), we can show that one of the normal modes of the lattice will be localized around the light atom. Letting the light atom occupy the $n = 0$ position, the lattice equations of motion are given by

$$m\ddot{u}_0 = k\left(u_1 + u_{-1} - 2u_0\right) \tag{2.61}$$

$$M\ddot{u}_1 = k\left(u_2 + u_0 - 2u_1\right) \ \ldots \tag{2.62}$$

The solution to the perfect linear chain is given by Eq. 2.39,

$$\omega = 2\sqrt{\frac{k}{M}}\sin\left(qa/2\right). \tag{2.63}$$

Euler's equation states

$$\sin z = [\exp(iz) - \exp(-iz)]/2i, \tag{2.64}$$

so that a mode with a frequency higher than the phonon frequencies can be obtained by letting the wave number q be complex:

$$q = q_R + iq_I\,. \tag{2.65}$$

From Eq. 2.64, we have the identity

$$\sin(qa/2) = [\exp(iq_R a/2)\exp(-q_I a/2) - \exp(-iq_R a/2)\exp(q_I a/2)]/2i \tag{2.66}$$

$$= \sin(q_R a/2) \cosh(q_I a/2) - i \cos(q_R a/2) \sinh(q_I a/2) \,.$$

For the frequency (2.63) to be real, the imaginary component must equal zero. This implies that $q_R = \pi/a$. The displacement of atom n is then given by Eq. 2.31:

$$u_n = u_0 \exp(i\pi n) \exp(-q_I na) \exp(-i\omega t) \tag{2.67}$$

$$= u_0 (-1)^n \exp(-q_I an) \exp(-i\omega t) \,.$$

Substituting this into Eq. 2.61 yields

$$\omega^2 = (k/m)[2 + 2\exp(-q_I a)] \tag{2.68}$$

while substituting into Eq. 2.62 yields

$$\omega^2 = (k/M)[2 + \exp(-q_I a) + \exp(q_I a)] \,. \tag{2.69}$$

Solving these simultaneous equations yields

$$\exp(q_I a)=(2M - m)/m \tag{2.70}$$

and

$$\omega^2 = \omega_{\max}^2 \frac{M^2}{2Mm - m^2}, \tag{2.71}$$

where $\omega_{\max} = (4k/M)^{1/2}$ is the maximum frequency of the unperturbed linear chain. If $m << M$, then Eq. 2.71 can be approximated

$$\omega^2 \approx \omega_{\max}^2 \frac{M}{2m} \,. \tag{2.72}$$

2.3.2 Numerical Approach

If a mass defect is introduced into a compound semiconductor, new vibrational modes will arise depending on whether the defect replaces the heavy or the light lattice atom (Barker and Sievers, 1975). In the diatomic linear chain model discussed in Sec. 2.2.2, the equations of motion in the n^{th} unit cell are given by

$$\begin{aligned} M_1 \ddot{u}_{1,n} &= k\left(u_{2,n-1} + u_{2,n} - 2u_{1,n}\right) \\ M_2 \ddot{u}_{2,n} &= k\left(u_{1,n} + u_{1,n+1} - 2u_{2,n}\right) \end{aligned}, \tag{2.73}$$

where M_1 and M_2 are the light and heavy masses, respectively. The normal modes are given by

$$u_{2,n} = u^0{}_{2,n}\, e^{i\omega t}, \tag{2.74}$$

where the lack of translational invariance means that the normal modes do not have real wave numbers. Substituting the normal modes into Eq. 2.73 yields

$$\begin{aligned} \left(\omega^2 - 2k/M_1\right)u_{1,n} + k/M_1\left(u_{2,n-1} + u_{2,n}\right) = 0 \\ \left(\omega^2 - 2k/M_2\right)u_{2,n} + k/M_2\left(u_{1,n-1} + u_{1,n}\right) = 0 \end{aligned}. \tag{2.75}$$

In matrix form, this set of equations is written

$$\begin{bmatrix} \omega^2 - 2k/M_1 & k/M_1 & 0 & 0 & \cdots & 0 & k/M_1 \\ k/M_2 & \omega^2 - 2k/M_2 & k/M_2 & 0 & \cdots & 0 & 0 \\ \vdots & \vdots & \vdots & \vdots & \ddots & \vdots & \vdots \\ k/M_2 & 0 & 0 & 0 & \cdots & k/M_2 & \omega^2 - 2k/M_2 \end{bmatrix} \begin{bmatrix} u_{1,1} \\ u_{2,1} \\ \vdots \\ u_{2,N} \end{bmatrix} = 0 \tag{2.76}$$

where I have assumed periodic boundary conditions. The eigenvalues ω and eigenvectors $\boldsymbol{u}_n$ can be determined numerically. A mass defect can be introduced by changing the M_1 or M_2 values on the first or second line, respectively, of the matrix. The phonon density of states is then produced by plotting a histogram of the eigenvalues.

As an example, consider the compound semiconductor GaP, with $M_1 = 70$ and $M_2 = 31$. Using *MATLAB* to diagonalize the matrix (2.77), I calculated the phonon density of states for a linear chain with $N = 128$ unit cells (Figure 2.3), where the spring constant k is chosen such that $\omega_{TO} = 366$ cm^{-1}. If a carbon atom ($m = 12$) replaces a phosphorus, a new mode appears at $\omega = 510$ cm^{-1}. The exponentially decaying vibrational amplitudes are shown in Figure 2.4. Experimentally, the ^{12}C LVM has a frequency of 606 cm^{-1} (Hayes *et al.*, 1970).

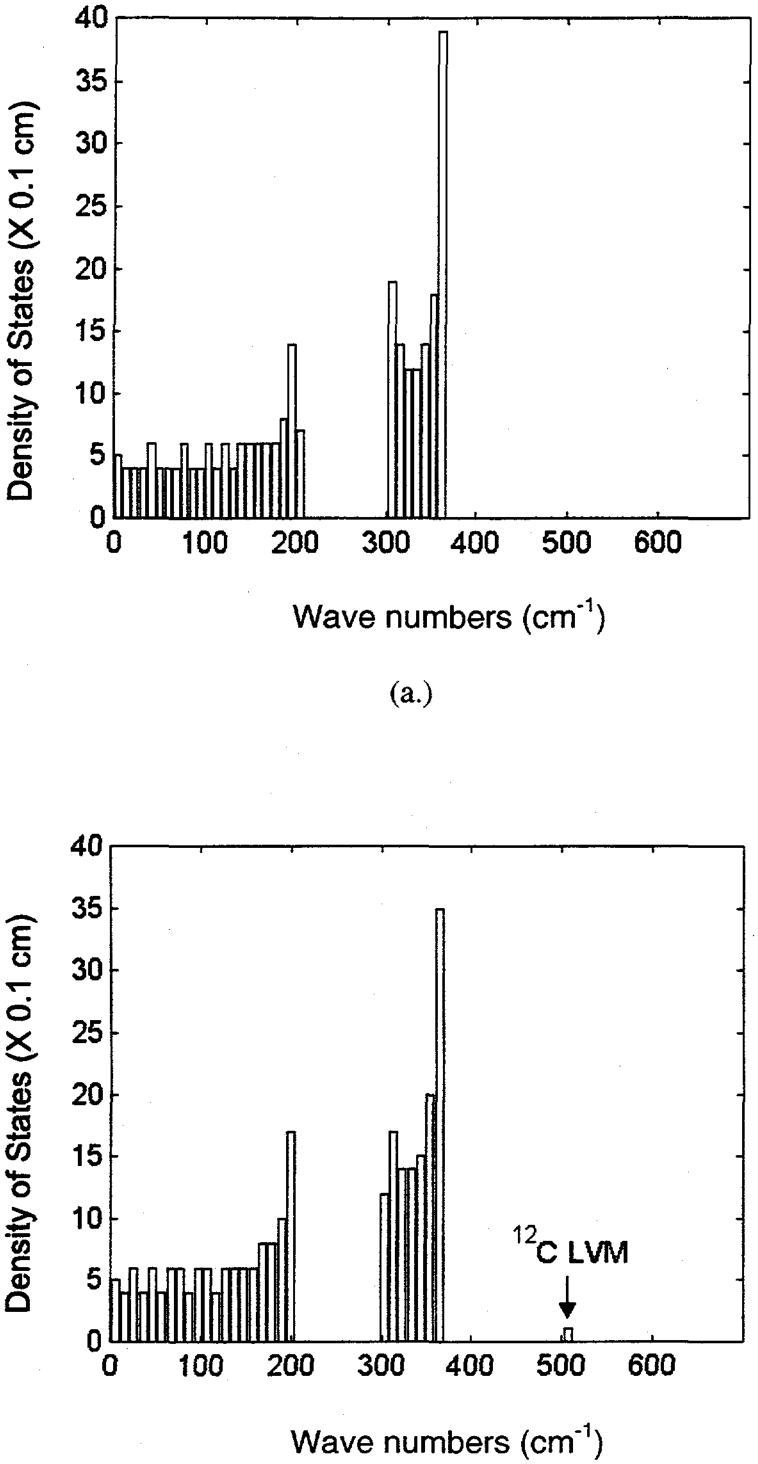

(a.)

(b.)

Figure 2.3. Calculated density of states for a GaP linear chain without (a) and with (b) a ^{12}C mass defect.

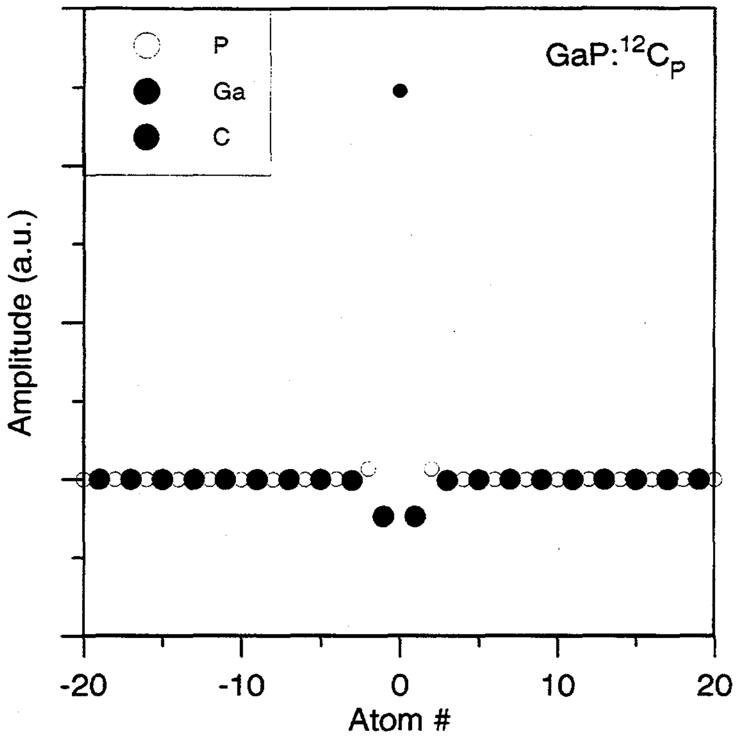

Figure 2.4. Plot of the vibrational amplitudes around the ^{12}C mass defect in a GaP linear chain.

If the phosphorus is replaced by an atom heavier than phosphorus but lighter than gallium, a *gap mode* will appear, in the gap between the acoustic and optical phonons. As an example, consider the As_P impurity ($m = 75$). As shown in Figure 2.5, a mode appears at $\omega = 240$ cm^{-1}. Although the vibrations are localized around the impurity (Figure 2.6), the decay in the amplitudes is not exponential. Experimentally, Grosche *et al.* (1995) have observed the As_P gap mode at 269 cm^{-1}. In addition, they have resolved the fine structure arising from the different combinations of the neighboring gallium isotopes.

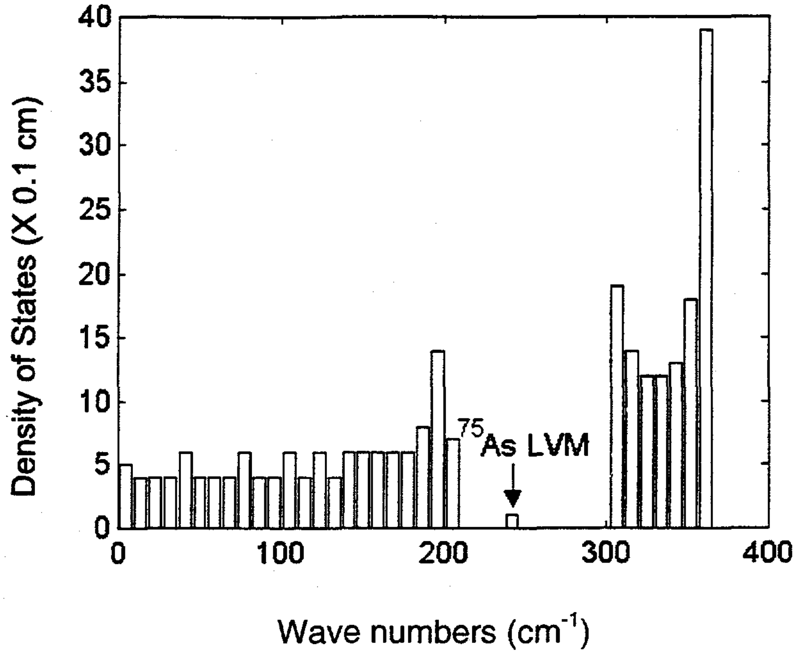

Figure 2.5. Calculated density of states for a GaP linear chain with an As_P mass defect.

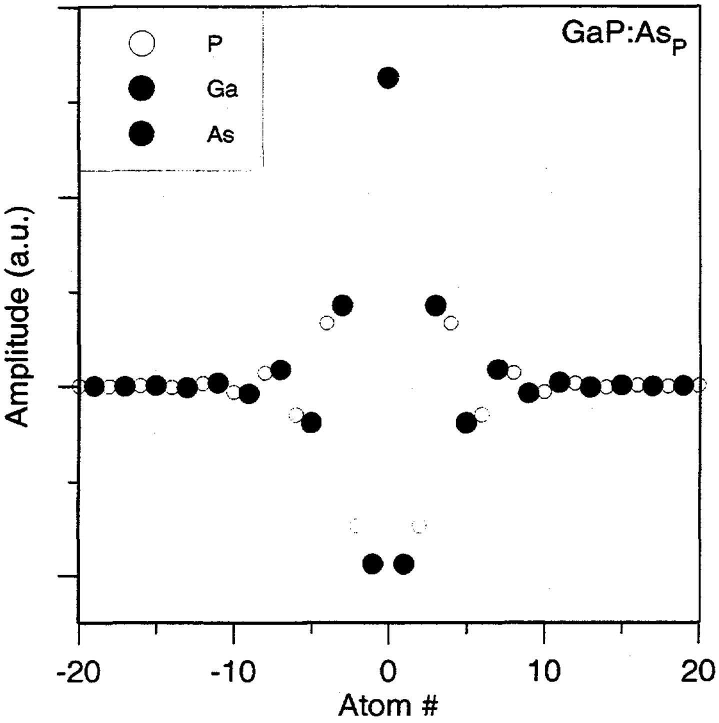

Figure 2.6. Vibrational amplitudes around an As_P mass defect in a GaP linear chain.

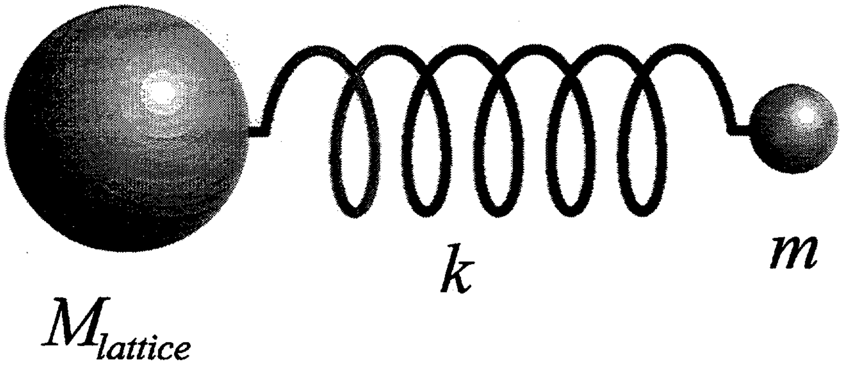

Figure 2.7. Diatomic model for LVMs.

2.3.3 Diatomic Model

The diatomic model is a useful empirical model that has been used to quantitatively describe the frequencies and isotope shifts of numerous LVMs (Haller 1995). In this model, an impurity of mass m is attached by a spring k to the lattice, whose mass is represented by $M_{lattice}$. The vibrational frequency of this diatomic molecule is given by

$$\omega = \sqrt{k\left(1/M_{lattice} + 1/m\right)} \equiv \sqrt{k/\mu}\,, \tag{2.78}$$

where μ is the reduced mass. In the case of hydrogen, $m = 1$ amu. To verify that a LVM is in fact hydrogen-related, the hydrogen can be replaced by deuterium ($m = 2$ amu). The isotopic frequency ratio is given by

$$r = \omega_H/\omega_D = \sqrt{2\frac{M_{lattice}+1}{M_{lattice}+2}}, \tag{2.79}$$

where ω_H and ω_D are the hydrogen and deuterium frequencies, respectively. r is slightly less than the square root of two, owing to the fact that $M_{lattice}$ is finite.

2.3.4 Anharmonicity

Another effect which reduces the isotopic frequency ratio is the anharmonicity of the potential. The hydrogen does not reside in a perfectly parabolic potential; rather, the potential becomes weaker for larger displacements. The Morse potential (Morse 1929), for example, is given by

$$V(x) = D_e\,[\exp(-\beta x)-1]^2\,, \tag{2.80}$$

where D_e is the binding energy. For small x, the Morse potential approximates a harmonic potential, with a spring constant $k = 2D_e\beta^2$. The hydrogen has a larger vibrational amplitude than the deuterium and its wavefunction samples more of the anharmonicity. Its frequency is lowered relative to the deuterium frequency, so that the factor $r = \omega_H / \omega_D$ is reduced.

To show this quantitatively, the energy eigenvalues of the Morse potential are given by

$$E_n = \hbar\omega_e\,(n + \tfrac{1}{2})[1 - x_e\,(n + \tfrac{1}{2})], \tag{2.81}$$

where

$$\omega_e = \beta\,(2D_e/\mu)^{1/2} \tag{2.82}$$

and

$$\omega_e\,x_e = \hbar\beta^2/2\mu\;. \tag{2.83}$$

The first excited state is given by

$$\Delta E = E_1 - E_0 = \hbar\omega_e - 2\hbar\omega_e x_e\,. \tag{2.84}$$

The anharmonic term $\omega_e\,x_e$ is inversely proportional to the reduced mass. Therefore, the anharmonic term is greater for hydrogen than for deuterium and the isotopic frequency ratio r is reduced.

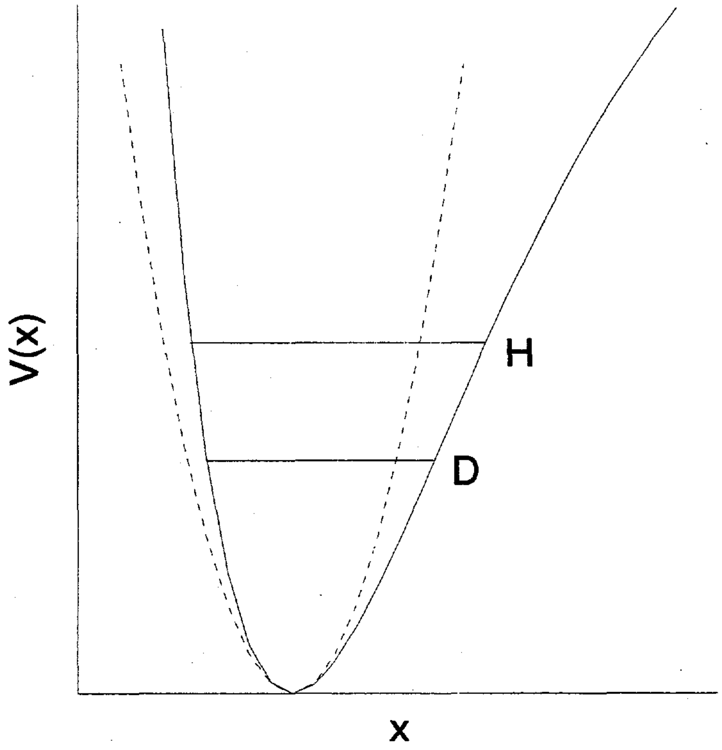

Figure 2.8. Hydrogen and deuterium ground states in a Morse potential (solid line). For comparison, the parabolic potential (dashed line) is shown.

2.4 Infrared Absorption

An important technique for probing the vibrational spectrum of a defect is infrared absorption. A photon can be absorbed by the defect, its energy going into a vibrational excitation. Most of the results presented in this thesis were obtained via infrared absorption spectroscopy.

2.4.1 Classical Treatment

Classically, an oscillating dipole can be modeled as two masses M and m, with electric charges $\pm e$, attached to each other by a spring with a spring constant k. The equation of motion is given by

$$\ddot{x} + \gamma\dot{x} + \omega_o^2 x = eE(t)/\mu \ , \tag{2.85}$$

where γ is a damping constant, $\omega_o = \sqrt{k/\mu}$ is the natural angular frequency, $\mu = 1/(1/M + 1/m)$ is the reduced mass, and $E(t)$ is the electric field. At the dipole, the electric field of a plane wave is given by

$$E(t) = E_o \exp(i\omega t). \tag{2.86}$$

The solution to Eq. 2.85 is also a complex exponential,

$$x(t) = x_o \exp(i\omega t), \tag{2.87}$$

with an amplitude given by

$$x_o = \frac{eE_o/\mu}{\omega_o^2 - \omega^2 + i\gamma\,\omega} \ . \tag{2.88}$$

For n dipoles per unit volume, the polarization is given by

$$P = nex = \frac{ne^2E_o/\mu}{\omega_o^2 - \omega^2 + i\gamma\,\omega}\exp(i\omega t) \tag{2.89}$$

and the dielectric constant $\varepsilon = 1 + 4\pi P/E$ is given by

$$\varepsilon(\omega) = 1 + \frac{4\pi\, ne^2}{\mu}\frac{1}{\omega_o^2 - \omega^2 + i\gamma\,\omega} \ . \tag{2.90}$$

The *oscillator strength* of this simple dipole is equal to unity.

Differentiating Eq. 2.87 with respect to time yields the relative velocity of the two masses,

$$v(t) = x_o\, i\omega \exp(i\omega t). \tag{2.91}$$

The power dissipated by the dipole is given by

$$P(t) = e\mathrm{Re}\{E(t)\}\mathrm{Re}\{v(t)\}. \tag{2.92}$$

Assuming for simplicity that E_o is real, Eq. 2.92 becomes

$$P(t) = \frac{e^2 E_o^{\,2}\omega}{\mu}\cos\omega\, t\, \mathrm{Re}\left\{\frac{\left(\omega_o^{\,2}-\omega^2\right)-i\gamma\,\omega}{\left(\omega_o^{\,2}-\omega^2\right)^2+\gamma^2\omega^2}\left(i\cos\omega\, t-\sin\omega\, t\right)\right\} \tag{2.93}$$

$$= \frac{e^2 E_o^{\,2}\omega}{\mu}\cos\omega\, t\,\frac{\gamma\,\omega\cos\omega\, t-\left(\omega_o^{\,2}-\omega^2\right)\sin\omega\, t}{\left(\omega_o^{\,2}-\omega^2\right)^2+\gamma^2\omega^2}\ .$$

Using the fact that

$$\left\langle\cos^2\omega t\right\rangle = 1/2 \tag{2.94}$$

and

$$\left\langle\sin\omega t\cos\omega t\right\rangle = 0, \tag{2.95}$$

the time-averaged power dissipation can be written

$$\left\langle P\right\rangle = \frac{e^2 E_o^{\,2}\omega^2\gamma/2\mu}{\left(\omega_o^{\,2}-\omega^2\right)^2+\gamma^2\omega^2}\,. \tag{2.96}$$

The peak in the power spectrum occurs near ω=ω_o, where the amplitude of vibration is greatest. The cross section of absorption is given by the ratio of the power dissipation to the intensity of the electromagnetic wave,

$$\sigma = \frac{\left\langle P\right\rangle}{cE_o^{\,2}/8\pi} = \frac{4\pi\, e^2\omega^2\gamma}{\mu\, c}\,\frac{1}{\left(\omega_o^{\,2}-\omega^2\right)^2+\gamma^2\omega^2}\,. \tag{2.97}$$

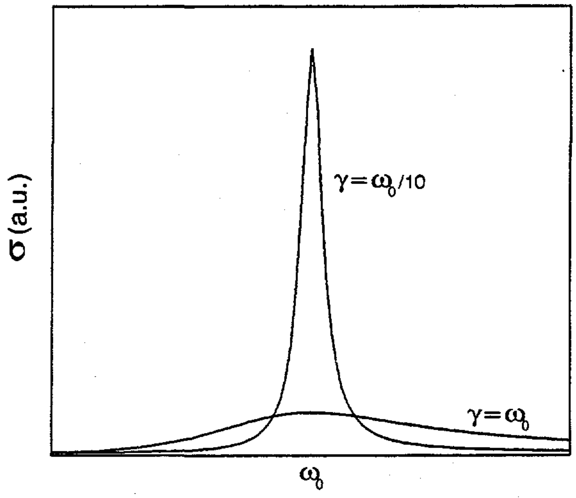

Figure 2.9. Cross section of absorption for oscillators with different damping coefficients.

The cross section is in units of cm^2 and defines an effective area in which incident light is totally absorbed. The damping factor γ is approximately the full width half maximum (FWHM) of the absorption peak.

If an electromagnetic wave of intensity I impinges on a material with n dipoles per cm^3 and a thickness dx, then the transmitted intensity will be given by

$$I(x+dx)=I(x)\,(1-\sigma n\,dx). \tag{2.98}$$

Rearranging terms yields

$$[I(x+dx)-I(x)]/dx = -\sigma n I(x) \tag{2.99}$$

and as the thickness dx goes to zero,

$$dI(x)/dx = -\sigma n I(x). \tag{2.100}$$

The solution to this differential equation is a decaying exponential,

$$I(x) = I_o\exp(-\sigma n x) \equiv I_o\exp(-\alpha x), \tag{2.101}$$

where α is the *absorption coefficient* and has units of cm^{-1}.

The *integrated absorption* is defined

$$A_I = \int_0^\infty \alpha(\omega)d\omega = n\int_0^\infty \sigma(\omega)d\omega\,. \tag{2.102}$$

Substituting Eq. 2.97 into Eq. 2.102 yields

$$A_I = \frac{4\pi\, ne^2\gamma}{\mu\, c}\int_0^\infty \omega^2\frac{d\omega}{\left(\omega_0{}^2-\omega^2\right)^2+\gamma^2\omega^2}\,. \tag{2.103}$$

For a "high-Q" oscillator, $\omega << \gamma$. In this limit, the integrand is nonzero only in a narrow range about ω_0. We can therefore write

$$\omega = \omega_0 + \delta\omega\,, \tag{2.104}$$

where $\delta\omega << \omega_0$. Making this substitution into the integral (2.103) and keeping the lowest order $\delta\omega$ terms yields

$$A_I = \frac{4\pi\, ne^2\gamma}{\mu\, c}\int_0^\infty \frac{d(\delta\,\omega)}{4\delta\,\omega^2+\gamma^2}\,, \tag{2.105}$$

where the integrand is a Lorentzian line shape. The integral can be solved by a trigonometric substitution which yields

$$A_I(\text{cm}^{-1}\text{rad / s}) = n\frac{\pi^2 e^2}{\mu c}. \tag{2.106}$$

As noted, the integrated absorption in Eq. 2.106 is given in units of cm^{-1}rad/s. In spectroscopy it is more convenient to use *wave numbers*, defined as $1/\lambda$, where λ is the wavelength of incoming light, instead of ω. To convert to wave numbers, we use the relation

$$1/\lambda = \omega/2\pi c, \tag{2.107}$$

yielding

$$A_I(\mathrm{cm}^{-2}) = n\frac{\pi e^2}{2\mu c^2}. \tag{2.108}$$

Note that the integrated absorption is independent of the width γ and the frequency ω_0 of the peak. If the e is equal to the charge of an electron and μ is the mass of a proton, then

$$A_I\,(\mathrm{cm}^{-2}) \sim 2.5 \text{ X } 10^{-16}\, n(\mathrm{cm}^{-3})\,. \tag{2.109}$$

This simple classical result is a reasonable order-of-magnitude estimate. For example, the Zn-H complex in InP has an experimental integrated absorption given by $A_I\,(\mathrm{cm}^{-2}) = 5 \text{ X } 10^{-15}\, n(\mathrm{cm}^{-3})$ (Chevallier *et al.*, 1991). The theoretical model given here neglects screening effects in the solid that reduce the dipole moment, and therefore the integrated absorption, of the complex.

2.4.2 Quantum Mechanical Treatment

A quantum mechanical approach yields a similar result. Following the treatment given by Sakurai (1985), the absorption cross section for exciting a transition from an initial state i to a final state f is given by

$$\sigma = \frac{4\pi^2 e^2}{\mu^2 \omega\, c}\left|\langle f|e^{i\mathbf{k}\cdot\mathbf{x}}\hat{\varepsilon}\cdot\mathbf{p}|i\rangle\right|^2 \delta\left(E_f - E_i - \hbar\omega\right), \tag{2.110}$$

where $\mathbf{k}$ and ω are the wave vector and angular frequency, respectively, of the electromagnetic wave, **p** is the momentum operator, and δ is the Dirac delta function. In the absence of damping, the transition is infinitely sharp, so that the cross section is nonzero only when the energy of the incoming light equals the transition energy. In the electric dipole approximation, the wavelength of the light is assumed to be much longer than the dipole, so that the exponential in Eq. 2.110 can be approximated

$$e^{i\mathbf{k}\cdot\mathbf{x}} \approx 1. \tag{2.111}$$

If **p** is directed along the x axis, then Eq. 2.110 can be written

$$\sigma = \frac{4\pi^2 e^2}{\mu^2 \omega c} \left|\langle f|p_x|i\rangle\right|^2 \delta\left(E_f - E_i - \hbar\omega\right). \tag{2.112}$$

Given the commutation relation

$$[x, H_0] = \frac{i\hbar p_x}{\mu}, \tag{2.113}$$

the matrix element in Eq. 2.112 can be written

$$\langle f|p_x|i\rangle = \frac{\mu}{i\hbar}\langle f|[x, H_0]|i\rangle = i\mu\omega_{fi}\langle f|x|i\rangle, \tag{2.114}$$

where $\omega_{fi} = \omega_f - \omega_i$. Substituting Eq. 2.114 into Eq. 2.112 yields

$$\sigma = \frac{4\pi^2 e^2}{\hbar c}\omega_{fi}\left|\langle f|x|i\rangle\right|^2 \delta\left(\omega - \omega_{fi}\right). \tag{2.115}$$

To compare this with the classical result, we integrate over all frequencies to obtain the integrated absorption:

$$A_I = n\int_0^\infty \sigma(\omega)\,d\omega = \frac{4\pi^2 n e^2}{\hbar c}\sum_f \omega_{fi}\left|\langle f|x|i\rangle\right|^2. \tag{2.116}$$

The *oscillator strength* is defined

$$f_{fi} \equiv \frac{2\mu}{\hbar}\omega_{fi}\left|\langle f|x|i\rangle\right|^2 \tag{2.117}$$

and is a dimensionless quantity that is proportional to the probability of a transition from i to f. According to the Thomas-Reiche-Kuhn sum rule (Sakuri 1985),

$$\sum_f f_{fi} = 1. \tag{2.118}$$

Applying this rule to Eq. 2.117 yields

$$A_l(\mathrm{cm^{-1}rad/s}) = n\frac{2\pi^2 e^2}{\mu c}, \tag{2.119}$$

which differs from the classical result (2.106) by a factor of two.

3. Experimental Techniques

3.1 Fourier Transform Infrared Spectroscopy (FTIR)

Fourier transform infrared spectroscopy (FTIR) is a characterization technique widely used in physics, chemistry, and biology. It has the advantages of high spectral resolution, good signal-to-noise ratios, and the ability to measure a broad region of the spectrum in a short amount of time. At the heart of a FTIR spectrometer is a Michelson interferometer (Figure 3.1). A parallel beam of collimated light from a broadband source is directed at a semitransparent beamsplitter. One of the two beams reflects off a movable mirror while the other beam reflects off a fixed mirror. The two beams recombine at the beamsplitter, travel through the sample, and finally impinge upon a detector. The detector signal is proportional to the intensity of the interfered beam and the plot of intensity versus optical path difference in real space is the *interferogram*. As shown in the following section, when the interferogram is Fourier transformed, the resulting function is a plot of the spectrum in frequency space. In practice, to maximize the signal-to-noise ratio, several hundred to several thousand interferograms are taken and averaged before the Fourier transform is performed.

As shown in Figure 3.1, the sample may be placed in a liquid helium cryostat. A photoconductor such as Ge:Cu is mounted directly behind the sample and kept at a temperature of 10 K. A DC bias of a few volts is applied across the photoconductor, and when light of sufficient energy excites a hole (electron) into the valence (conduction) band, current is produced. For variable temperature measurements, a detector such as a mercury- cadmium-telluride (MCT) diode cooled to 77 K may be placed external to the cryostat. A detailed description of our spectrometer is given in Sec. 3.1.5.

3.1.1 Advantages of Fourier Transform Spectroscopy

There are two major advantages of a Fourier transform spectrometer over a grating spectrometer. First, a Fourier transform spectrometer can obtain a broad spectrum in a time that is short compared to a grating spectrometer. This is known as Felgett advantage (Felgett, 1958). In a broad spectrum ranging in frequency from ν_1 to ν_2, the number of spectral elements is given by

$$M = (\nu_2 - \nu_1)/\delta\nu \equiv \Delta\nu/\delta\nu \ , \tag{3.1}$$

where $\delta\nu$ is the resolution. If the time to observe the entire spectrum is T, then the time to observe a single spectral element it T/M. Assuming the detector noise is independent of the signal intensity, the signal-to-noise ratio for a grating spectrometer is given by

$$\left(S/N\right)_G \propto \sqrt{T/M} \, . \tag{3.2}$$

In an interferometer, however, all the spectral elements are measured simultaneously. Therefore, the signal-to-noise ratio for a Fourier transform spectrometer is independent of M:

$$(S/N)_I \propto \sqrt{T}. \tag{3.3}$$

For a given time *T*, the advantage of a Fourier transform spectrometer over a grating spectrometer is $\sqrt{M}$. Since *M* is often on the order of 10,000, this represents a significant advantage. In the visible spectral range, where detectors typically operate in the photon-counting regime, the signal-to-noise ratio is proportional to the square root of the signal and the Felgett advantage is no longer important.

As second advantage that interferometers have over grating spectrometers is the throughput, or Jacquinot (1960) advantage. In a grating spectrometer, the resolution is limited by the width of the entrance and exit slits. In a Fourier transform spectrometer, however, the resolution is determined by the length of the mirror path (Sec. 3.1.3). Therefore, for high resolution measurements the Fourier transform spectrometer is preferred.

3.1.2 Derivation of Fourier Result

Following the treatment given by Bell (1972), I derive the equation used in Fourier transform spectroscopy. The two beams in the Michelson interferometer are separated by an optical path difference δ. The superposition of the two beams is given by

$$E(z) = \int_{-\infty}^{\infty} \left[E_o(k) e^{ikz} + E_o(k) e^{ik(z-\delta)} \right] dk, \tag{3.4}$$

where $k=2\pi/\lambda$, *E* is electric field, and *z* is distance along the beam. From Eq. 3.4 is can be seen that the resultant electric field is given by

$$E_R(k) = E_o(k)\left(1 + e^{-ik\delta}\right). \qquad (3.5)$$

The intensity of the electromagnetic wave is given by the magnitude of its Poynting's vector (Jackson 1975):

$$I(k) = \frac{c}{8\pi}\left|E_R(k)\right|^2 \qquad (3.6)$$

$$= \frac{c}{4\pi}\left|E_o(k)\right|^2 (1 + \cos k\delta).$$

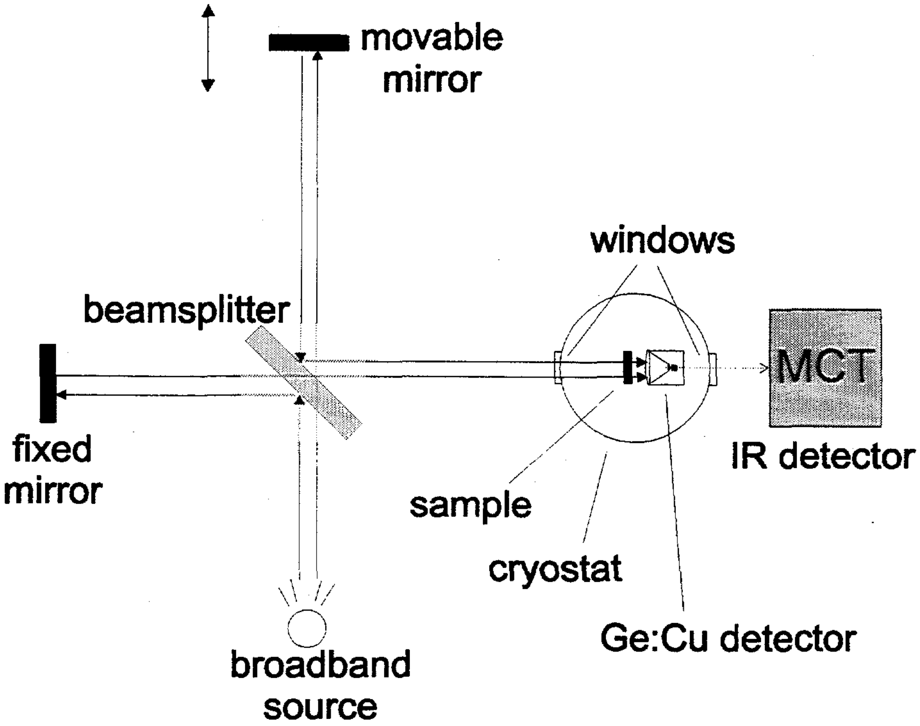

Figure 3.1. Schematic of the Fourier Transform infrared (FTIR) spectrometer.

Since the phases of different frequencies of light are random with respect to each other, the intensities add linearly:

$$I_R(\delta) = \frac{c}{2\pi}\left\{\int_0^\infty |E_o(k)|^2\, dk + \int_0^\infty |E_o(k)|^2 \cos k\delta\; dk\right\}, \tag{3.7}$$

where the integrals are semi-infinite because the integrands are even functions. This is the interferogram. Only the second integral varies with δ ; the first is an offset term. The second integral is given by

$$I(\delta) = 4\int_0^\infty I_0(k) \cos k\delta\; dk, \tag{3.8}$$

where

$$I_0(k) = \frac{c}{8\pi}|E_0(k)|^2. \tag{3.9}$$

Eq. 3.8 is simply the Fourier transform of the intensity $I_0(k)$. To obtain the spectrum $I_0(k)$, we perform an inverse Fourier transform:

$$I_0(k) = (\text{const.})\int_0^\infty I(\delta) \cos k\delta\; d\delta\ . \tag{3.10}$$

In practice, a computer uses a fast Fourier transform (FFT) algorithm (e.g., Cooley and Tukey, 1965) to evaluate the integral (3.10).

3.1.3 Resolution

In the preceding derivation, the path length δ was assumed to vary from 0 to ∞. In an experiment, however, the scanning mirror can only travel a finite distance.

Suppose that the light source is monochromatic, with an intensity given by

$$I_0(k) = I_0\,\delta\,(k - k_0), \tag{3.11}$$

where k_0 is the wave number in cm^{-1} and δ is the Dirac delta function. The delta function can also describe a perfectly sharp absorption peak. Substituting this function into Eq. 3.8 yields

$$I(\delta) = 4I_0 \cos(k_0\delta). \tag{3.12}$$

As described in Sec. 3.1.5, the cosine interferogram from a laser is used to accurately measure the optical length difference δ.

If an absorption peak is described by a delta function, the peak measured by the FTIR spectrometer will be broadened by the finite scanning length L. The Fourier transform of the interferogram is given by

$$I_0(k) = (\text{const.})\int_0^L I(\delta)\cos k\delta \; d\delta \ , \tag{3.13}$$

where the interferogram is abruptly truncated at a distance L. Substituting the delta function interferogram (3.12) into Eq. 3.13 yields

$$I(k) = (\text{const.})\int_0^L \cos k_0\delta \cos k\delta \; d\delta \, . \tag{3.14}$$

Using the a trigonometric identity, this can be written

$$I(k) = (\text{const.})\int_0^L \big(\cos(k+k_0)\delta + \cos(k-k_0)\delta\big)\, d\delta \tag{3.15}$$

$$= (\text{const.})\,L\left[\frac{\sin\big((k-k_0)L\big)}{(k-k_0)L} + \frac{\sin\big((k+k_0)L\big)}{(k+k_0)L}\right].$$

For a typical mid-infrared spectrum, $L \sim 1\ \mathrm{cm}^{-1}$ and $k_0 \sim 1000\ \mathrm{cm}^{-1}$. Therefore, $k_0L >> 1$ and the second term can be neglected. The computed spectrum is then given by

$$I(k) = (\mathrm{const.})L\ \mathrm{sinc}\big((k - k_0)L\big), \tag{3.16}$$

where

$$\mathrm{sinc}\ z \equiv \sin z / z\ . \tag{3.17}$$

The sinc function has a central maximum with sidelobes (Figure 3.2). The sinc function is zero at $z = \pm\pi/2$, or $k = k_0 \pm \pi/(2\mathrm{L})$. The width of the central peak is therefore given by

$$\Delta k \sim 1/\mathrm{L}\ . \tag{3.18}$$

Thus, the resolution of the spectrometer is inversely proportional to the scanning length.

3.1.4 Apodization

As shown in Figure 3.2, abruptly truncating the spectrum at $\delta = L$ produces sidelobes that can be quite large. Apodization is a method which numerically "corrects" the interferogram in a way that reduces the size of the sidelobes. The most common apodization function is a linear function that goes to zero at $\delta = L$. For a delta function peak, the apodized spectrum is given by

$$I(k) = (\mathrm{const.})\int_0^L (1 - \delta / L)\cos(k - k_0)\delta\ d\delta\ , \tag{3.19}$$

where the $\cos(k + k_0)$ term is neglected as before. Integrating by parts yields

$$I(k) = (\mathrm{const.})\left[\frac{1 - \cos\big((k - k_0)L\big)}{(k - k_0)^2 L}\right], \tag{3.20}$$

and using a trigonometric identity, we have

$$I(k) = (\text{const.})\ \mathrm{sinc}^2[(k - k_0)L]. \tag{3.21}$$

The $\mathrm{sinc}^2 z$ function is shown in Figure 3.2 and has smaller sidelobes than the sinc z function.

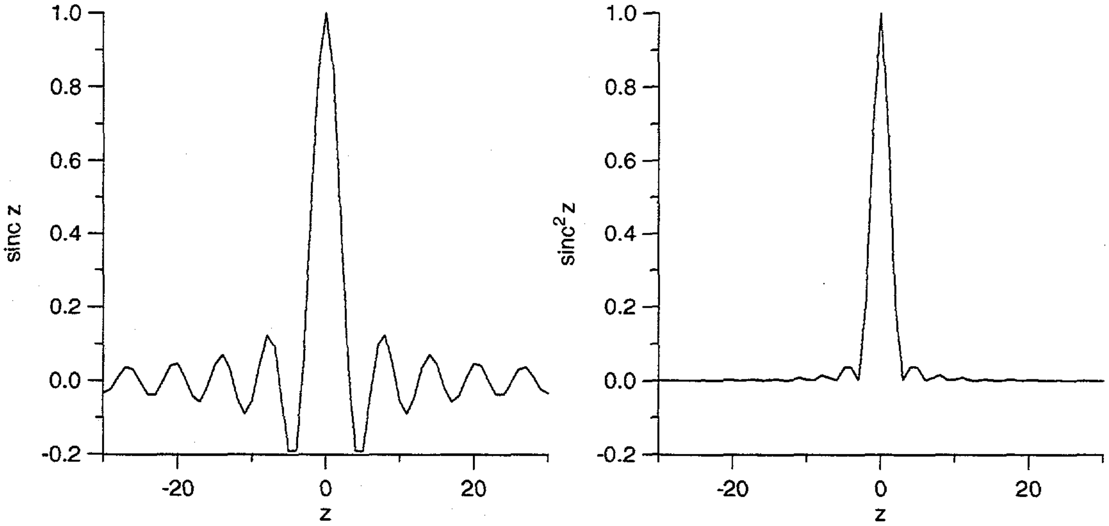

Figure 3.2. Plots of sinc(z) and sinc^2z.

3.1.5 Experimental Apparatus

Two spectrometers were used to obtain the infrared spectra presented in this thesis: the Digilab 80-E and Bomem DA8 vacuum Fourier Transform infrared (FTIR) spectrometers. The Digilab 80-E (see Wolk 1992) is capable of an instrumental resolution of 0.1 cm^{-1}. The Bomem DA8 is a newer instrument and is capable of a resolution of 0.02 cm^{-1}. In addition, the Bomem is a more versatile spectrometer, with several beamsplitters and optical ports, and detector modules.

Unlike the Digilab spectrometer, which uses a horizontally scanning mirror on air bearings, the Bomem instrument has a scanning mirror that moves vertically, allowing for a large optical path difference with a small footprint. The upper section (Figure 3.3) houses the scanning motor, mirror, and tube. The mirror is moved by a torque motor and a tensioned belt drive. The speed is servo-controlled by a tachometer on the motor shaft, which keeps the scanning velocity constant to within ±6%.

The middle section contains a beam switching compartment, which consists of a 45° mirror that can rotate to direct the beam to one of several ports. Two sets of transfer and focusing mirrors direct the beam onto the left or right sample compartments. The beam travels through the sample and onto an off-axis ellipsoidal mirror in the detector module which focuses the beam onto the detector. In addition, the beam switching compartment can direct the beam to the rear compartment, where a Janis continuous-flow liquid helium cryostat is housed.

The beamsplitters and water-cooled light sources are also in the middle section. Mylar beamsplitters are used for far-infrared studies (below 700 cm^{-1}). For mid-infrared studies, a KBr (450 to 4000 cm^{-1}) or a CaF_2 (1200 to 8000 cm^{-1}) beamsplitter is used. The beamsplitter can easily be changed by removing the beamsplitter cover plate. For a light source, we use a globar, which is a SiC bar heated to 1200°C. The blackbody radiation emitted by the globar extends from ~300 to 4000 cm^{-1}. In addition, there is a quartz-halogen source that emits light from ~2000 to 20,000 cm^{-1}. The light sources are mounted on a rotating wheel, so that one can choose a source without breaking vacuum.

The lower section of the spectrometer contains vacuum valves and electronics. The spectrometer is kept under vacuum (100 mTorr) by a roughing pump, in order to minimize infrared absorption peaks arising from CO_2 and H_2O in the air. A High Performance Vector Processor (HPVP) system executes the fast Fourier transforms (FFTs) and communicates with a 486 PC computer via a high-speed Ethernet connection.

The position of the scanning mirror is accurately measured by counting fringes of a single-mode He-Ne laser. All modes except the 632 nm line are suppressed, so it is a monochromatic source. The narrow laser beam, centered in the 2" diameter infrared light beam, is sent into the interferometer, where it produces a cosine interferogram (Eq. 3.12). The centers of the beamsplitters are all quartz, to split the laser beam. The wavelength is such that the laser interferogram passes through 31600 cycles per cm displacement of the scanning mirror. Before the laser beam can reach the sample, it is diverted by a 90° prism that directs the beam to detectors located on the laser reference detector card. By monitoring the laser interferogram, electronics on the card calculate the optical path difference δ.

Since the cosine interferogram produced by the He-Ne laser is periodic, it cannot be used to determine where the zero path difference (ZPD) occurs. To determine the ZPD, white light emitted by an incandescent bulb is also sent into the interferometer. Since the white light is a broadband source of light, its interferogram has a large maximum at zero path difference, where all wavelengths of light constructively interfere.

The white light travels through the same optics as the light from the globar. As with the laser, the white light is split by the quartz at the center of the beamsplitter and is sent to the detector card. When the fringes of the white light interferogram exceed a certain threshold (typically 0.7 to 1.5 volts), a pulse is produced. By locating the center pulse, the computer determines where ZPD occurs.

If the fixed and scanning mirrors are not properly aligned, different parts of the two beams will have different optical path lengths and the resolution will be limited. To align the mirrors, the Bomem spectrometer uses a dynamic alignment process, in which electromagnetic mirror tilt transducers adjust the mirrors continuously during each scan. The feedback is provided by the interfered He-Ne laser beam. Different parts of the beam impinge upon several detectors on the detector card, and the slight phase difference between the detectors provides information about the misalignment. With dynamic alignment, the angular deviation from optimal alignment is less than 10^{-6} radians.

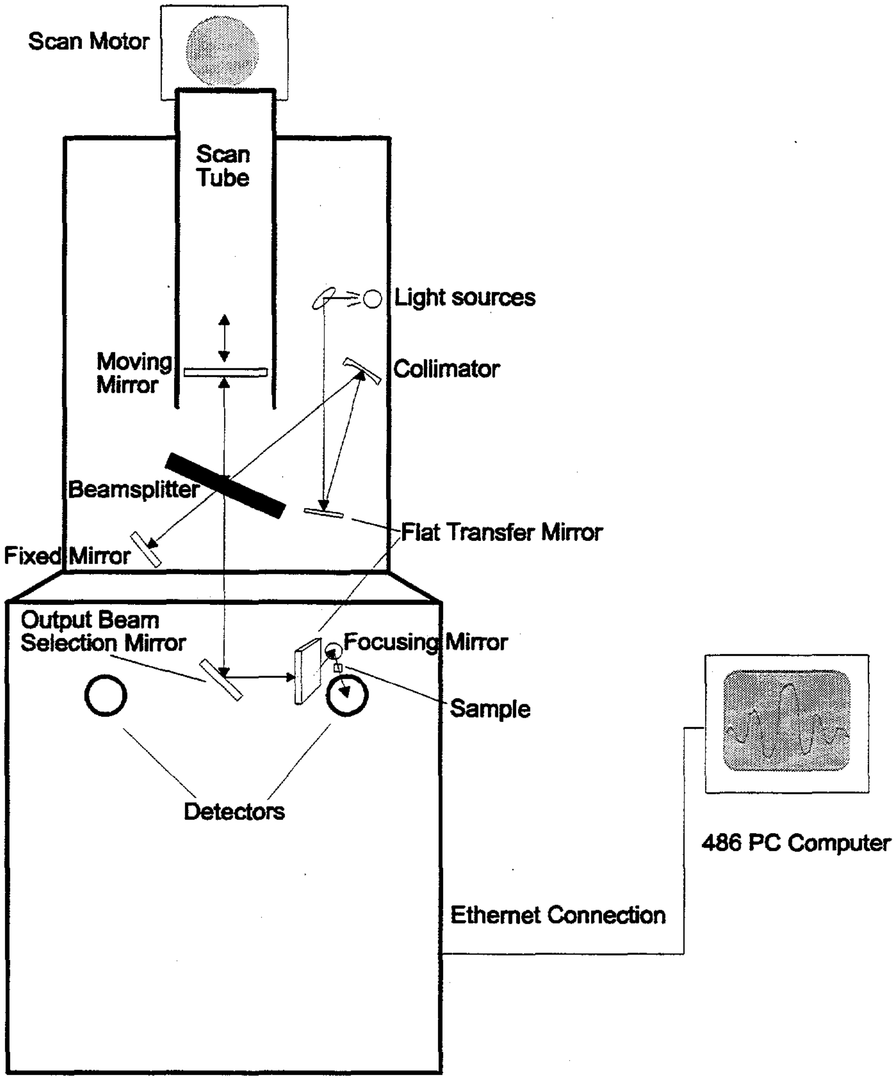

Figure 3.3. Schematic of the Bomem DA8 FTIR spectrometer (side view).

3.2 Raman Scattering

Raman scattering involves inelastic scattering of laser light from a complex such as a molecule or crystal. In Stokes Raman scattering, the incoming photon loses some of its energy by exciting rotational, vibrational or electronic modes. In anti-Stokes Raman scattering, the photon gains energy from a thermally populated mode. The photon polarization vector can also be changed. Since selection rules for Raman scattering and infrared absorption are generally different, the two complementary techniques can be used to accurately determine the symmetry of a complex.

The fundamental properties of Raman scattering can be described by classical theory (Cardona 1982). The starting point is the time-averaged power emitted per solid angle by an oscillating dipole

$$\frac{dP}{d\Omega} = \frac{\omega^4}{8\pi c^3}\left|\hat{\mathbf{e}}_s \cdot \mathbf{p}\right|^2 \tag{3.22}$$

where ω is the oscillation frequency, c is the speed of light in the medium, $\hat{\mathbf{e}}_s$ is the polarization of emitted light, and $\mathbf{p}$ is the electric dipole moment. The dipole $\mathbf{p}$ is induced by the incoming laser light, which has polarization $\hat{\mathbf{e}}_L$, electric field amplitude E_L, and frequency ω_L:

$$\mathbf{p} = \alpha \cdot \hat{\mathbf{e}}_L E_L \cos(\omega_L t), \tag{3.23}$$

where α is the polarizability tensor.

We now consider the specific case of vibrational Raman scattering. A defect in a crystal (or molecule in a vacuum) has one or more local vibrational modes, as explained in Sec. 2.3. A particular mode has a frequency ω_v and normal mode coordinate

$$u(t) = u_o \cos(\omega_v t). \tag{3.24}$$

The vibration is assumed to be adiabatic, so that at any point in time, the polarizability α is given by an equilibrium value which depends on the normal mode coordinate. α can be expanded in a Taylor series in small u:

$$\alpha = \alpha_o + \frac{\partial \alpha}{\partial u} u_o \cos(\omega_v t) + \cdots \tag{3.25}$$

Inserting this expression into Eq. 3.22 yields

$$\mathbf{p} = \alpha_o \cdot \hat{\mathbf{e}}_{\mathrm{L}} E_L \cos(\omega_L t) + \frac{\partial \alpha}{\partial u} \cdot \hat{\mathbf{e}}_{\mathrm{L}} u_o E_L \cos(\omega_L t) \cos(\omega_v t). \tag{3.26}$$

The first term on the right-hand-side is simply the Rayleigh scattering term. By a trigonometric identity, the second term can be written

$$\frac{\partial \alpha}{\partial u} \cdot \hat{\mathbf{e}}_{\mathrm{L}} u_o \frac{E_L}{2} \left\{ \cos[(\omega_L - \omega_v)t] + \cos[(\omega_L + \omega_v)t] \right\}. \tag{3.27}$$

The cosine terms describe scattered light with frequencies $\omega_L - \omega_v$ (Stokes) and $\omega_L + \omega_v$ (anti-Stokes). The Stokes line is produced by the emission of a phonon and the anti-Stokes line is produced by the absorption of a phonon.

By inserting the expression for the dipole (3.26) into Eq. 3.22, the time-averaged scattering efficiency can be obtained:

$$\frac{dP}{d\Omega} \propto \left| \hat{\mathbf{e}}_s \cdot \frac{\partial \alpha}{\partial u} \cdot \hat{\mathbf{e}}_{\mathrm{L}} \right|^2. \tag{3.28}$$

The Raman tensor **R** is proportional to $\partial \alpha / \partial u$; for the purposes of determining the symmetry of a complex, the constant of proportionality is unimportant.

The quantity (3.28) must be invariant under all the operations of the crystal point group (Appendix A). The vectors $\hat{\mathbf{e}}_s$ and $\hat{\mathbf{e}}_L$ belong to irreducible representations of the point group, designated Γ_s and Γ_L, respectively. To make (3.28) invariant, **R** must possess the symmetry of Γ_{R_i}:

$$\Gamma_s \otimes \Gamma_L = \Gamma_{R_1} \oplus \Gamma_{R_2} \oplus \cdots \qquad (3.29)$$

The different Γ_{R_i} representations correspond to Raman-active vibrational modes.

3.3 Diamond Anvil Cell (DAC)

The study of solids under large hydrostatic pressures is an active area of research in geology, physics, and materials science (Jayaraman 1983). One method of producing pressure is via a piston cylinder cell in which a pressure transmitting medium such as oil is compressed. Although these cells are useful for electrical measurements, the maximum pressure attainable by them is approximately 15 kbar. For higher pressures, a diamond anvil cell (DAC) is used.

In a DAC, the flat parallel faces of two diamonds press on a metal gasket. The sample is placed in a pressure transmitting medium in the gasket hole. Although a 4:1 methanol-ethanol mix is a commonly used medium, it has the disadvantage that it absorbs infrared light. Therefore, in variable pressure infrared transmission experiments, liquid nitrogen is commonly employed. At room temperature, N_2 solidifies at ~25 kbar (Figure 3.5). Although the N_2 is a solid at low temperatures and/or high pressures, it is a weakly bound Van der Walls solid which produces very hydrostatic pressures up to 130 kbar (Jayaraman 1983).

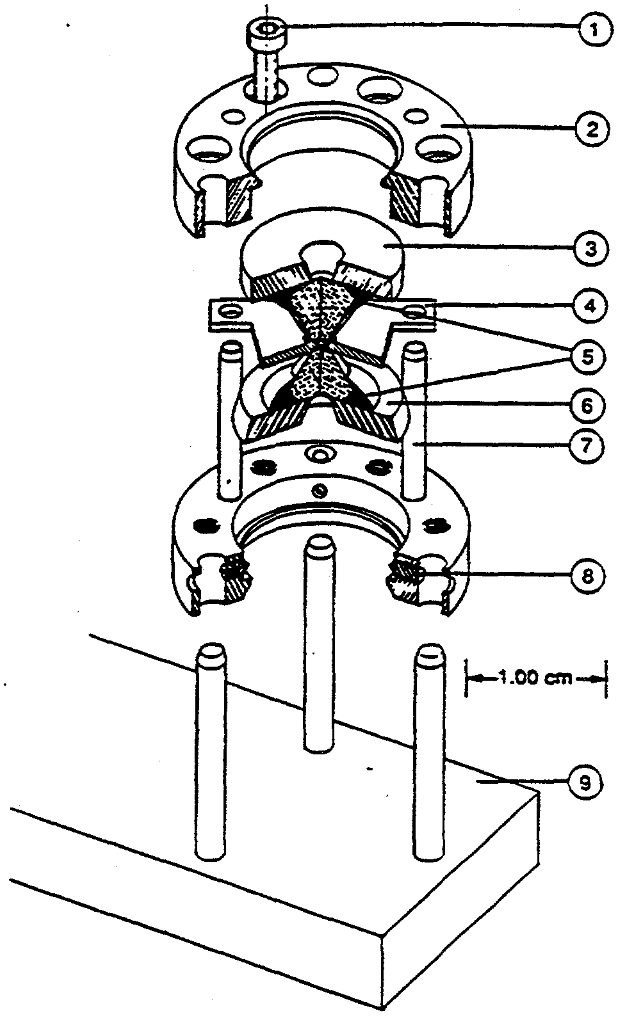

Figure 3.4. Exploded view of the modified Merrill-Basset diamond anvil cell: 1) Allen screws to generate pressure. 2) platens. 3) fixed backing plate. 4) gasket. 5) diamond anvils. 6) adjustable backing plate. 7) positioning and gasket holder pins. 8) set screws. 9) cell holder (Sterer. 1990).

The DAC which I use in this study is a modified Merrill-Bassett cell (Merrill and Bassett, 1974) (Sterer *et al.*, 1990), in which two platens are pulled together by six screws, pressing the diamonds against each other. The diamonds are mounted on backing plates with epoxy, and the backing plates are gold-plated with light-concentrating cones to focus the light on the sample. To ensure that the diamonds are aligned parallel to each other, before the gasket is inserted, the six screws are adjusted until the Newton interference fringes formed between the two diamond surfaces disappear. In addition, set screws (Figure 3.4) allow for translational adjustment of one of the diamonds. When the diamonds are properly aligned, the distances between the platens are measured in three locations with a micrometer and recorded for future reference.

3.3.1 Loading the Sample

I used 0.25 carat type I diamonds with flat octagonal culets 750 μm in diameter. Type I diamonds contain a nitrogen absorption band from 1100 to 1400 cm^{-1} (Seal 1984). Type II diamonds, which do not contain nitrogen, are transparent in that region of the spectrum but cost twice as much as type I diamonds. The gasket is made from stainless steel and is pre-indented to a thickness ranging from 50 to 100 μm. For 200 μm thick samples, I used heat-treated Cu-Be gaskets, pre-indented to a thickness of ~300μm. After the pre-indentation, a hole is drilled in the center of the pre-indented area with a #78 carbide drill. The sample and liquid nitrogen are then placed in the hole, along with a ruby chip for pressure calibration (Sec. 3.3.2). The screws are loosely adjusted so that the diamonds are properly aligned. Finally, the DAC is immersed in liquid nitrogen (Schiferl *et al.*, 1978) so that the nitrogen can seep into the sample space. Helium gas is continuously blown into the liquid nitrogen to suppress the formation of N_2 bubbles. The screws are then tightened so that the diamonds press down on the gasket and form a seal, trapping the nitrogen in the sample space.

3.3.2 Ruby Fluorescence Pressure Calibration

In high pressure x-ray studies, the lattice constants of NaCl and Ag are used as pressure markers. In Raman, photoluminescence, and infrared studies, however, the ruby fluorescence pressure calibration is commonly used. The R lines of Cr^{3+} in Al_2O_3 shift linearly with pressure (Forman *et al.*, 1972) up to 190 kbar (Piermarini *et al.*, 1975). Beyond 190 kbar, the shift in the R lines deviates from the linear approximation. The following empirical formula is used (Mao *et al.*, 1978) to determine the pressure:

$$P = 380.8\left\{\left[\lambda_P(T)/\lambda_0(T)\right]^5 - 1\right\}, \tag{3.30}$$

where P is the pressure in GPa, λ_P is the wavelength of the ruby R_1 line at pressure P and temperature T, and λ_0 is the corresponding wavelength at the same temperature and atmospheric pressure.

For infrared transmission studies performed at liquid helium temperatures, it is difficult to obtain the *in situ* pressure using ruby fluorescence, since the laser beam must enter the spectrometer and cryostat and the fluorescence must be detected by a monochromator. Although Chen and Weinstein (1996) have developed such a system, for mid-infrared measurements it is much easier to exploit the fact that infrared absorption peaks in the N_2 ambient shift linearly with pressure. In the following section I discuss the physics of N_2 under pressure at liquid helium pressures and give the quantitative pressure dependence of the infrared peaks (McCluskey *et al.*, 1996c). In all subsequent measurements in this thesis, these peaks are used as a precise *in situ* pressure calibration.

3.4 Infrared Absorption of Solid Nitrogen Under Pressure

3.4.1 Introduction

The development of high-pressure diamond-anvil cells has led to extensive experimental research on the properties of high density molecular solids (Polian *et al.*, 1989). N_2 is in many respects a model molecular system because its triple bond is very stable and its low atomic number simplifies theoretical calculations (Nosé and Klein, 1983). At low temperatures and pressures (Figure 3.5), N_2 crystallizes into the cubic α phase (space group *Pa3*) (Schiferl *et al.*, 1989). At pressures between 0.4 and 1.9 GPa, N_2 is in the tetragonal γ ($P4_2 / mnm$) phase (Medina and Daniels 1976, Thiéry *et al.*, 1973). For pressures higher than 1.9 GPa, x-ray diffraction (Mills *et al.*, 1986) and Raman (Schiferl *et al.*, 1985) studies have provided evidence that ε-N_2 has a structure which belongs to the rhombohedral space group $R\bar{3}C$. Theoretical studies predict that ε-N_2 has a tetragonal structure with 32 molecules per unit cell, but that the structure is very similar to $R\bar{3}C$ (Belak *et al.*, 1990). In the following sections I present the results of infrared absorption studies that lend further support to the $R\bar{3}C$ model.

The infrared absorption spectrum of solid nitrogen at normal vapor pressure has been measured in α-N_2 (Jodl *et al.*, 1987) and β-N_2 (Tryka *et al.*, 1995). The α and β phases have infrared absorption features near the fundamental N-N stretch frequency which are attributed to nonlinear coupling between the N-N vibrons and lower frequency phonons (Löwen *et al.*, 1990). Recently the profile of the N-N stretch overtone has been used to determine the temperature of solid nitrogen on the surface of Pluto (Tryka *et al.*, 1994). In this section, I discuss the observation of an infrared active peak in nitrogen in the high-pressure ε phase. In addition, for all measured pressures, I observe the ν_3 vibrational mode of CO_2 impurities. The pressure dependence of these peaks serve as a useful *in situ* pressure calibration in Sec. 5.1.2.

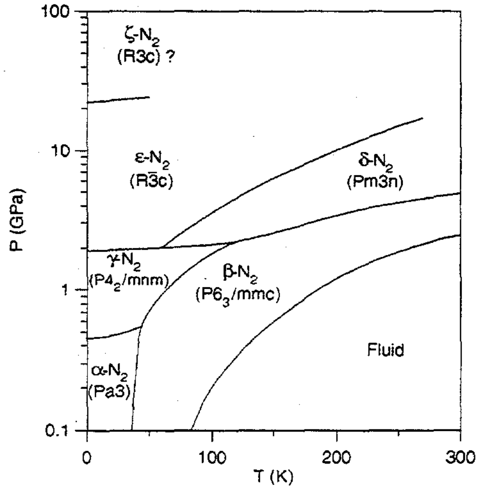

Figure 3.5. Phase diagram of nitrogen (Belak 1990).

3.4.2 Experimental Techniques

As discussed in Sec. 3.3, we used a modified Merrill-Basset diamond-anvil cell to generate pressures up to 7 GPa. The liquid-immersion technique was used to load the cell with liquid nitrogen. To determine the pressure at liquid-helium temperatures, a few grains of ruby were placed in the cell and on the outside face of one of the diamonds. The cell was then placed in a liquid-helium cryostat and the rubies were excited by an Argon ion laser. The ruby fluorescence was dispersed by a double monochromator and detected by a photomultiplier tube. The atmospheric and high pressure fluorescence lines were recorded by computer, and pressures were determined with the relation (4.30).

Following the fluorescence measurements, each sample was warmed to room temperature and then placed in the infrared spectrometer liquid-helium cryostat. Mid-infrared absorption spectra were obtained with a Digilab 80-E vacuum Fourier transform spectrometer with a KBr beamsplitter, with a spectral range of 450 to 3400 cm^{-1}. Spectra were taken at a temperature of 7 K with an instrumental resolution of 0.5 cm^{-1}. A light concentrating cone focused the light through the diamonds and sample into a Ge:Cu photoconductor mounted directly behind the sample.

To obtain a more precise measurement of the pressure, we loaded some diamond-anvil cells with AlSb:Se,C samples which were cut into discs 300 μm in diameter and polished to a thickness of 50 μm. The $^{12}C_{Sb}$ acceptor has a local vibrational mode (LVM) peak at 591.0 cm^{-1} at a temperature of 10 K and atmospheric pressure (Figure 3.6). Our samples are co-doped with Se so that they are *n*-type. Since Se is a deep donor

(Becla *et al.*, 1995), the free carriers freeze out at low temperatures, and the samples are infrared transparent even for high (~10^{17} cm^{-3}) concentrations of C_{Sb}. We assume that the position of the C_{Sb} LVM varies linearly with pressure, as is observed in the case of GaAs:Si_{Ga} (Wolk *et al.*, 1991). The observation that the pressure-induced shift of the C_{Sb} LVM varies linearly with the shifts of the CO_2 and N_2 vibrational modes (Figure 3.8) supports this assumption. We therefore use the position of the C_{Sb} LVM peak as a precise pressure calibration.

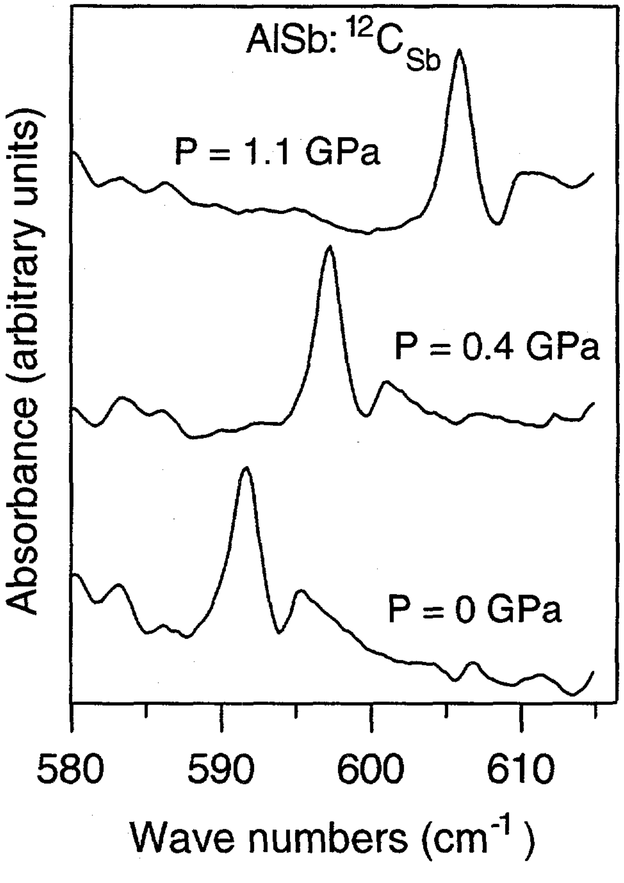

Figure 3.6. Pressure dependence of the AlSb:$^{12}C_{Sb}$ local vibrational mode (LVM) at a temperature of 10 K. The position of the LVM is used as an *in situ* pressure calibration.

3.4.3 Results

For all pressures, we observe an infrared absorption peak which we attribute to the ν_3 vibrational mode of CO_2 impurities in the N_2 matrix (Figure 3.7). In Figure 3.8, the open and filled circles refer to CO_2 vibrational frequencies measured by the C_{Sb} LVMs and ruby fluorescence lines, respectively. By matching the two sets of points, we obtain the relation

$$P = 0.073\ [\nu\ (C_{Sb}) - 591.0]\ , \tag{3.31}$$

where P is the pressure in GPa and $\nu\ (C_{Sb})$ is the position of the C_{Sb} LVM peak in cm^{-1} at liquid-helium temperatures. This pressure calibration is used in the subsequent analysis.

The pressure-induced phase transitions of solid N_2 can be inferred from discontinuities in the positions of the CO_2 and N_2 peaks (Figure 3.8). For low pressures, N_2 is in the α phase, and the CO_2 peak shifts linearly:

$$\nu_3\ (CO_2) = 2349.3 + 12.3\ P \qquad 0 \leq P \leq 0.45 \tag{3.32}$$

where $\nu_3\ (CO_2)$ is the frequency in cm^{-1} and P is the pressure in GPa. At 0.45 GPa, two CO_2 peaks are observed, indicating a coexistence of the α and γ phases. This transition pressure differs from the value obtained by Thiéry *et al.* (1973), who found a transition pressure of 0.35 GPa at a temperature of 4.2 K. Thiéry *et al.* determined the pressure by estimating the force per area of a piston-cylinder cell. Although they did not state the error in their pressure calibration, it is probably large enough to account for the discrepancy.

In the γ phase, the position of the CO_2 peak is best described by two piece-wise linear fits,

$$\nu_3(CO_2) = \begin{cases} 2347.6 + 8.4P & 0.45 \leq P \leq 1.3 \\ 2349.5 + 6.9P & 1.3 \leq P \leq 1.9 \end{cases} \tag{3.33}$$

The reason for the two linear regimes is currently not known. In the ε phase, the CO_2 peak shifts linearly:

$$\nu_3(CO_2) = 2345.1 + 6.6\,P \qquad 1.9 \leq P \leq 7 \tag{3.34}$$

In addition, a new infrared absorption peak appears (Figure 3.7). We attribute this new peak to a N-N stretch mode, since its frequency is similar to that of the Raman-active N-N stretch mode of solid nitrogen under pressure (Figure 3.8). In keeping with the notation of Schiferl, *et al.* (1985), we label this mode ν_3. The pressure dependence of the peak position can be described by a least-squares linear fit:

$$\nu_3(N_2) = 2326.5 + 2.7\,P \qquad 1.9 \leq P \leq 7 \tag{3.35}$$

The N-N stretch mode of a N_2 molecule in free space is not infrared active, since no electric dipole is induced by the symmetric vibration. In the γ phase, however, the symmetry is lowered so that a small dipole moment is induced by the N-N vibration. This is the first observation of an infrared active N-N stretch mode in solid nitrogen.

The infrared activity of this mode is consistent with the rhombohedral space group $R\bar{3}C$ (D_{3d}^6), which has one infrared-active and three Raman-active stretch modes (Table 3.1). N_2 molecules on the 2b site have one Raman-active stretch mode while those on the 6e site have two Raman-active modes and one infrared-active mode. Previous Raman studies have only revealed two of the three Raman-active peaks (Schiferl *et al.*, 1985), perhaps because the frequency difference between the A_{1g} and E_g modes is too small to be resolved. The ν_3 infrared-active mode has a frequency very similar to the ν_2 Raman-active mode (Figure 3.8), an observation which suggests that they both arise from N_2 molecules on the 6e site. If that is the case, then the factor group splitting is much smaller than the site splitting for the $R\bar{3}C$ structure. The absence of a N-N infrared-active absorption peak for pressures below 1.9 GPa is consistent with the symmetries of the cubic α phase *Pa3* (Schiferl *et al.* 1989) and tetragonal γ phase $P4_2/mnm$ (Medina and Daniels 1976).

Table 3.1. Correlation diagram for the N-N stretch mode of solid nitrogen in the ε ($R\bar{3}C$) phase, at the center of the Brillouin zone.

Site	Molecular Symmetry	Site Symmetry	Factor Group Symmetry	Activity
2b	$D_{\infty h}$	$S_6 \equiv C_{3i}$	D_{3d}	
	Σ_g^+ (N-N stretch) →	A_g →	A_{1g} (1)	Raman
			A_{2g} (1)	--
6e	$D_{\infty h}$	C_2	D_{3d}	
	Σ_g^+ (N-N stretch) →	A →	A_{1g} (1)	Raman
			E_g (1)	Raman
			A_{1u} (1)	--
			E_u (1)	Infrared

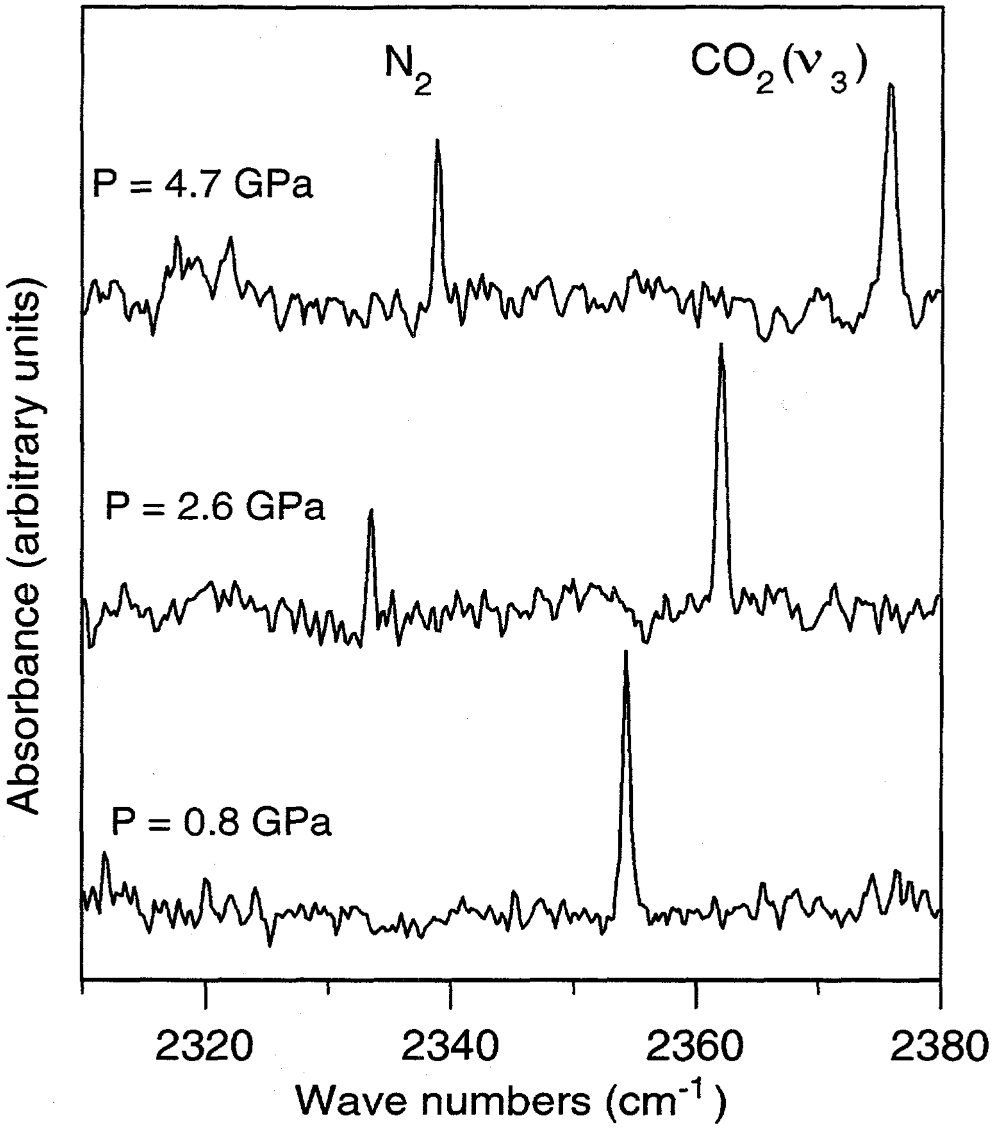

Figure 3.7. Infrared absorption spectra of solid nitrogen under pressure. For all measured pressures, the ν_3 vibrational mode of CO_2 impurities is observed. For pressures above 1.9 GPa, the N-N stretch mode becomes infrared-active.

3.4.4 Conclusions

In conclusion, we have observed infrared absorption peaks in solid nitrogen under large hydrostatic pressures and liquid-helium temperatures. The ν_3 mode of CO_2 was observed for all measured pressures. For pressures greater than 1.9 GPa, we observe the N-N stretch mode of solid nitrogen in the ε ($R\bar{3}C$) phase. Using the shift of the AlSb:$^{12}C_{Sb}$ LVM as an *in situ* pressure calibration, we measured the pressure-dependent shifts of the CO_2 and N_2 vibrational modes. These shifts are used as a precise pressure calibration for infrared absorption experiments.

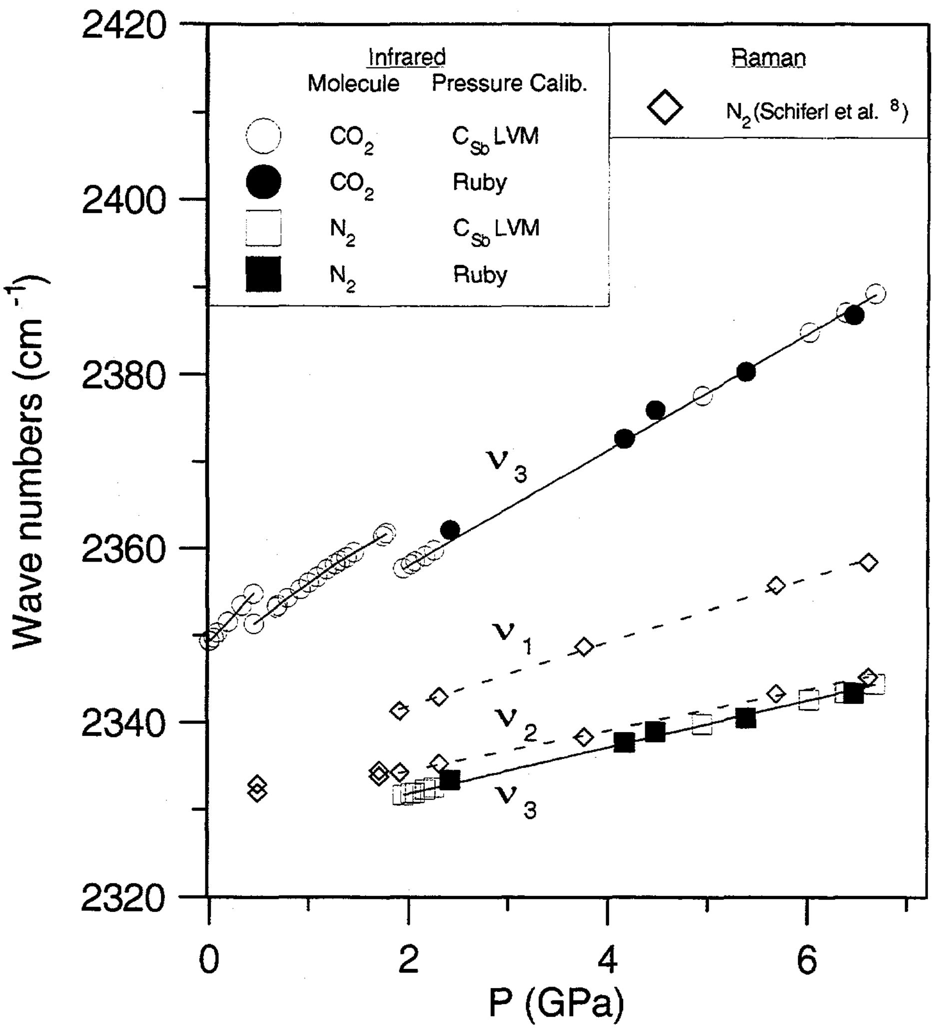

Figure 3.8. Positions of the CO_2 and N_2 infrared absorption peaks in nitrogen under pressure at liquid-helium temperatures. For the solid circles and squares, ruby fluorescence was used as a pressure calibration (Eq. 4.30). For the open circles and squares, the position of the AlSb:$^{12}C_{Sb}$ local vibrational mode (LVM) was used to calibrate the pressure (Eq. 4.31). The open diamonds are Raman-active modes measured by Schiferl, *et al.* (1985) at a temperature of 15 K. The solid lines are linear fits given in Eq. 4.32-4.35 and the dashed lines are guides to the eye. The discontinuities near 0.45 and 1.9 GPa are due to structural phase transitions.

4. Hydrogen Related Complexes in Compound Semiconductors

4.1 Acceptor-Hydrogen Complexes in GaP

4.1.1 Introduction

Although most studies of LVMs in compound semiconductors have focused on GaAs and InP (Sec. 1.4), significant work has also been done on hydrogen LVMs in GaP. Clerjaud *et al.* (1991) observed the C-H and C-D bond-stretching LVMs and the N-H mode (1992) in GaP grown by the liquid-encapsulation Czochralski (LEC) technique. LVMs corresponding to hydrogen-defect complexes in LEC-grown GaP have also been observed (Dischler *et al.*, 1991). McCluskey *et al.* reported LVMs corresponding to zinc-hydrogen (1994a) and beryllium-hydrogen (1994b) complexes in GaP. In the following sections, I discuss the modes arising from beryllium-, zinc-, and cadmium-hydrogen complexes and compare them to similar complexes in GaAs and InP. In addition, I describe a simple model which accounts for the temperature dependence of the hydrogen LVMs (McCluskey *et al.*, 1995).

The GaP samples used for this study had a (100) orientation and were n-type, with a sulfur concentration of approximately 10^{17} cm^{-3}. GaP:Be samples were obtained by implanting the undoped samples with 40 keV beryllium ions at a dose of 5 X 10^{14} cm^{-2}, and 100 and 200 keV ions at doses of 1 X 10^{15} cm^{-2} each, for a total dose of 2.5 X 10^{15} cm^{-2}. To activate the beryllium acceptors, the implantation was followed by rapid thermal annealing at 1000°C for 10 s. To obtain GaP:Zn, the undoped samples were placed in a 100 ml evacuated quartz ampoule with 0.5 g metallic zinc and diffused in a vertical furnace for 10 min at a temperature of 860°C. After completion of the diffusion, the samples were quenched to room temperature by dropping the ampoule into ethylene glycol. To obtain GaP:Cd, the undoped samples were placed with 200 mg cadmium and 1/3 atm H_2 ambient in an ampoule and diffused for 22 hr at a temperature of 950°C, followed by quenching to room temperature. Room temperature Hall effect measurements with the Van der Pauw geometry indicated sheet hole concentrations of p(Be) = 1 X 10^{15} cm^{-2}, p(Zn) = 5 X 10^{15} cm^{-2}, and p(Cd) = 2 X 10^{14} cm^{-2}.

Some of the samples were then exposed to monatomic hydrogen or deuterium in a remote plasma system as described in Sec. 1.5.2. The hydrogenation temperature was 300°C and the duration of the exposure was 1 hr. GaP samples which were doped p-type but not H- or D-plasma exposed were used as reference samples.

Infrared absorption spectra were obtained at liquid helium temperature with a Digilab 80-E vacuum Fourier transform spectrometer with a KBr beamsplitter and an instrumental resolution of 0.25 cm^{-1}. A Ge:Cu photoconductor was used as a detector. For temperatures above 10 K, spectra were obtained with a Bomem DA8 spectrometer with a KBr beamsplitter and external mercury cadmium telluride (MCT) detector. The instrumental resolution for the variable temperature measurements ranged from 0.5 to

1 cm^{-1}.

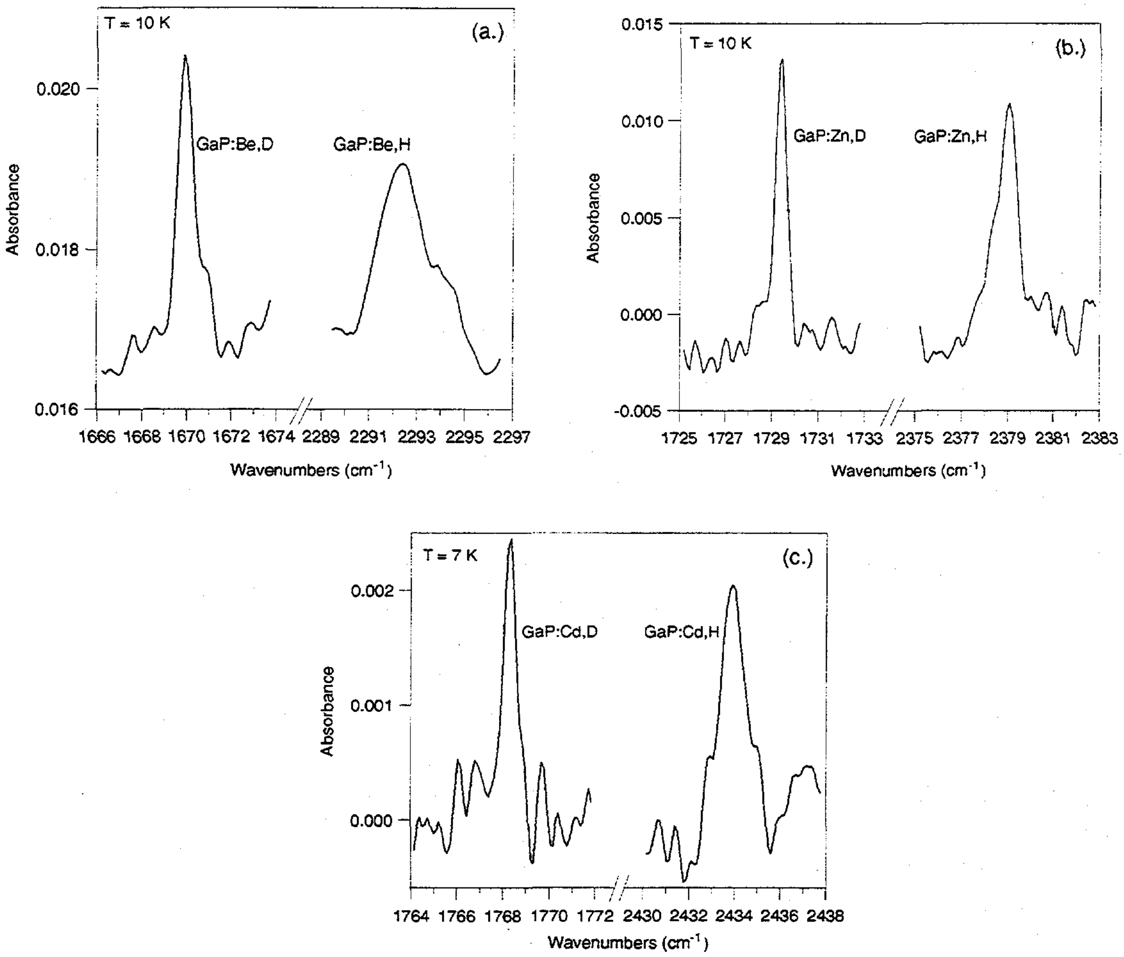

Figure 4.1. Infrared absorption spectra of deuterated and hydrogenated (a.) GaP:Be. (b.) GaP:Zn. and (c.) GaP:Cd. The vibrational modes are associated with P-H (P-D) complexes adjacent to the group II acceptors.

4.1.2 Results

Hydrogenated and deuterated GaP:Zn samples have infrared absorption peaks at 2379.0 and 1729.4 cm^{-1}, respectively (Figure 4.1b). The isotopic ratio of these frequencies, $r = \nu_H/\nu_D$, is 1.3756. By way of comparison, hydrogenated InP:Zn has a bond-stretching mode at 2287.7 cm^{-1} and an isotopic ratio r = 1.3744 (Darwich *et al.*, 1993). The bond-stretching mode has been attributed to a P-H complex oriented along a [111] bond-centered direction, adjacent to the zinc acceptor, with the zinc relaxed into the plane of phosphorus atoms (Figure 4.2). Since the LVMs and the r-factor for GaP:Zn are similar to the corresponding values for InP:Zn, we assume that the structures are the same. The P-H model receives further support from the observation that the Zn-H bond-stretching frequency is 1600 cm^{-1}, far lower than the P-H bond-stretching mode of phosphine, which is 2328 cm^{-1}.

The hydrogenated and deuterated GaP:Be samples have infrared absorption peaks at 2292.2 and 1669.8 cm^{-1}, respectively, at a temperature of 10 K (Figure 4.1a). The isotopic ratio of these frequencies is r = 1.3727. Neither peak was seen in GaP:Be which was not H- or D-plasma exposed. These values are similar to the corresponding values in InP:Be, which has a P-H bond-stretching mode at 2236.5 cm^{-1} and isotopic ratio r = 1.3714. We therefore assume that the absorption peaks arise from a P-H complex, oriented in a bond-centered direction, adjacent to the beryllium acceptor.

The hydrogenated and deuterated GaP:Cd samples have infrared absorption peaks at 2434.0 and 1768.3 cm^{-1}, respectively, at a temperature of 7 K (Figure 4.1c). The isotopic ratio of these frequencies is r = 1.3765. Although the samples were diffused in a H_2 ambient, GaP:Cd which was not exposed to a hydrogen plasma did not have the hydrogen related absorption peak. Once again, these values are similar to the corresponding values for InP:Cd, which has a P-H bond-stretching mode at 2332.4 cm^{-1} and isotopic ratio r = 1.3757. It therefore appears that for all group II acceptor-hydrogen complexes in GaAs (Rahbi *et al.*, 1993), InP, and GaP, the hydrogen binds to the host anion in a [111] bond-centered orientation.

The positions and FWHM of the observed peaks are listed in Table 4.2. The FWHMs of the P-D peaks are smaller than those of the P-H peaks. This narrowing effect has been observed in all group II acceptor-hydrogen complexes in III-V semiconductors and is correlated with the smaller vibrational amplitude of the deuterium as compared to the hydrogen. It has been suggested (Chevallier, 1991) that the smaller vibrational amplitude of deuterium leads to a weaker coupling with the lattice and thus an increase in the lifetime. Other hydrogen/deuterium-related complexes do not follow this trend, however, so the question is still open.

In addition to the change in linewidth, several trends are immediately apparent. First, the P-H modes in GaP are higher than the corresponding P-H modes in InP (Figure 4.3a). This is due to the fact that GaP has a smaller lattice constant than InP. Second, as the size of the group II acceptor increases, the frequency of the P-H mode increases. The significant upward shift in frequency is evidence for hydrogen residing in a bond-centered, rather than an antibonding, position. As explained below, as the acceptor atomic number increases from Be to Cd, the acceptor-hydrogen bond is compressed, increasing the LVM frequency. Finally, the isotopic ratio $r = \nu_H/\nu_D$ increases with increasing acceptor mass (Figure 4.3b). Darwich *et al.* (1993) noted that the anharmonicity decreases from Be to Cd, increasing *r* (Sec. 2.3.4).

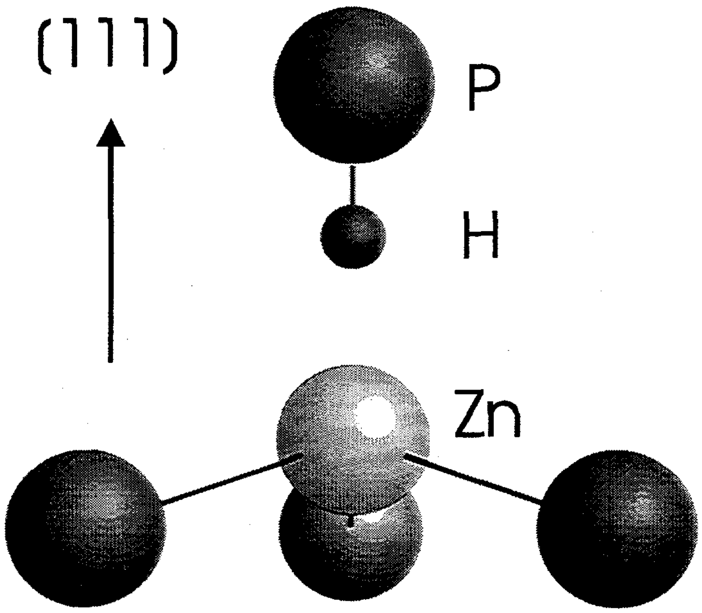

Figure 4.2. Model for H passivation of the Zn acceptor with the H atom attached to a P atom in a bond-centered orientation. This model applies for all observed group II acceptor-hydrogen complexes in GaP and InP.

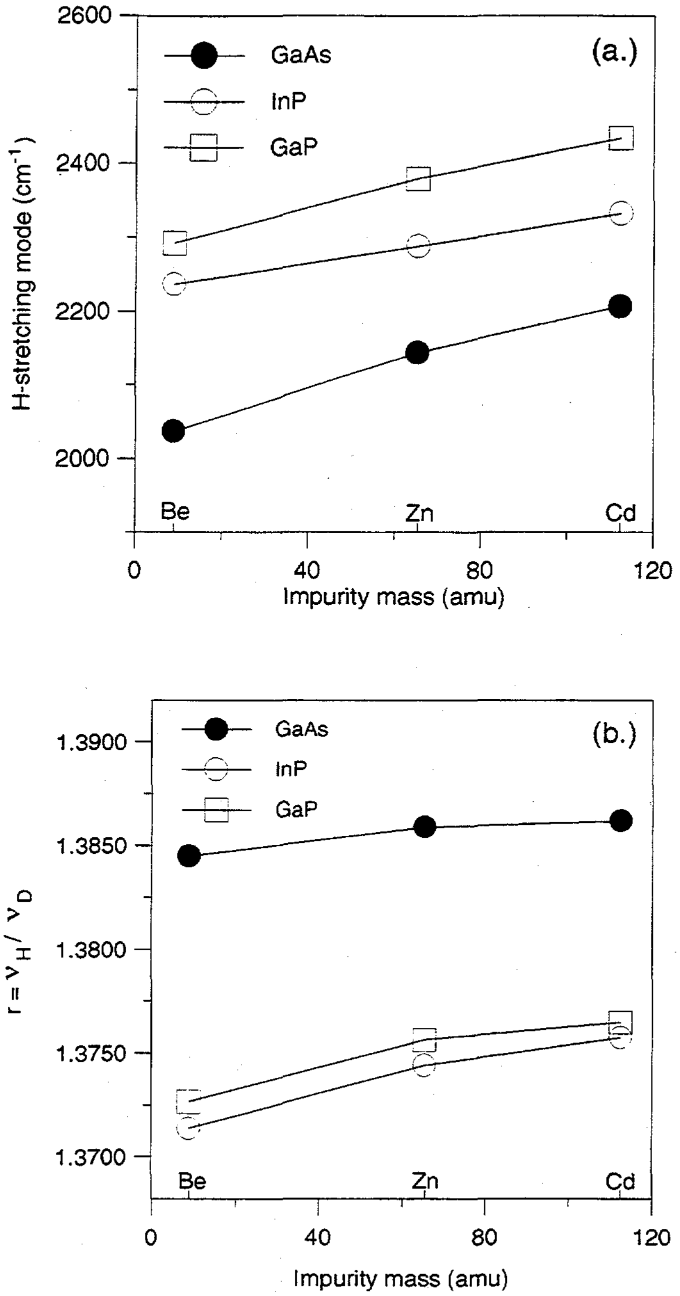

Figure 4.3. (a.) Hydrogen bond-stretching modes for group II acceptor-hydrogen complexes in GaAs, InP, and GaP. Note that the LVM frequency shifts upward with increasing acceptor size, evidence that the hydrogen is in a bond-centered orientation. (b.) Isotopic ratio $r = \nu_H/\nu_D$. As the size of the acceptor increases, so does the r-factor.

4.1.3 Bond Compression

The increase in the hydrogen LVM frequency can be described empirically by considering the equilibrium bond lengths of the diatomic molecules BeH, ZnH, and CdH. I define the *compression factor*

$$\Delta = d(X\text{-H}) + d(Y\text{-H}) - d_{nn}, \tag{4.1}$$

where X is Be, Zn, or Cd, Y is P or As, and $d(X\text{-H})$ and $d(Y\text{-H})$ are equal to the molecular bond lengths (Table 4.1). d_{nn} is the nearest neighbor lattice distance, given by

$$d_{nn} = \sqrt{3}a / 4, \tag{4.2}$$

where a is the lattice constant. This simple model does not account for the distribution of between the X-H and Y-H bonds or the influence of other atoms in the lattice.

Table 4.1. Equilibrium bond lengths of free molecules (Rosen 1970) and semiconductors (Landolt-Börnstein, 1987).

Bond	Length (Å)
Free Molecules	
P-H	1.42
As-H	1.52
Be-H	1.30
Zn-H	1.59
Cd-H	1.76
Semiconductors	
GaP	2.36
InP	2.54
GaAs	2.45

Δ is a crude measure of how much the bonds are compressed. As Δ increases, the LVM frequency and *r* value increase. Figure 4.4 shows the LVM frequencies and *r* values as a function of Δ for acceptor-hydrogen complexes in GaAs, GaP, and InP. For GaAs and GaP, the LVMs vary linearly with Δ. The *r* values for GaP and InP lie on the same curve, since the complexes are so similar. In the future, it would be interesting to use hydrostatic pressure to determine whether varying d_{nn} has the same effect as varying the acceptor species.

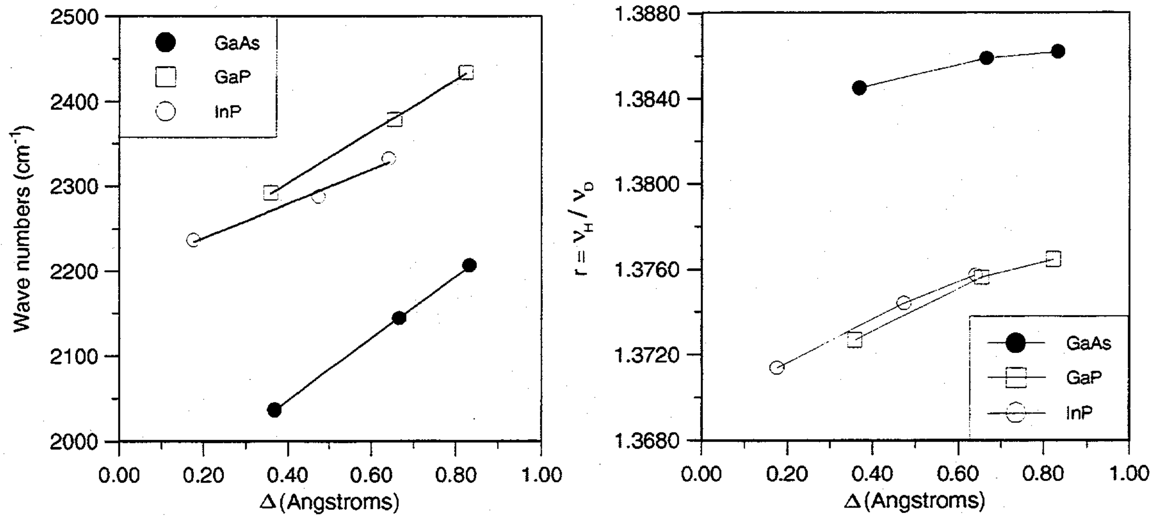

Figure 4.4. LVM frequencies and *r* values for group II acceptor - hydrogen complexes in GaAs, GaP, and InP as a function of bond compression Δ.

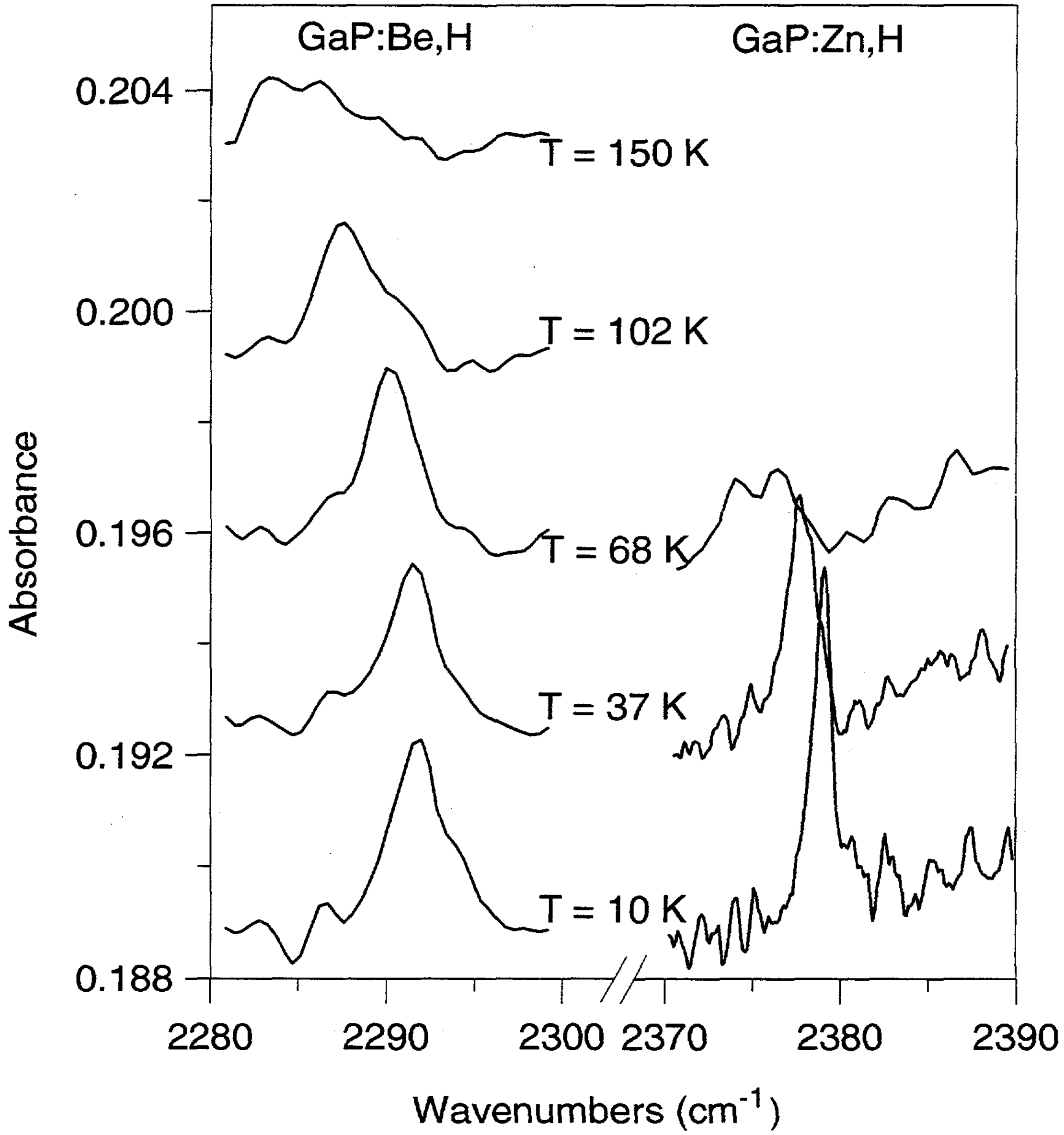

Figure 4.5. Variable temperature spectra of GaP:Be,H and GaP:Zn,H LVMs. The LVM shift and linewidth broadening of the GaP:Zn,H mode is much greater than the GaP:Be,H mode.

4.1.4 Temperature Dependence of LVMs

The temperature dependence of the hydrogen related LVMs in GaP:Be and GaP:Zn was observed between 7 and 150 K (Figure 4.5). Unfortunately, the small signal-to-noise ratio of the GaP:Cd,H LVM precluded variable temperature measurements. We obtained the frequencies and linewidths of the peaks by fitting the data to Lorentzian functions. The linewidth broadening and shift to lower energy with increasing temperature have been observed in numerous systems and are believed to be caused by anharmonic coupling between the localized mode and the extended lattice phonons. The temperature dependence of hydrogen LVMs in GaAs (Tuncel and Sigg, 1993) and InP (Darwich *et al.*, 1993) has been explained with a model which assumes that the LVM interacts with a *single* phonon mode. In our case, however, we assume that the LVM interacts with *all* the phonons and does not couple preferentially to any one mode.

Elliot *et al.* (1965) quantitatively described the temperature dependence of LVMs in alkali halides. In our case, we assume that the hydrogen's potential is perturbed by the neighboring acceptor. The phosphorus-acceptor distance is given by

$$x(t) = x_o + \delta x(t), \tag{4.3}$$

where x_o is the equilibrium distance, $\delta x(t)$ is a perturbation due to thermal fluctuation, and t is time. The resultant shift in the LVM energy can be expanded in a Taylor series about small δx:

$$\delta\left(\hbar\omega(t)\right) = a(\delta x) + b(\delta x)^2 + \cdots \tag{4.4}$$

When averaged over time, the linear term does not contribute to the LVM shift. To lowest order, the shift is given by

$$\delta\,(\hbar\omega) = b\left\langle (\delta\, x)^2 \right\rangle\ . \tag{4.5}$$

$\left\langle (\delta\, x)^2 \right\rangle$ is calculated by summing the contributions from all the lattice modes **q**:

$$\left\langle (\delta\, x)^2 \right\rangle = \sum_{\mathbf{q}} \left\langle (\delta\, x_{\mathbf{q}})^2 \right\rangle = \sum_{\mathbf{q}} A_{\mathbf{q}}{}^2/2\ , \tag{4.6}$$

where $A_{\mathbf{q}}$ is the amplitude of vibration. In this simple model, the lattice modes are assumed to be unperturbed by the defect. Classically, the mean vibrational energy of the crystal is given by

$$U(T) = \frac{N}{2}\gamma \sum_{\mathbf{q}} A_{\mathbf{q}}{}^2 \tag{4.7}$$

where N is the number of atoms and γ is the nearest-neighbor force constant. From Eqs. 4.5-4.7, it can be seen that the LVM shift is proportional to the thermal lattice energy $U(T)$. Eq. 4.5 can therefore be written as

$$\delta\,(\hbar\omega) = \frac{\beta}{N_A} U(T) \tag{4.8}$$

where $U(T)$ is given in units of energy per mole, N_A is Avagadro's number, and β is a dimensionless constant. Roughly speaking, β is the fraction of thermal energy that is transferred to the hydrogen's vibrational motion from its neighboring atoms.

Figure 4.6 shows the LVM shifts plotted against $U(T)$. We obtained the values of $U(T)$ by numerically integrating the reported experimental values of the specific heat $C_V(T)$ (Irwin and LaCombe, 1974), neglecting the zero temperature energy. The data can be approximated by linear least-squares fits, with coefficients given in Table 4.3. Evidently, the larger zinc acceptor has more influence than the beryllium on the LVM frequency.

The temperature dependent increase of the linewidth is determined by the lifetime of the mode. It is unlikely that the hydrogen related LVMs decay via the creation of phonons, since at least six optical phonons would be required to conserve energy. Instead, elastic phonon scattering reduces the lifetime of the over-all mode (Barker and Sievers, 1975). This process is given by

$$|1\rangle|\ldots n_q, n_{q'}, \ldots\rangle \to |1\rangle|\ldots n_q + 1, n_{q'} - 1, \ldots\rangle \tag{4.9}$$

where $|1\rangle$ is the LVM and the n_q's are the phonon modes. In the Debye approximation, this process leads to a temperature dependent linewidth

$$\delta\,\Gamma = \Gamma(T) - \Gamma(0) = A\left(\frac{T}{\theta_C}\right)^7 \int_0^{\theta_C/T} \frac{z^6 e^z}{\left(e^z - 1\right)^2}\,dz \tag{4.10}$$

where $k\theta_C/\hbar$ is an effective cutoff frequency and A is an empirical constant. These two parameters have been adjusted to give reasonable fits to the data (Table 4.3). The value of $\theta_C = 400$ K that we used is physically reasonable, since the Debye temperature for GaP ranges from 300 to 500 K as the sample is warmed from 10 to 150 K. The data and the fits are plotted in Figure 4.8. Again, it can be seen that the GaP:Zn,H LVM is more sensitive to temperature variation than the GaP:Be,H LVM.

It should be noted that the thermal expansion of the lattice may contribute to the temperature-dependent shifts of the hydrogen LVMs. From 0 to 125 K, however, the lattice constant increases by only $\Delta a/a \sim 10^{-4}$ (Landolt-Börnstein, 1987). From hydrostatic pressure measurements done on GaAs:Si (Wolk *et al.*, 1991), it can be shown that a strain of $-\Delta a/a = 10^{-4}$ yields a LVM shift of less than 0.1 cm^{-1}. It is therefore unlikely that the small lattice expansion from 0 to 125 K plays a dominant role in the LVM shifts.

4.1.5 Conclusions

In conclusion, we have discovered vibrational modes in GaP:Be, GaP:Zn, and GaP:Cd exposed to H- and D-plasma. It appears that for all observed group II acceptor-hydrogen complexes in III-V semiconductors, the hydrogen binds to the host anion in a bond-centered orientation. The temperature dependent shifts of the LVMs are proportional to the lattice thermal energy $U(T)$, an observation which probably holds for hydrogen LVMs in other semiconductors as well.

Table 4.2. Frequencies and FWHM of P-H and P-D LVM peaks in group II acceptor-hydrogen complexes in GaP and InP.

	P-H stretch mode		P-D stretch mode		
Compound	Peak (cm^{-1})	FWHM (cm^{-1})	Peak (cm^{-1})	FWHM (cm^{-1})	$r=\nu_H/\nu_D$
GaP:Be	2292.2	2.7	1669.8	0.8	1.3727
GaP:Zn	2379.0	1.1	1729.4	0.5	1.3756
GaP:Cd	2434.0	1.2	1768.3	0.6	1.3765
InP:Be[a]	2236.5	0.43	1630.9	0.2	1.3714
InP:Zn[a]	2287.7	0.23	1664.5	0.08	1.3744
InP:Cd[a]	2332.4	0.12	1695.4	0.10	1.3757

[a] See Darwich *et al.* (1993).

Table 4.3. Parameters from Eqs. (4.8) and (4.10) which describe the temperature dependence of the GaP:Be,H and GaP:Zn,H LVMs.

LVM	β	θ_C (K)	*A* (cm^{-1})
GaP:Be,H	-0.050	400	200
GaP:Zn,H	-0.15	400	4900

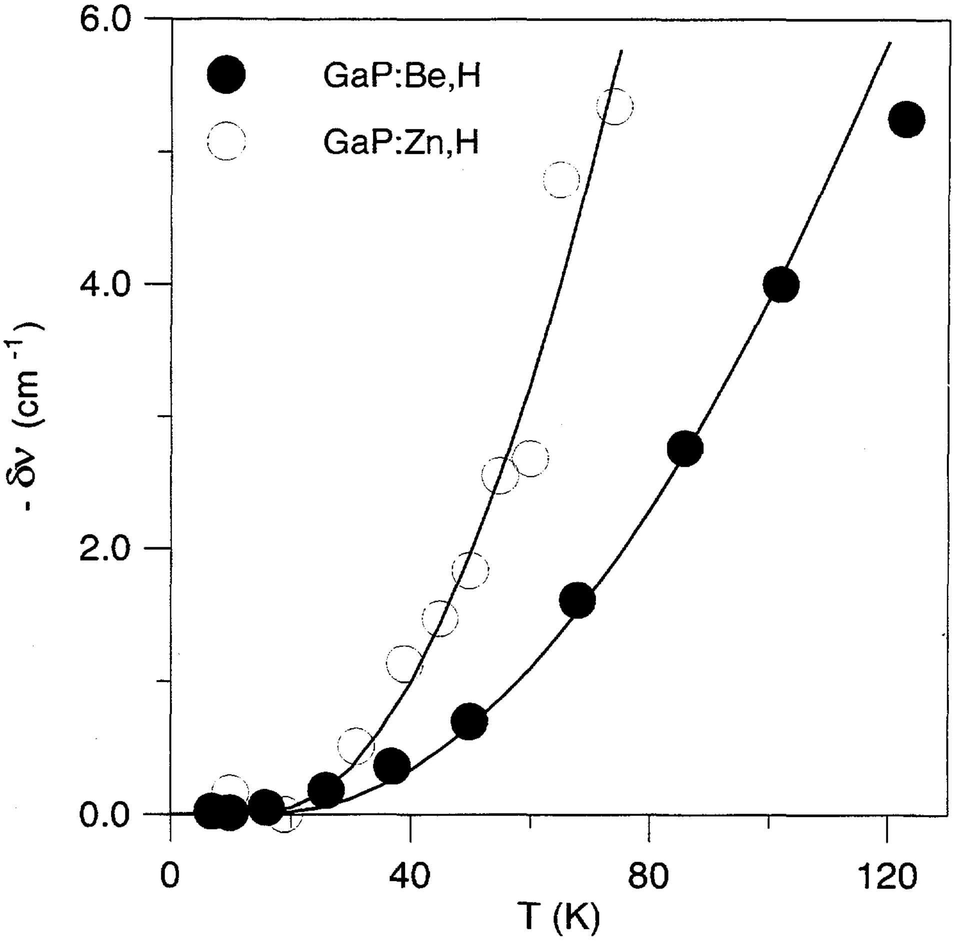

Figure 4.6. Shifts of the GaP:Be.H and GaP:Zn.H LVMs as a function of temperature. The solid lines are fits according to Eq. 4.8, with the β parameters given in Table 4.3.

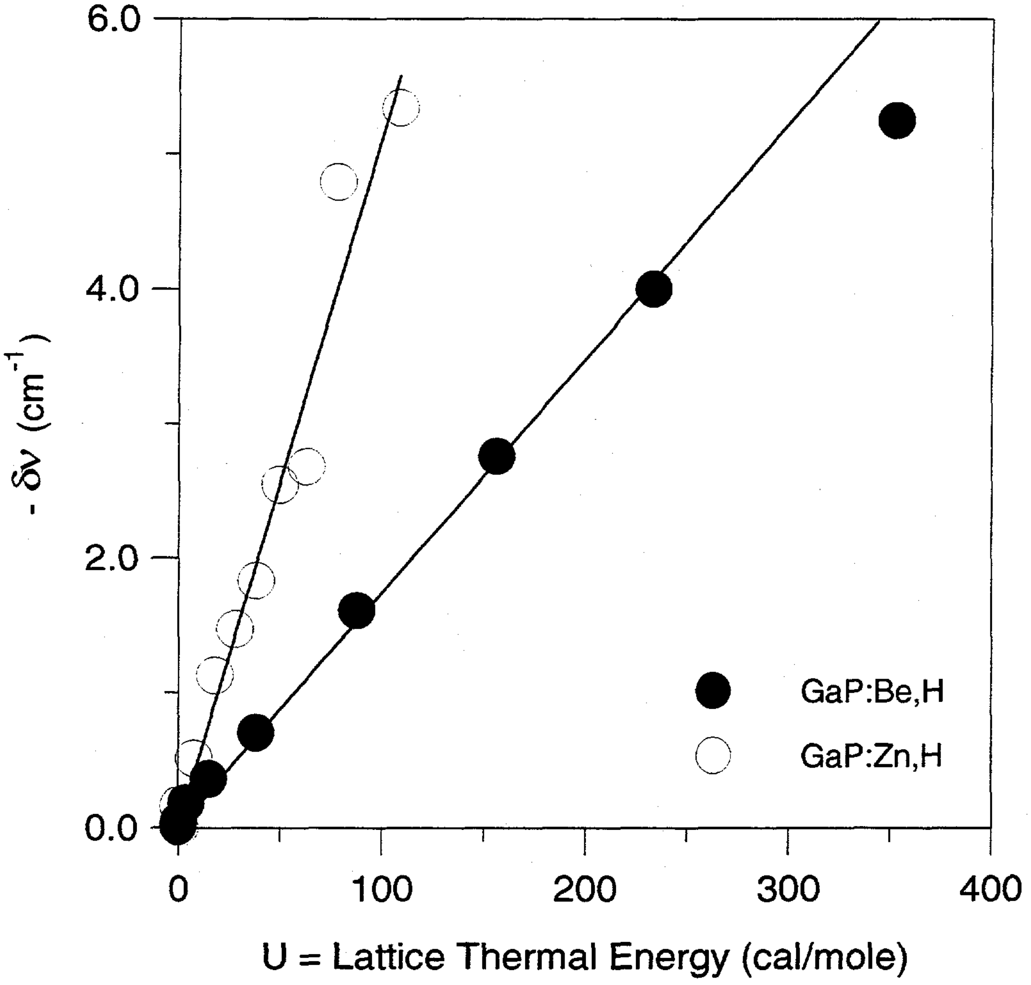

Figure 4.7. Shifts of the GaP:Be,H and GaP:Zn,H LVMs as a function of lattice thermal energy *U*(*T*). The solid lines are fits according to Eq. 4.8, with the β parameters given in Table 4.3.

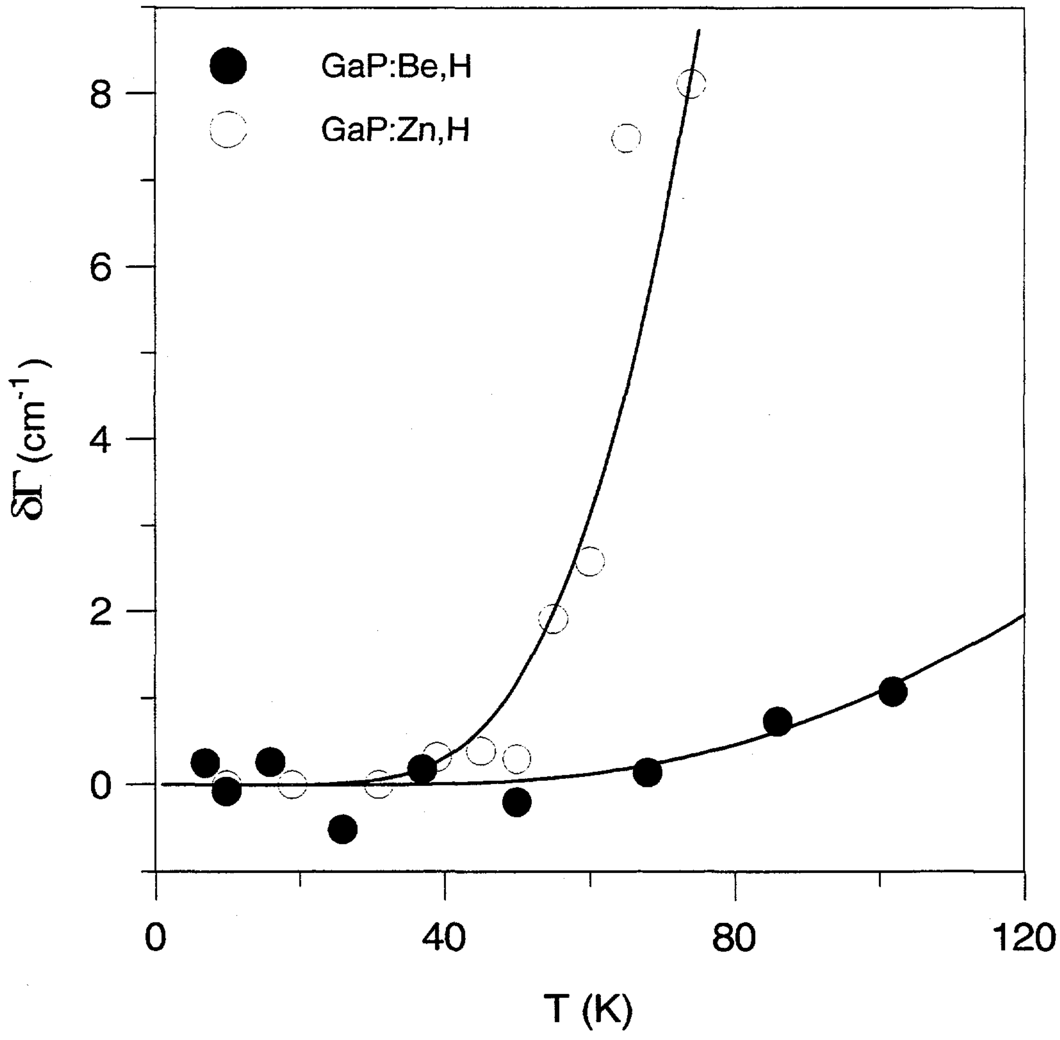

Figure 4.8. Temperature dependent shifts of the linewidth δΓ for the GaP:Be,H and GaP:Zn,H modes. The solid lines are fits according to Eq. 4.10. with the θ_C and *A* parameters given in Table 4.3.

4.2 Arsenic-Hydrogen Complexes in ZnSe

4.2.1 Introduction

The interest in developing blue light-emitting diodes and diode lasers has focused a great deal of research on the growth and doping of wide-band-gap semiconductors. Continuous wave ZnSe-based laser diodes have been fabricated from epilayers grown by molecular beam epitaxy (MBE), with high p-type doping achieved using a radio frequency plasma nitrogen source (Park *et al.*, 1990; Ohkawa *et al.*, 1992). Epilayers grown by metalorganic chemical vapor deposition (MOCVD), however, have proved resistant to p-type doping (Morimoto and Fujino, 1993; Nishimura *et al.*, 1993). Hydrogen plays a role in neutralizing the nitrogen acceptors, as shown by the observation of the local vibrational mode (LVM) of the N-H complex in MOCVD-grown ZnSe layers (Wolk *et al.*, 1993; Kamata *et al.*, 1993). Although arsenic-doped bulk ZnSe has only deep-level photoluminescence peaks (Watts *et al.*, 1971), there is evidence that arsenic has a shallow acceptor level in ZnSe epilayers grown by MBE (Li *et al.*, 1994). The incorporation of hydrogen in arsenic and nitrogen doped MOCVD-grown ZnSe has been studied by secondary ion mass spectrometry (SIMS) (Bourret 1996). In this chapter, I discuss the observation of LVMs of As-H complexes in ZnSe (McCluskey *et al.*, 1996a).

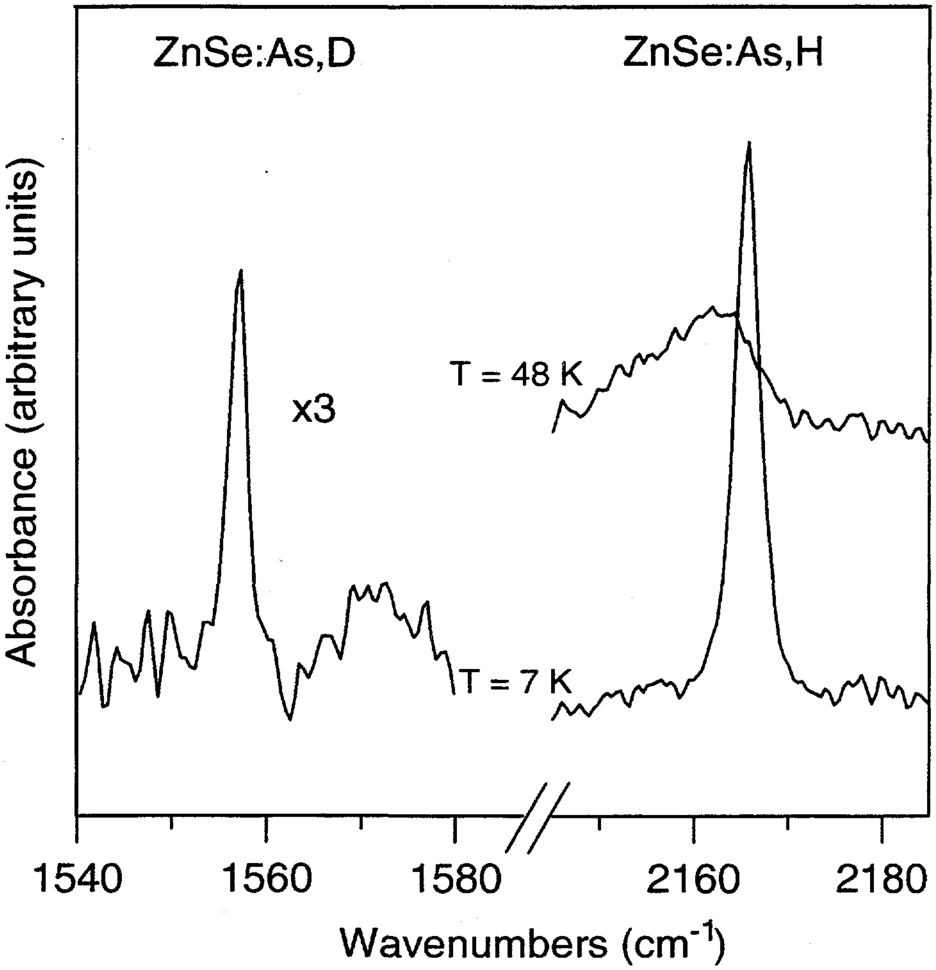

Figure 4.9. Infrared absorption peaks corresponding to the LVMs of As-H and As-D complexes in MOCVD-grown ZnSe. The shift and linewidth broadening of the As-H LVM at higher temperatures is due to interactions with the lattice phonons (see text).

The epitaxial ZnSe films were deposited on (100) GaAs substrates by MOCVD. The precursors to ZnSe were diisopropylselenide (DIPSe) and diethylzinc (DEZn) and the source of arsenic was tertiarybutylarsine (TBA). Pd-purified hydrogen, deuterium, or high-purity nitrogen was used as the carrier gas. The growth temperature was 464°C, the molar flow ratio DIPSe/DEZn was 4, and the layers were ~3 μm thick.

4.2.2 Results

The sample that was grown with hydrogen as a carrier gas has an infrared absorption peak at 2165.6 cm^{-1} at a sample temperature of 7 K. When nitrogen is used as a carrier gas, we find the same peak, but its area is reduced by a factor of 14, in good agreement with SIMS measurements (Bourret 1996) which show that the sample grown with hydrogen has [H] = 1.5 X 10^{19} cm^{-3} while the sample grown with nitrogen has [H] = 1 X 10^{18} cm^{-3}. In this case, the hydrogen most likely comes from the metalorganic molecules. The sample that was grown with deuterium as a carrier gas has an absorption peak at 1557.1 cm^{-1}, along with the hydrogen-related peak at 2165.6 cm^{-1} (Figure 4.9). The isotopic ratio is $r = \nu_H / \nu_D = 1.3908$. The peak positions, widths, areas, and *r* values of the LVMs are given in Table 4.1. The area of the hydrogen-related peak is approximately 3 times that of the deuterium-related peak. Previous SIMS measurements of the samples show [H] = 6 X 10^{18} cm^{-3} and [D] = 1 X 10^{18} cm^{-3} (Bourret 1996). These results indicate that most of the hydrogen incorporation comes from by-products of reactions involving the hydrogen carrier gas and the metalorganic molecules. A sample which was grown at a lower temperature (360°C) contains high concentrations of hydrogen and arsenic ([H] = 3 X 10^{20} cm^{-3} and [As] = 1.8 X 10^{21} cm^{-3}) but does not show the hydrogen-related peak. At the lower growth temperature, hydrogen may be incorporated in forms that are infrared inactive, such as interstitial H_2 molecules.

The hydrogen bond-stretching mode frequencies of the free molecules H_2Se, AsH_3, and ZnH are 2345, 2116 (Shimanouchi 1972), and 1553 cm^{-1} (Rosen 1970), respectively. Since the frequency of the ZnSe:As,H mode is 2165.6 cm^{-1}, we propose that the hydrogen binds directly to the arsenic acceptor. In several respects, the As-H complex in ZnSe is similar to the Zn-H complex in GaAs (Chevallier *et al.*, 1991). In GaAs, zinc is an acceptor which occupies a substitutional gallium site. Hydrogen passivates zinc by attaching to a host arsenic atom, in a bond-centered orientation, adjacent to the zinc acceptor. In ZnSe:As it is likely that the hydrogen attaches to the arsenic acceptor, in a bond-centered orientation, adjacent to the host zinc atom (Figure 4.10). The stretch mode of the GaAs:Zn,H complex is 2146.0 cm^{-1} at a temperature of 6 K and the isotopic ratio is $r = 1.3860$ (Table 4.4). The fact that the isotopic ratios and LVM frequencies of the two complexes are very similar lends further support to the bond-centered model.

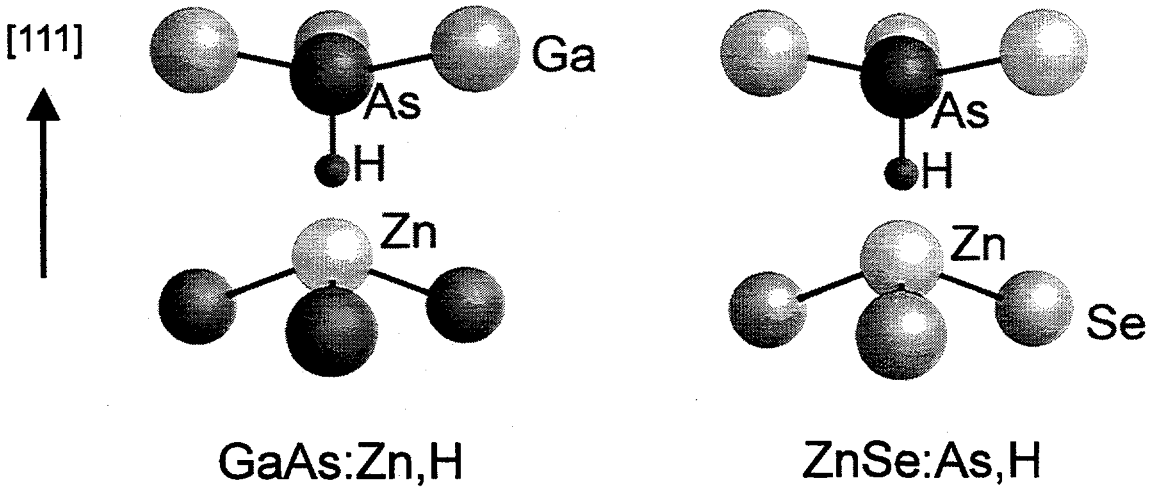

Figure 4.10. Model of ZnSe:As,H complex, as compared with the GaAs:Zn,H complex. In both complexes, the hydrogen resides in a bond-centered orientation between an arsenic and a zinc.

4.2.3 Temperature Dependence

The temperature dependent behavior of the ZnSe:As,H LVM is shown in Figure 4.9. As explained in Sec. 4.1.4, to first order the LVM shift is proportional to the lattice thermal energy $U(T)$,

$$\delta(\hbar\omega) = \frac{\beta}{N_A} U(T) \tag{4.11}$$

where $U(T)$ is given in units of energy per mole, N_A is Avagadro's number, and β is a dimensionless constant. We obtained the values of $U(T)$ by numerically integrating the experimental values of the specific heat $C_V(T)$ reported by Irwin and LaCombe (1974), neglecting the zero temperature energy. The data can be approximated by a linear least-squares fit to Eq. 4.11, with $\beta = -0.17$. The temperature dependent shift and the fit are shown in Figure 4.11. At 77 K, the shift of the ZnSe:As,H mode is approximately twice that of the GaAs:Zn,H mode.

As discussed in Sec. 4.1.4, elastic phonon scattering leads to a temperature dependent linewidth

$$\delta\Gamma = \Gamma(T) - \Gamma(0) = A\left(\frac{T}{\theta_C}\right)^7 \int_0^{\theta_C/T} \frac{z^6 e^z}{\left(e^z - 1\right)^2} dz \tag{4.12}$$

where $k\theta_C/\hbar$ is the effective cutoff frequency and A is an empirical constant. For high temperatures, Eq. 4.12 reduces to

$$\delta\Gamma = \alpha T^2 \tag{4.13}$$

Elliot *et al.* point out that Eq. 4.13 is a good approximation even when T is a fraction of

θ_C. Using Eq. 4.13, we obtain a fit to the data with $\alpha = 4 \times 10^{-3}$ cm^{-1}/K^2. The temperature dependent linewidth and the fit are plotted in Figure 4.12.

The ZnSe:As,H mode has a slightly higher frequency, higher *r*-factor, and stronger temperature dependence than the GaAs:Zn,H mode. These observations suggest that the coupling between the zinc and the hydrogen is slightly weaker in GaAs than in ZnSe. The effect of the zinc can be modeled as a repulsive potential which confines the hydrogen atom. The potential increases the frequency and the *r*-factor, the latter because hydrogen has a larger amplitude than deuterium and overlaps the potential more. The temperature dependent shift of the frequency and linewidth are caused primarily by coupling between the hydrogen and the thermal motion of the zinc atom. Greater coupling leads to an LVM with a more pronounced temperature dependence. Although the cause of this greater coupling is not currently understood, it may be related to the fact that ZnSe is more ionic than GaAs.

4.2.4 Conclusions

In conclusion, we have discovered LVM peaks which we attribute to bond-stretching modes of As-H and As-D complexes in MOCVD-grown ZnSe. By analogy with the Zn-H complex in GaAs, we propose that the hydrogen binds directly to the arsenic acceptor in a bond-centered orientation, adjacent to a host zinc atom. Samples which were grown with deuterium as a carrier gas have a strong As-H peak and a weak As-D peak, indicating that the hydrogen originates primarily from by-products of reactions involving the metalorganic molecules and the carrier gas. Furthermore, it is clear that in p-type doping of MOCVD-grown ZnSe, hydrogen passivation plays a significant role.

Table 4.4. Peak positions, widths, and isotopic frequency ratios of As-H and As-D LVMs in GaAs:Zn and ZnSe:As.

	As-H stretch mode		As-D stretch mode		
Compound	Peak (cm^{-1})	FWHM (cm^{-1})	Peak (cm^{-1})	FWHM (cm^{-1})	$r = \nu_H / \nu_D$
GaAs:Zn[a]	2146.9	1.8	1549.1	0.9	1.3860
ZnSe:As	2165.6	2.8	1557.1	1.9	1.3908

[a] See Chevallier *et al.* (1991)

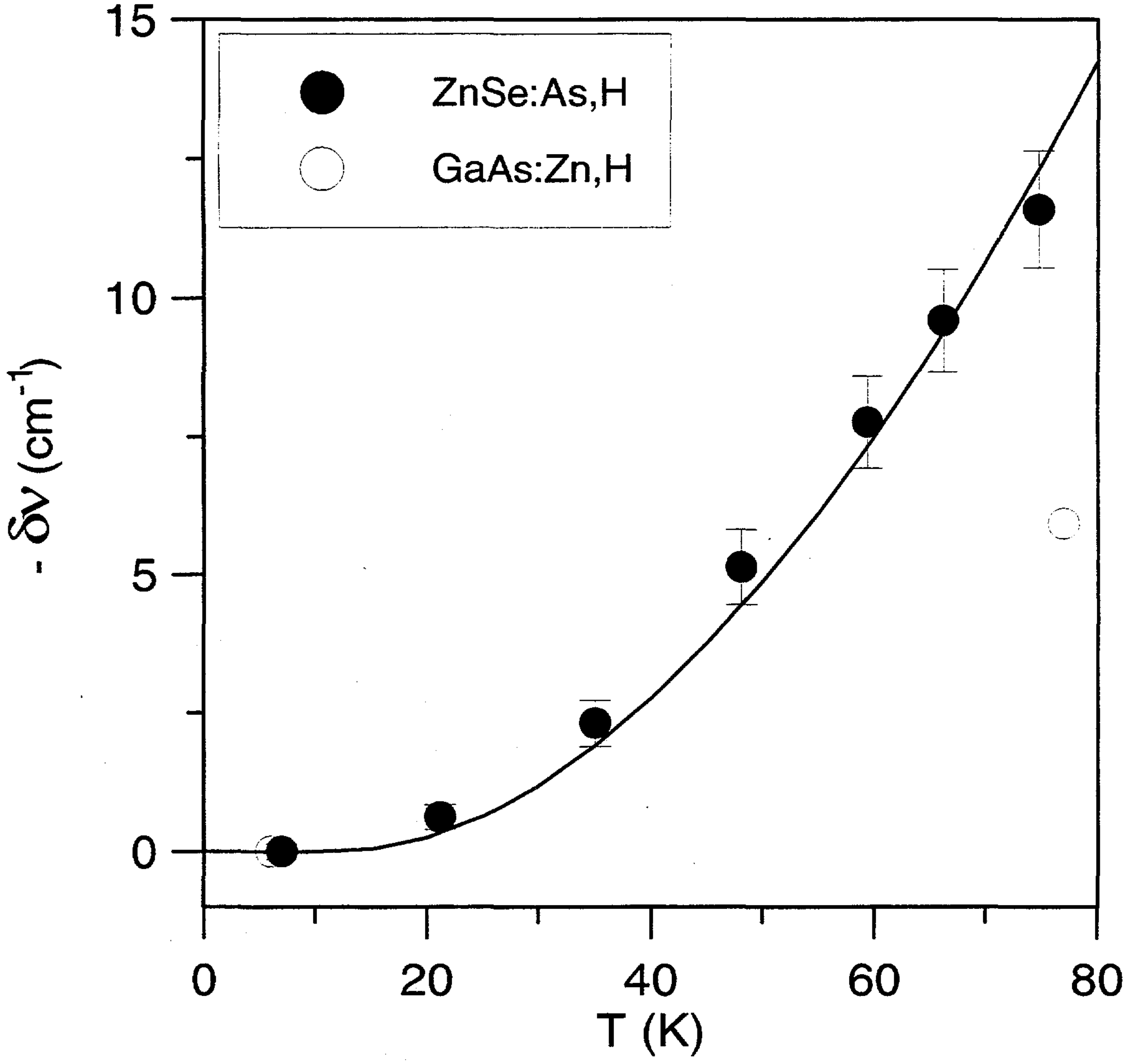

Figure 4.11. Shift of the As-H LVM frequency with temperature for ZnSe (this work) and GaAs (Chevallier *et al.*, 1991). The solid line is a fit according to Eq. 4.11, with $\beta = -0.17$.

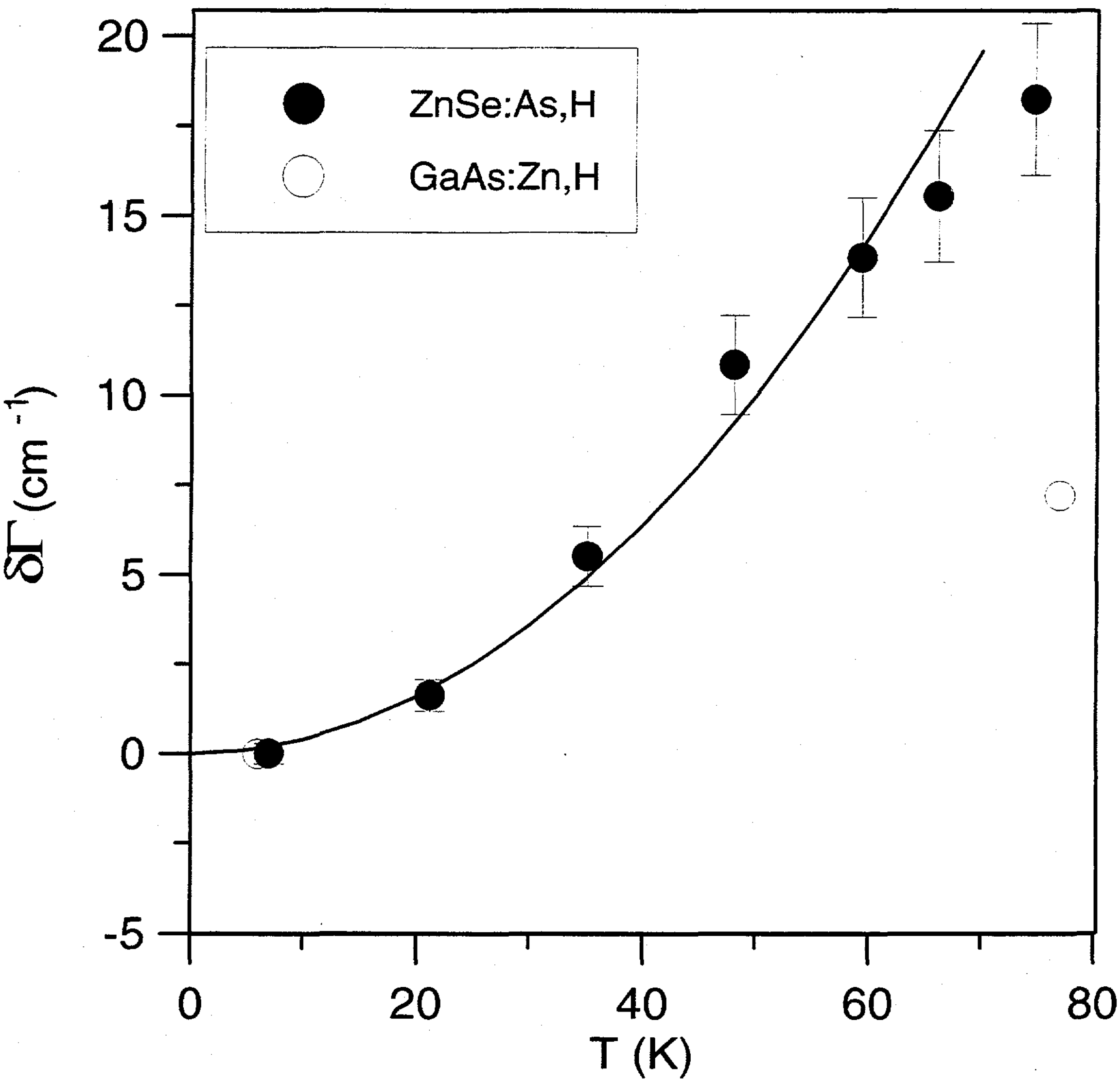

Figure 4.12. Shift of the As-H LVM linewidth with temperature for ZnSe (this work) and GaAs (Chevallier *et al.*, 1991). The solid line is a fit according to Eq. 4.13. with $\alpha = 4 \times 10^{-3}$ cm^{-1}/K^2.

4.3 Hydrogen Passivation of DX Centers in AlSb

In this chapter, I describe LVMs of DX-hydrogen complexes in AlSb (McCluskey *et al.*, 1996b). A DX center is a donor that has a deep ground state in an off-substitutional configuration. As shown in Figure 4.13, the coordinates of the defect are represented by the configuration coordinate Q. A donor can be transferred from the deep DX state (binding energy E_{DX}) into the substitutional hydrogenic state (binding energy E_D) by absorbing a photon of energy greater than E_{OPT}. If the temperature is low enough, typically 120 K or below, the hydrogenic state is metastable. As discussed in Sec. 4.3.3, in AlSb:Se, the persistent photoionization of the hydrogenic state is measured to obtain the relative concentration of DX centers. The first DX centers were observed in $Al_xGa_{1-x}As$ for $x > 0.22$ (Nelson 1977; Lang and Logan, 1977) and GaAs under pressure (Mizuta *et al.*, 1985; Wolk *et al.*, 1991).

In most semiconductors, the DX state is the ground state only when the semiconductor is an alloy or when hydrostatic pressure is applied. In AlSb, however, the ground states of Se (Becla *et al.*, 1995) and Te (Jost *et al.*, 1994) donors are DX states, making them convenient for spectroscopic studies. This is the first infrared spectroscopic study of DX-hydrogen complexes.

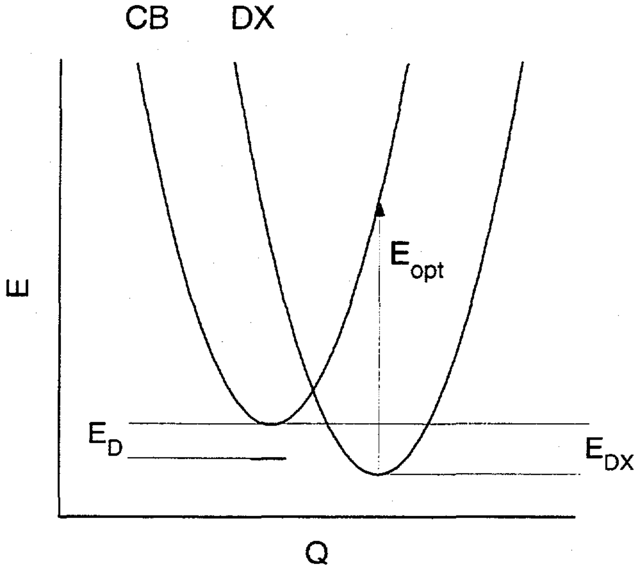

Figure 4.13. Configuration diagram of a DX center.

4.3.1 Introduction

As mentioned in Sec. 1.5, hydrogen can be introduced into a sample by boiling in water, electrolysis, implantation, exposure to a hydrogen plasma, or contamination during the growth process (Haller 1994). In this section, I show that annealing bulk AlSb:Se or AlSb:Te in a hydrogen atmosphere at temperatures as low as 700°C followed by a rapid quench leads to the formation of DX-hydrogen complexes. We have also found that hydrogen passivation can occur by annealing in methanol (CH_3OH) vapor. It has been demonstrated that annealing in hydrogen passivates shallow acceptors (Veloarisoa *et al.*, 1991) and platinum (Williams *et al.*, 1993) in silicon. Annealing of heavily doped epitaxial GaAs:C layers in a hydrogen ambient was shown to passivate the carbon acceptor (Kozuch *et al.*, 1993). This is the first study in which n-type semiconductors have been passivated by annealing in hydrogen.

The AlSb crystals were grown by the Czochralski technique from selenium or tellurium doped melts. The growth was performed in a Sb-enriched melt, with an atomic fraction [Sb]/([Sb]+[Al])=0.515. Some of the samples were sealed in evacuated quartz ampoules with a 1/3 atm H_2 or D_2 ambient and annealed for 1 hr at temperatures ranging from 700°C to 950°C. After completion of the diffusion, the samples were quenched to room temperature by dropping the ampoules into ethylene glycol. Some AlSb samples were sealed in quartz ampoules with 0.3 ml CH_3OH or methanol-d_4 (CD_3OD) and annealed for 1 hr at 900°C, followed by a rapid quench. Since an unknown fraction of the methanol evaporated before the ampoules were completely sealed, it was not possible to determine the methanol vapor pressure. To remove the surface damage from annealing in hydrogen, approximately 50 μm of the surfaces were lapped with a slurry of 3 μm SiC grit and water, followed by polishing with a slurry of 0.3 μm Al_2O_3 powder and methanol. After polishing, the samples were approximately 2 mm thick. Since AlSb is hygroscopic, samples were kept with desiccant in sealed containers.

Infrared absorption spectra above 500 cm^{-1} were obtained with a Bomem DA8 spectrometer with a KBr beamsplitter and an external mercury cadmium telluride (MCT) detector. For spectra below 500 cm^{-1} we used a 3 μm Mylar beamsplitter and a deuterated tryglycine sulfate (DTGS) detector. The samples were placed in a Janis continuous-flow liquid helium cryostat with ZnSe windows for spectra above 500 cm^{-1}

and polypropylene windows for spectra below 500 cm^{-1}. We used instrumental resolutions ranging from 0.1 to 1 cm^{-1} such that all the LVM peaks were fully resolved.

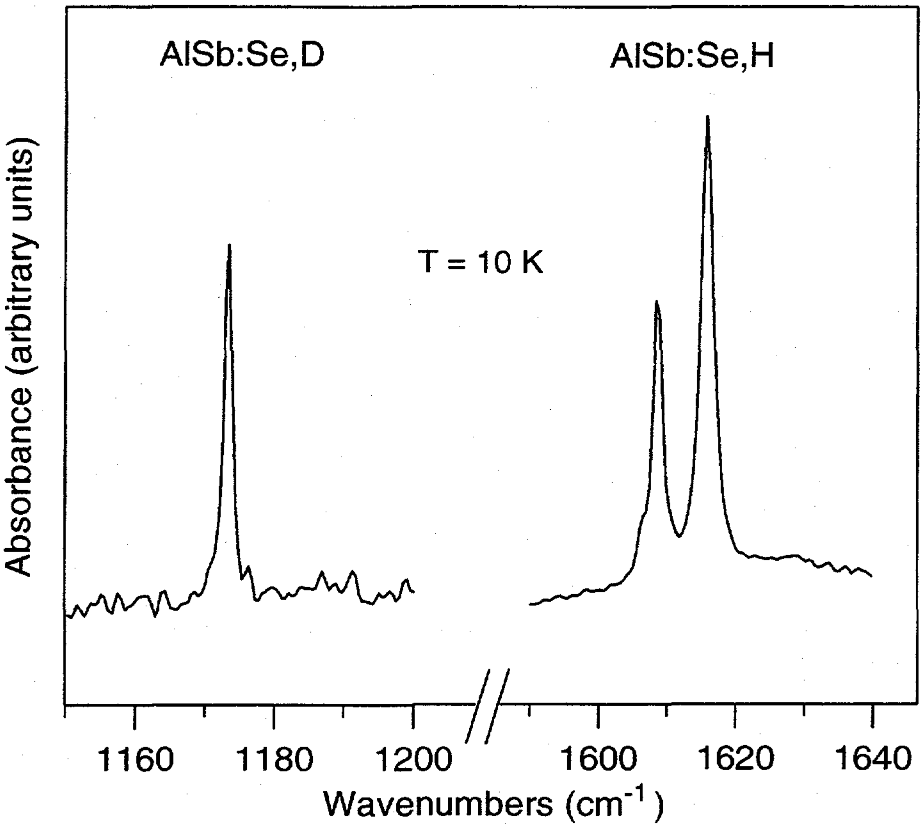

Figure 4.14. Infrared absorption peaks of deuterated and hydrogenated AlSb:Se at a temperature of 10 K. The peaks are attributed to bond-stretching modes. with the deuterium/hydrogen attached to an aluminum atom.

4.3.2 LVMs in AlSb:Se,H

AlSb:Se samples that were annealed in H_2 or CH_3OH at 900°C for 1 hr have infrared absorption peaks at 1608.6 and 1615.7 at a temperature of 10 K (Figure 4.14). Some of the as-grown samples also show these peaks with much smaller absorption strengths, indicating the presence of hydrogen in the growth process. Longer H_2-annealing times do not increase the size of the peaks, so a 1 hr H_2-anneal is probably sufficient to diffuse the hydrogen through the entire bulk. We attribute the peaks at 1608.6 and 1615.7 cm^{-1} to hydrogen stretch modes. Since the bond-stretching mode of the free diatomic molecule AlH is 1624 cm^{-1} (Rosen 1970), while the hydrogen stretch modes of H_2Se and SbH_3 are 2345 and 1891 cm^{-1}, respectively (Shimanouchi 1972), we propose that the hydrogen binds to an aluminum atom.

AlSb:Se samples that were annealed in D_2 or CD_3OD at 900°C for 1 hr have only one stretch mode at 1173.4 cm^{-1} at a temperature of 10 K. AlSb:Se samples that were annealed in a mixture of H_2 and D_2 have the hydrogen- and deuterium-related peaks but no new peaks which would have indicated a multihydrogen complex. The isotopic ratios, $r = \nu_H/\nu_D$, are close to $\sqrt{2}$, indicating that the vibrational modes are dominated by the motion of the hydrogen and not the aluminum (Sec. 2.3.3). For the stretch modes, since there are two hydrogen peaks, there are two r values, $r = 1.3709$ and 1.3769. The peak positions, widths, areas, and r values of the LVMs are given in Table 4.5.

The fundamental transitions of the Se-D and Se-H wag modes are not observed, since the spectral regions where we expect to find them have significant phonon absorption features. The second, third, and fourth harmonics of the Se-D and Se-H wag modes have been observed (Figure 4.15). The splittings of the peaks are a result of the threefold symmetry of the complex, as explained below. The energy level spacings are approximately 240 and 330 cm^{-1} for the Se-D and Se-H wag modes, respectively. It should be noted that the fine structure and broadening of the Se-H third harmonic are currently not understood. In addition, there are small peaks at 486 and 673 cm^{-1} which may correspond to unidentified deuterium- and hydrogen-related complexes.

The splittings of the wag harmonics are consistent with a complex which possesses C_{3v} symmetry. In the plane perpendicular to the [111] axis, the C_{3v} potential is given by (Newman 1969; Sciacca *et al.*, 1995)

$$V(x,y)=\frac{1}{2}k\left(x^2+y^2\right)+B\left(xy^2-x^3/3\right)+C\left(x^2+y^2\right)^2+\cdots \quad , \tag{4.14}$$

where x and y are parallel to the $[1\bar{1}0]$ and $[11\bar{2}]$ crystallographic axes, respectively. For simplicity, we have omitted the wag-stretch coupling terms. The anharmonic terms in Eq. 4.14 lift the threefold degeneracy of the wavefunctions for $N = n_x + n_y > 1$. The predicted splittings are shown in Figure 4.16. The dipole allowed transitions are the $\Gamma_1 \rightarrow \Gamma_1$ and $\Gamma_1 \rightarrow \Gamma_3$ transitions. The higher harmonics give rise to weaker peaks, since they require higher order anharmonic terms in Eq. 4.14.

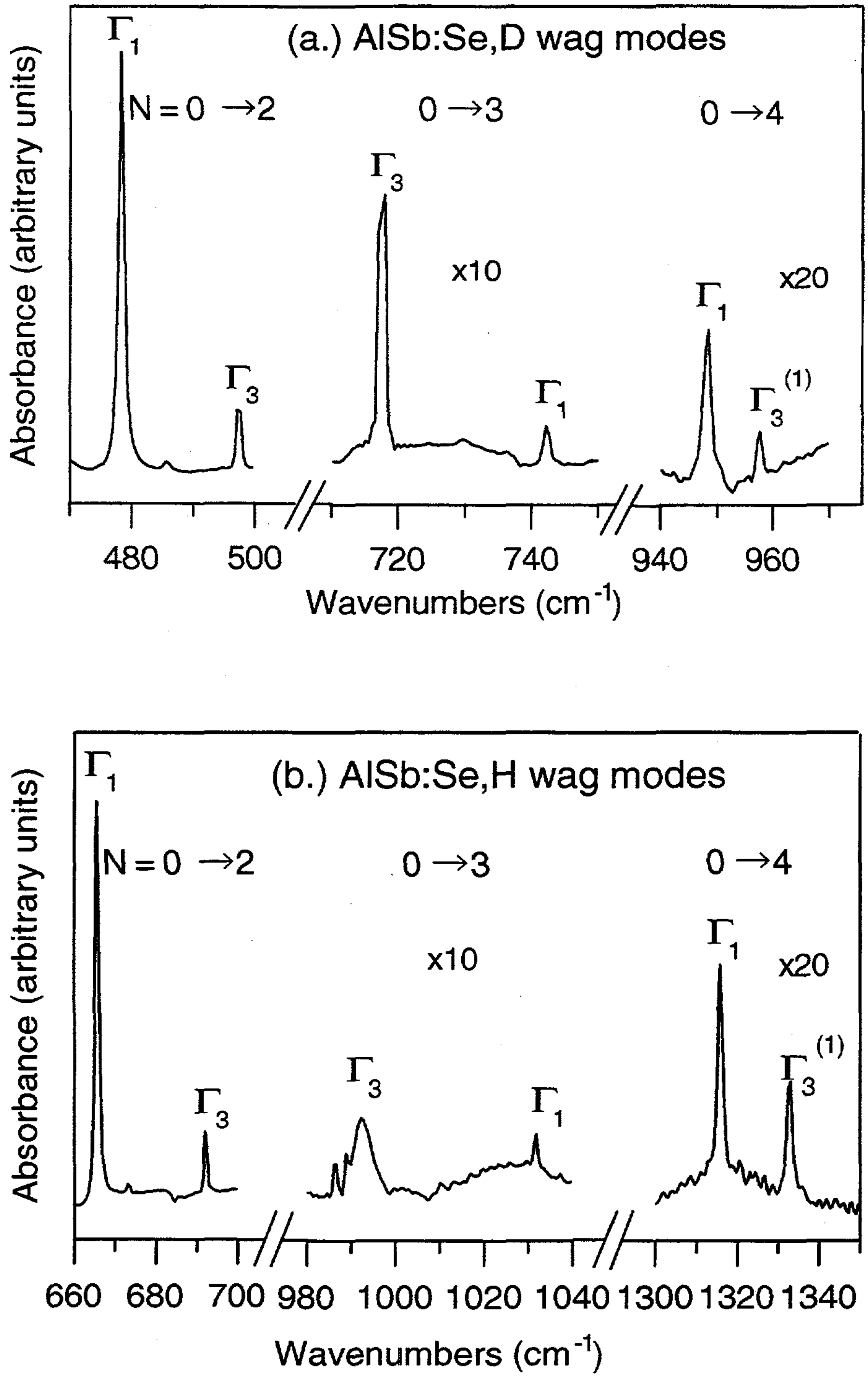

Figure 4.15. Infrared absorption peaks of deuterated and hydrogenated AlSb:Se. The peaks are attributed to the second, third, and fourth harmonics of the hydrogen/deuterium wag modes. The peak assignments are discussed in Appendix B.

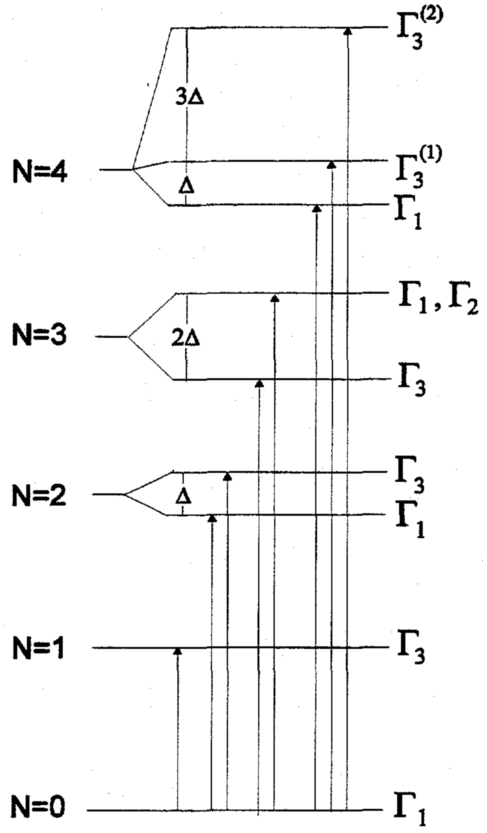

Figure 4.16. The splitting of the hydrogen/deuterium wag modes in C_{3v} symmetry. Splittings are expanded for clarity. The dipole allowed transitions are the $\Gamma_1 \to \Gamma_1$ and $\Gamma_1 \to \Gamma_3$ transitions. The Γ_1 and Γ_2 states are accidentally degenerate. The theoretical level spacing Δ is defined in Appendix B.

4.3.3 Electronic spectrum of passivated AlSb:Se

In addition to LVMs, we observed the effect of hydrogenation on the Se electronic spectrum. At temperatures below 90 K, AlSb:Se exhibits a large photoinduced persistent optical absorption (Becla *et al.*, 1995). When AlSb:Se samples are exposed to light of energy 1 eV or more, the Se donors are transformed from a deep DX-like state to a metastable hydrogenic state. The hydrogenic absorption spectrum extends from 0.1 to

1.5 eV and is due to the excitation of the electron from the ground state to the X_1 and X_3 conduction bands. The hydrogenic spectrum was first measured by Ahlburn and Ramdas (1968), long before the existence of DX centers was established.

We measured the persistent optical absorption of AlSb:Se samples that were annealed in a D_2 atmosphere at several temperatures ranging from 700°C to 950°C. The absorption spectra at 10 K after 2 min exposures to a white filament light bulb were measured and referenced to the spectra prior to exposure. Although only a fraction of the Se_{DX} centers are transferred into their hydrogenic states, the strength of the photoinduced absorption gives a relative measure of the Se_{DX} concentration. As shown in Figure 4.17, the persistent absorption decreases with increasing annealing temperature, while the height of the Se-D stretch mode increases. The correlation between the LVM increase and the persistent absorption decrease indicates that the deuterium passivates a significant fraction of the Se DX centers.

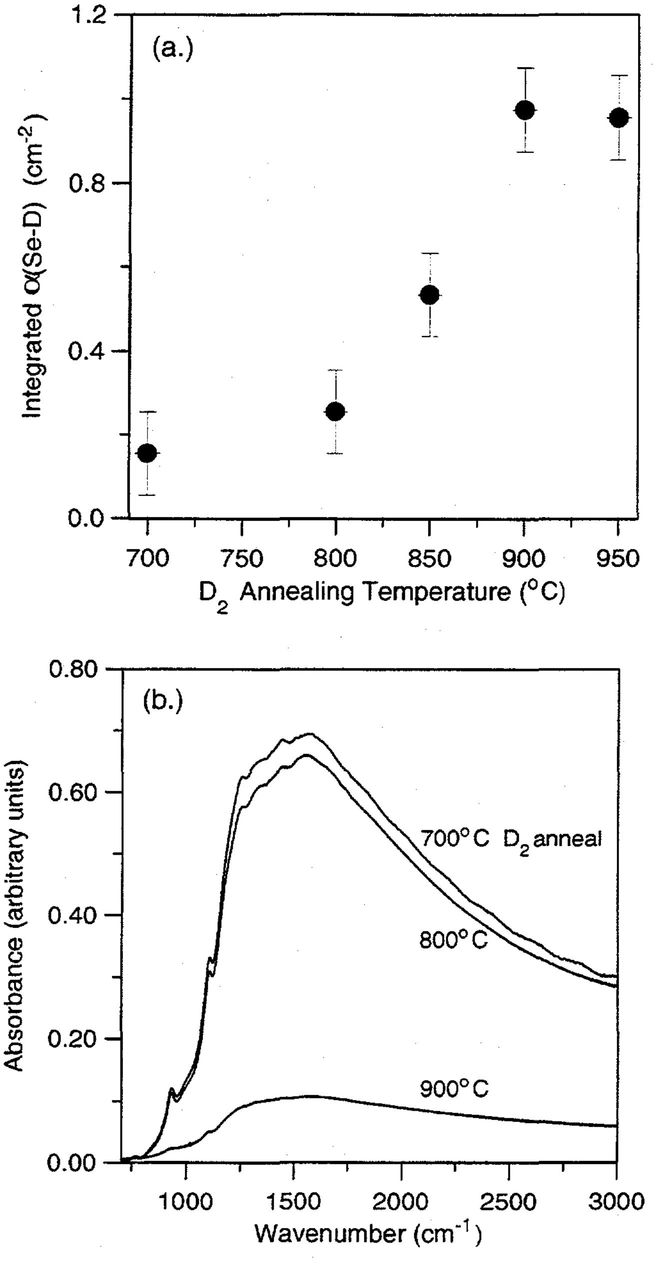

Figure 4.17. (a.) Integrated absorption of the Se-D peak in AlSb:Se as a function of D_2-annealing temperature. Samples were annealed in 1/3 atm D_2 for 1 hr. (b.) Persistent photoabsorption in AlSb:Se for annealing temperatures of 700°C, 800°C, and 900°C. The correlation between the increasing Se-D peak area and decreasing photoabsorption indicates that a significant fraction of Se DX centers are passivated.

4.3.4 LVMs in AlSb:Te,H

AlSb:Te samples that were annealed in H_2 or D_2 atmospheres at 900°C for 1 hr have stretch modes at 1599.0 and 1164.4 cm^{-1}, and second harmonic wag modes at 665.0 and 478.2 cm^{-1}, respectively (Figure 4.18). Like Se, Te also exhibits a DX-like bistability in AlSb (Jost *et al.*, 1994). In the samples that we studied, the Te-H peaks were 4 to 8 times weaker than the Se-H peaks, perhaps because hydrogen does not passivate Te as efficiently as Se. The fact that the hydrogen stretch and wag modes of AlSb:Se and AlSb:Te have similar vibrational frequencies and *r*-values provides evidence that the hydrogen attaches to an aluminum atom in an antibonding, rather than a bonding, orientation (Figure 4.19). As described in Sec. 1.3.3, the antibonding model also applies to donor-hydrogen complexes in Si. This finding is consistent with the study of Rahbi *et al.* (1994) and Vetterhöffer *et al.* (1994), who measured the hydrogen modes in GaAs:Se and GaAs:Te to be 1507.5 and 1499.9 cm^{-1}, respectively. Those LVMs were attributed to hydrogen stretch modes, with the hydrogen attached to a gallium atom in an antibonding orientation. Since the hydrogen is weakly coupled to the donor, the LVM frequency does not depend strongly on the donor species.

Theoretical studies (Chang *et al.*, 1992) of the DX-hydrogen complex of GaAs:S under hydrostatic pressure suggest that two neutral hydrogen atoms can passivate a positively ionized donor and a negatively ionized DX center, resulting in two neutral complexes. The structures of the DX-hydrogen and donor-hydrogen complexes are identical, with the hydrogen in an antibonding [111] orientation. Our results for DX-hydrogen complexes in AlSb lend further support to the antibonding model.

4.3.5 Conclusions

In conclusion, we have discovered that annealing AlSb:Se and AlSb:Te in hydrogen gas or methanol vapor results in the passivation of the Se and Te donors. The hydrogen stretch and wag mode harmonics are consistent with complexes which possess C_{3v} symmetry, with the hydrogen attached to an aluminum atom in a [111] antibonding orientation. The antibonding model is similar to that of group VI donor-hydrogen complexes in GaAs. The anomalous splitting of the Se-H stretch mode is discussed in the following section.

Table 4.5. Peak positions, widths, areas, and isotopic ratios of hydrogen and deuterium related LVMs in AlSb:Se and AlSb:Te at liquid-helium temperature. The areas of the stretch modes are normalized to unity.

H-mode	**ν (cm^{-1})**	**FWHM (cm^{-1})**	**Area**	**D-mode**	**ν (cm^{-1})**	**FWHM (cm^{-1})**	**Area**	$r=\nu_H/\nu_D$
Se-H				**Se-D**				
Stretch #1	1608.6	1.5	1	Stretch	1173.4	1.4	1	1.3709
#2	1615.7	2.2	2.4					1.3769
Wag				Wag				
2nd harmonics	665.7	1.2	8.0	2nd harmonics	478.3	1.5	3.7	1.3921
	692.2	0.5	0.91		497.4	0.5	0.44	1.3916
3rd harmonics	992.6	4.7	0.83	3rd harmonics	717.5	0.4	0.2	1.3834
	1031.8	0.9	0.048		742.2	1.0	0.033	1.3902
4th harmonics	1315.8	1.5	0.25	4th harmonics	948.4	1.2	0.046	1.3874
	1333.0	1.5	0.16		957.4	1.3	0.014	1.3923
Te-H				**Te-D**				
Stretch	1599.0	1.3		Stretch	1164.4	1.0		1.3732
Wag (2nd harmonic)	665.0	1.0		Wag (2nd harmonic)	478.2	1.3		1.3906

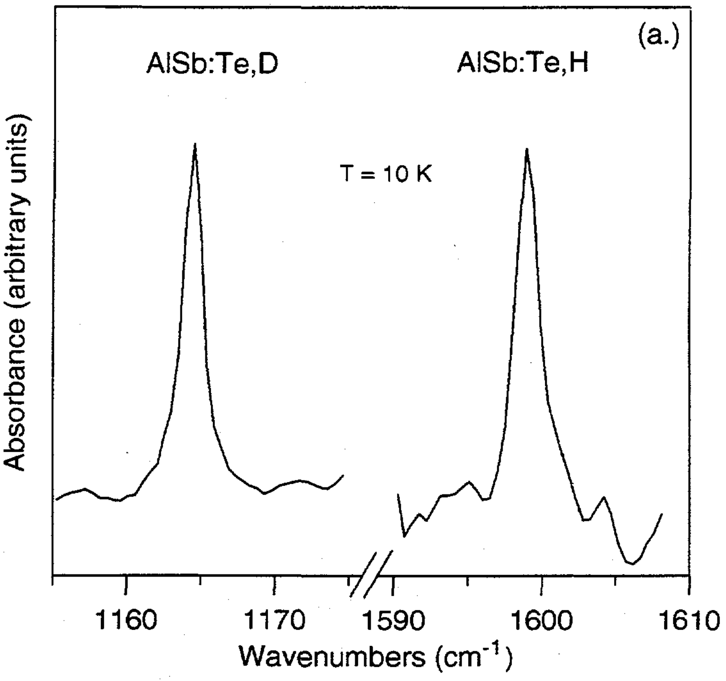

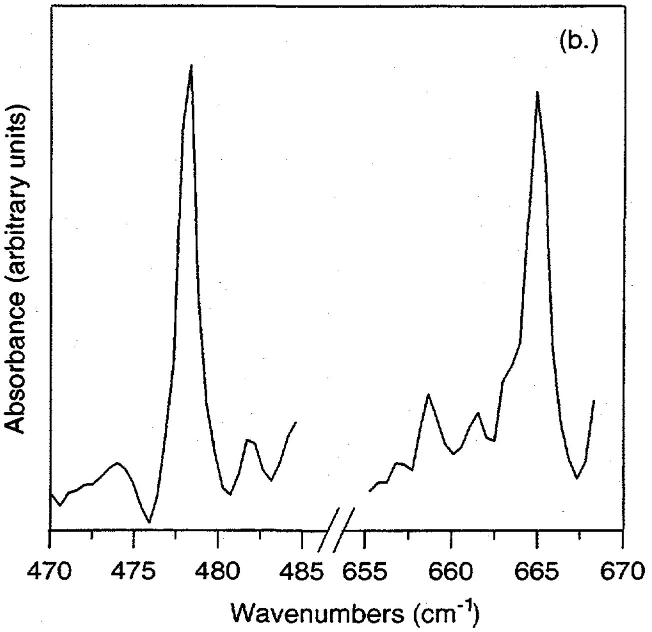

Figure 4.18. Infrared absorption peaks of deuterated and hydrogenated AlSb:Te. (a.) Bond-stretching modes. (b.) Second harmonic wag modes. The LVM frequencies are similar to the Se-D and Se-H modes, providing evidence for the antibonding model.

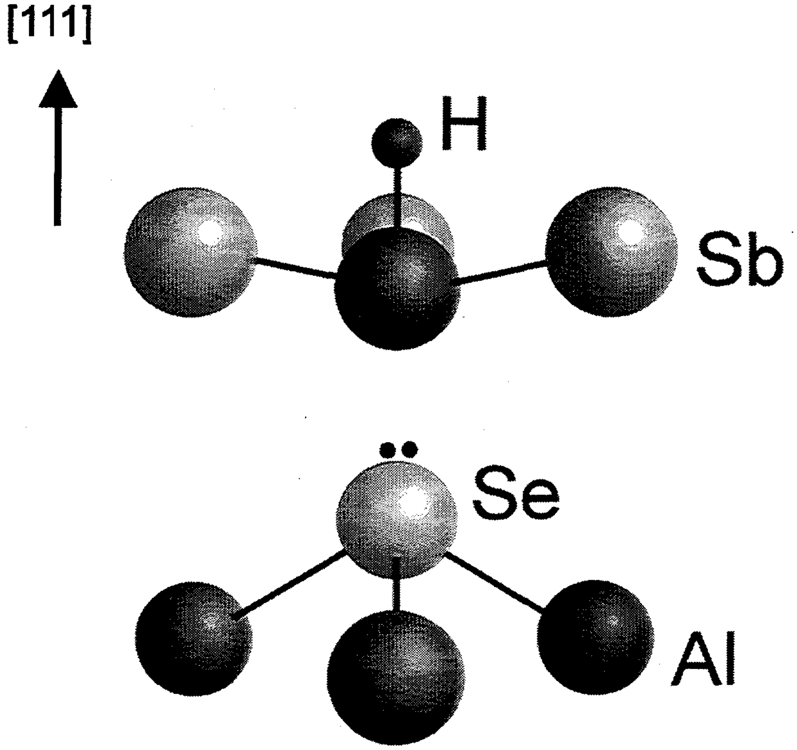

Figure 4.19. Model for the structure of the DX-hydrogen complexes in AlSb. The hydrogen attaches to an aluminum atom in a [111] antibonding orientation.

5. Resonant LVM-Phonon Interactions: the Localon

Resonant interactions between weakly coupled systems play an important role in a variety of phenomena in solid state physics. The study of such interactions has led to discoveries of new quasi-particles such as polarons (Frölich *et al.*, 1950) and polaritons (Kittel, 1986). Thus far most of these studies have been limited to interactions between electronic and vibronic subsystems of the lattice, since small changes in electronic properties can be easily detected and the energy levels may be tuned by external perturbations such as magnetic field or pressure. Recently, Zheng and Stavola (1996) have discovered a Fermi resonance between wag and stretch local vibrational modes (LVMs) in donor-hydrogen complexes in silicon. In this chapter, I discuss the first evidence of a resonant interaction between LVMs and extended lattice phonons that gives rise to a new collective excitation called a "localon" (McCluskey *et al.*, 1997). By varying the temperature and pressure to change the phonon energies, we have studied the evolution of the localon spectra in AlSb and GaAs.

5.1 AlSb:Se,H

As described in Sec. 4.3.2, at liquid-helium temperatures, hydrogenated AlSb:Se has stretch mode peaks at 1608.6 and 1615.7 cm^{-1}, whereas the Se-D, Te-H, and Te-D stretch modes have only one stretch vibration peak each. In addition, there is a small Se-H peak at 1606.3 cm^{-1}. The ratio of the three Se-H peak areas is constant from sample to sample, which suggests that they are not due to additional impurity complexes. In the following discussion, we provide evidence that the Se-H stretch mode interacts with two multi-phonon modes, giving rise to several absorption peaks. The Se-D stretch mode, which is far away from these modes, does not split. The LVM-phonon interaction gives rise to a new quasiparticle that we refer to as the *localon*.

5.1.1 Temperature Dependence

The temperature dependence of the Se-H and Se-D stretch modes is shown in Figure 5.1. The linewidth broadening and shift to lower frequency with increasing temperature is seen in numerous semiconductor systems and is caused by an anharmonic interaction between the localized mode and acoustic phonons (Sec. 4.1.4). Although the broadening obscures peak 0, peaks 1 and 2 are clearly resolved up to a temperature of 100 K. As the temperature increases, the area of peak 1 increases while the area of peak 2 decreases. The peak areas were determined by a two-Lorentzian peak fit. The sum of the areas remains constant to within the experimental error.

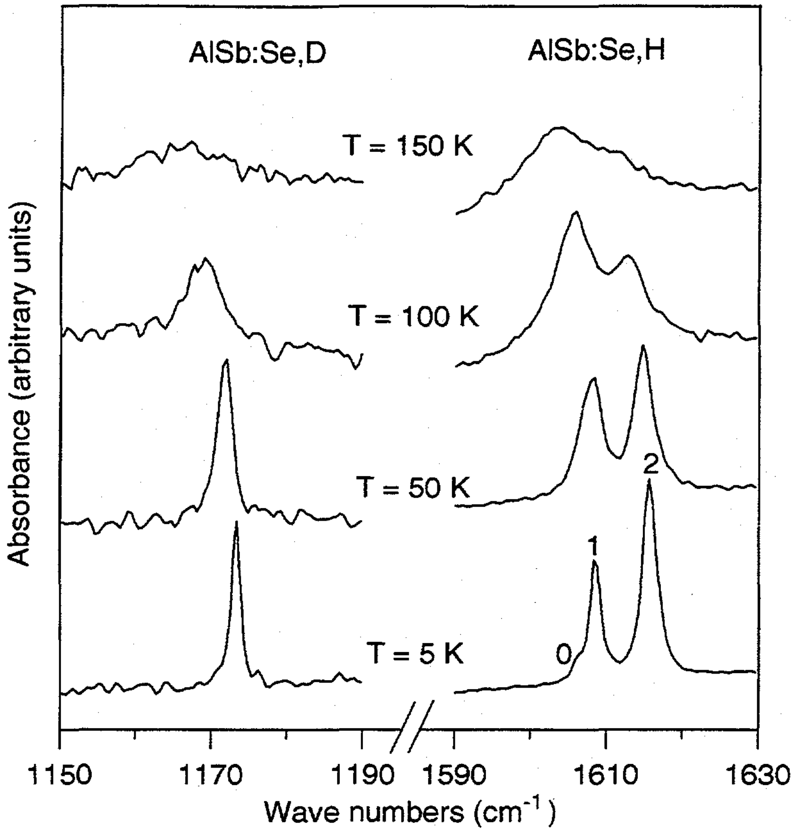

Figure 5.1. Temperature dependence of Se-D and Se-H stretch modes in AlSb.

To explain these observations, we propose a model in which the Se-H stretch mode and a multi-phonon mode are nearly degenerate and interact with an energy *A*. The Hamiltonian is given by:

$$H = \begin{bmatrix} \omega_{LVM} & A \\ A & \omega_{phonon} \end{bmatrix} \tag{5.1}$$

The eigenvalues of this Hamiltonian are

$$\omega_{\pm} = \tfrac{1}{2}\left[\omega_{LVM} + \omega_{phonon} \pm \sqrt{\left(\omega_{LVM} - \omega_{phonon}\right)^2 + 4A^2}\right] \tag{5.2}$$

In our model, $A = 3.45\ \mathrm{cm}^{-1}$. The minimum frequency difference between the two peaks is $2A = 6.9\ \mathrm{cm}^{-1}$. The eigenfunctions of the Hamiltonian (5.1) are linear combinations of an LVM and a multi-phonon,

$$|\psi\rangle = a|LVM\rangle + b|phonon\rangle \tag{5.3}$$

We refer to this linear combination of a local mode and a phonon as a *localon*. Since the multi-phonon mode is practically infrared inactive, the coefficient *a* can be determined experimentally from the normalized area of each peak. For peak 1, the lower frequency peak,

$$|a|^2 = A_1/(A_1+A_2), \tag{5.4}$$

where A_1 and A_2 are the integrated areas of peaks 1 and 2, respectively. The theoretical expression is given by:

$$|a|^2 = \frac{A^2}{(\omega_{LVM} - \omega_-)^2 + A^2} \tag{5.5}$$

The temperature dependence of the unperturbed stretch mode is given by

$$\omega_{LVM} = 1613.0 - 0.034\ U(T), \tag{5.6}$$

where $U(T)$ is the mean vibrational energy of the lattice (Sec. 4.1.4) in cal/mole and ω_{LVM} is given in cm^{-1}. The multi-phonon mode can be described by the empirical relation

$$\omega_{phonon} = 1611.4 - 30/(\exp(380/T)+1), \tag{5.7}$$

The parameters are adjusted to fit the data.

As the temperature increases, the area of peak 1 increases as it becomes more "LVM-like" (Figure 5.2). Conversely, the area of peak 2 decreases as it becomes more "phonon-like."

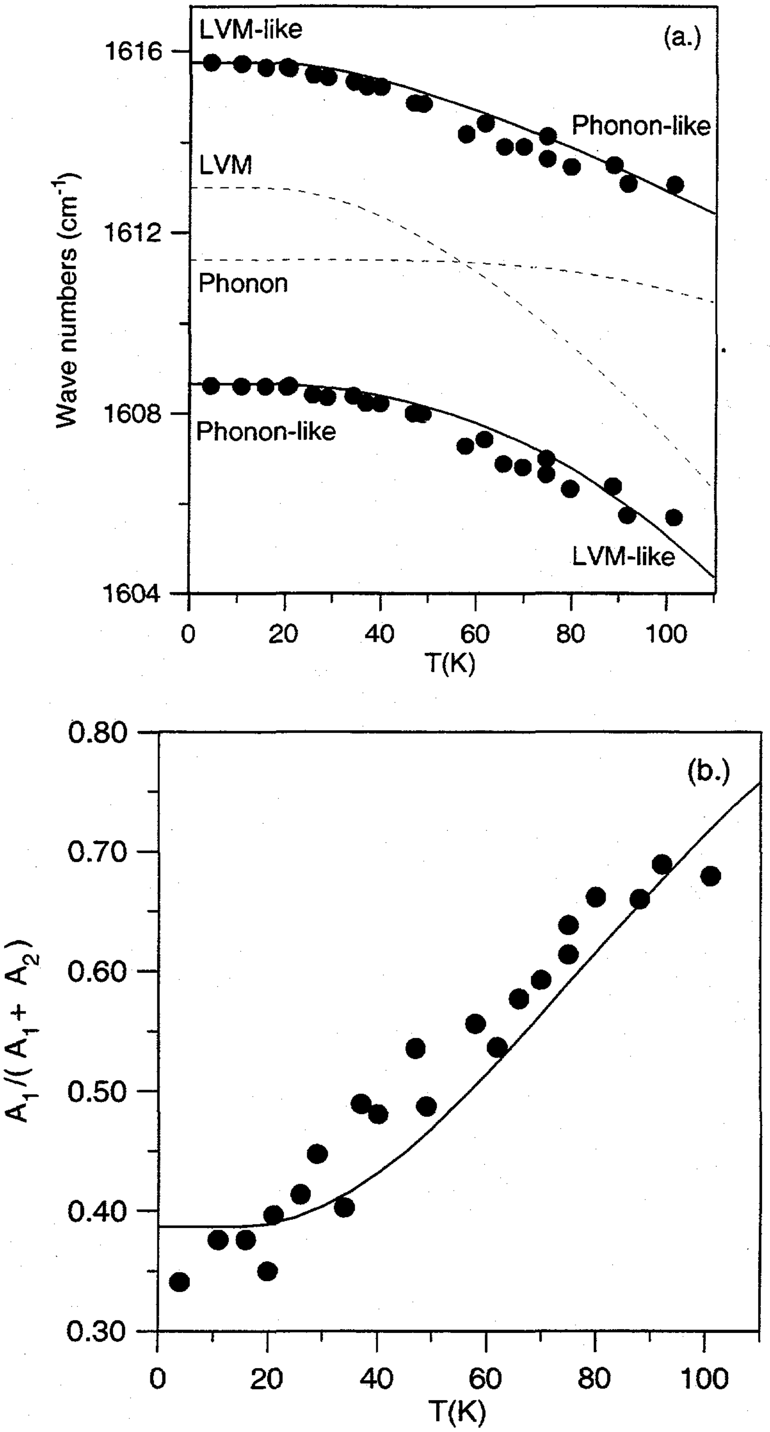

Figure 5.2. (a.) Se-H stretch modes as a function of temperature. The dashed lines are the unperturbed LVM and multi-phonon modes (Eq. 5.6-5.7) and the solid lines are the perturbed modes (Eq. 5.2). (b.) Normalized area of Se-H peak 1 (lower-frequency peak). The solid line is a plot of the theoretical model (Eq. 5.5).

5.1.2 Pressure Dependence

Variable pressure spectra were obtained with a Digilab 80-E spectrometer with a KBr beamsplitter and an instrumental resolution of 0.5 cm-1. To generate hydrostatic pressures up to 15 kbar, we used a modified Merrill-Basset diamond-anvil cell (Sec. 3.3). The liquid immersion-technique was used to load the cell with liquid nitrogen. A light-concentrating cone focused the light through the diamonds and sample and into a Ge:Cu photoconductor mounted directly behind the sample. We use the pressure dependence of the AlSb:C_{Sb} LVM as a precise in situ calibration of the sample pressure (Sec. 3.4).

Anti-crossing is observed between the three peaks when the hydrostatic pressure is increased. Varying the pressure has the advantage of not broadening the lines, so that both multi-phonon modes are resolved. As shown in Figure 5.3, at pressures around 2 kbar, there are three absorption peaks. In our three-level system, the Hamiltonian is given by

$$H = \begin{bmatrix} \omega_{LVM} & A & B \\ A & \omega_{phonon,1} & 0 \\ B & 0 & \omega_{phonon,2} \end{bmatrix} \tag{5.8}$$

where A = 3.45 cm^{-1} and B = 1 cm^{-1}. For simplicity we have neglected the interaction between the multi-phonon modes. The pressure dependence of the modes are given by

$$\omega_{LVM} = 1612.7 + 0.075\ \mathrm{P} \tag{5.9}$$

$$\omega_{phonon,1} = 1610.5 + 2.1\ P \tag{5.10}$$

$$\omega_{phonon,2} = 1605.8 + 2.1\ P \tag{5.11}$$

where P is the pressure in kbar and the frequencies are in units of cm^{-1}. The eigenvalues of the Hamiltonian (5.8) are calculated using MATLAB. We obtain very good agreement between the model and experiment (Figure 5.4).

The pressure dependence can be understood qualitatively as follows: the LVM interacts primarily with phonon 1, producing a localon. The localon then interacts with phonon 2, with a smaller coupling energy. The anti-crossing between the three modes yields three infrared active peaks at pressures of ~2 kbar. For higher pressures, only the lowest branch, peak 0, is "LVM-like."

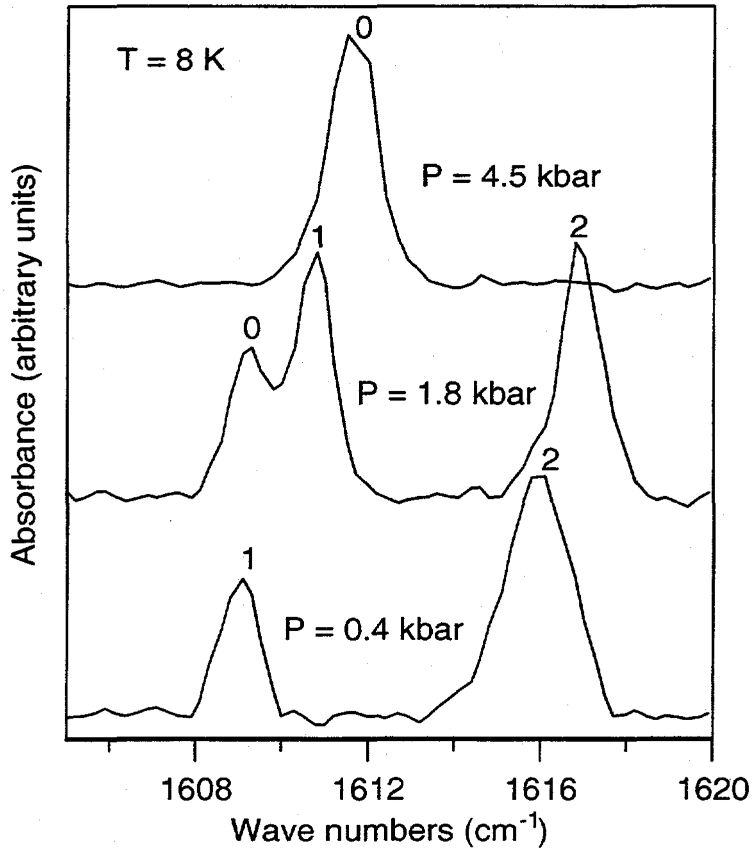

Figure 5.3. Se-H stretch mode peaks as a function of pressure.

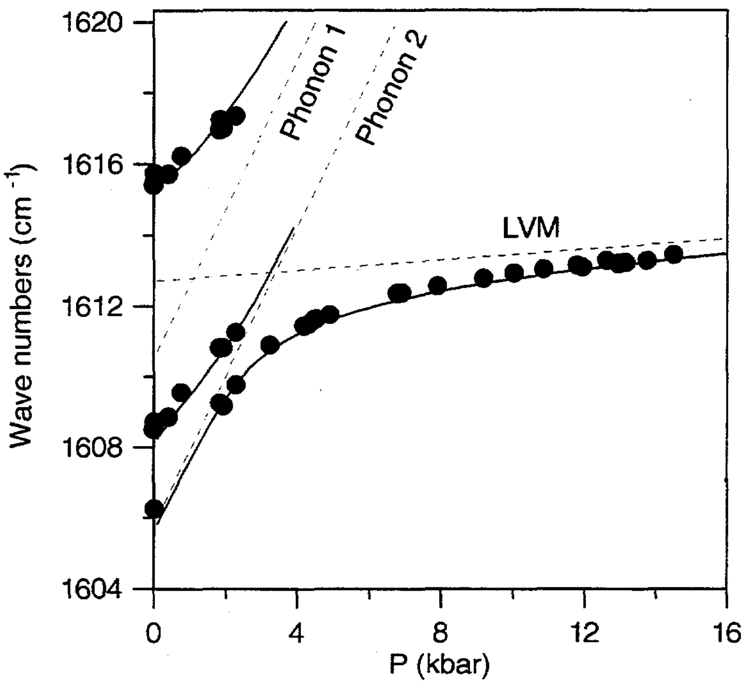

Figure 5.4. Se-H stretch mode peaks as a function of pressure. The dashed lines are the unperturbed LVM and multi-phonon modes and the solid lines are plots of the three-level theory (Eq. 5.8-5.11).

5.1.3 Summary of Results

Using variable temperature and pressure infrared spectroscopy, we have observed an anti-crossing resonance between the AlSb:Se,H stretch mode and two unknown modes. We propose that the modes are different combinations of five optical phonons, since 5 X $\omega_{TO}(\Gamma) \sim 1610$ cm^{-1} is very close to the observed frequencies. The pressure dependence of the TO phonon at room temperature is 0.58±0.5 cm^{-1}/kbar (Ves *et al.*, 1986). This value is somewhat larger than the value predicted by Eq. 5.10 and 5.11, 1/5 X 2.1 = 0.4 cm^{-1}/kbar. Another possibility is that the modes are overtones of other Se-H LVMs. Only Γ_1 modes can interact with the Γ_1 stretch mode (Appendix A). The N=5,

Γ_1 wag mode has a predicted frequency of 1665 cm^{-1}, which is too far away from the stretch mode (1610 cm^{-1}) to interact. In addition, there is only one N=5, Γ_1 wag mode, and we observe two "unknown" modes. Although there may be other modes that have not been detected, the five-phonon modes remain the best candidates.

5.2 GaAs:C

In GaAs, the C_{As} substitutional impurity gives rise to a LVM peak at 580 cm^{-1} and an unexplained sideband at 576.6 cm^{-1} at room temperature (Alt and Dischler, 1995). We extended the measurements of Alt and Dischler to temperatures as high as 500 K. As the temperature increases, the main peak merges with the sideband and broadens (Figure 5.5). We propose that the sideband is produced by an interaction between the LVM and a two-optical-phonon mode. Unlike in the case of AlSb:Se,H, the energy of interaction is less than the width of the phonon mode, so we must use a Green's function approach to correctly describe the line shape.

The Green's function of the local mode is given by

$$G^{-1}(\omega) = \omega - \omega_L + \int_{-\infty}^{\infty} f_P(\omega') \frac{C}{\omega - \omega' + i\eta} d\omega', \tag{5.12}$$

where ω_L is the local mode center frequency, $f_P(\omega)$ is the phonon density of states, $C = \langle LVM | H_{\text{int.}} | phonon \rangle$, and $\eta \to 0^+$ (Nakayama 1969). The local mode interacts with a distribution of phonon modes. Eq. 13 can be written

$$G^{-1}(\omega) = \omega - \omega_L + \Delta(\omega) + i\Gamma(\omega). \tag{5.13}$$

The spectral weight function describes the local mode line shape and is given by

$$A(\omega) = \frac{1}{\pi} \frac{\Gamma(\omega)}{\left(\omega - \omega_L - \Delta(\omega)\right)^2 + \Gamma^2(\omega)}. \tag{5.14}$$

In our model, the two-phonon density of states is given by the empirical form

$$f_P(\omega, \omega_P) = \begin{cases} a^3/2\left(\omega_P - \omega\right)^2 e^{-(\omega_P - \omega)a} & \omega < \omega_P \\ 0 & \omega > \omega_P \end{cases} \tag{5.15}$$

where $a = 0.8$ cm and ω_P is the threshold frequency in cm^{-1}. This form describes an asymmetric phonon distribution with a sharp rise at $\omega = \omega_P$. The unperturbed LVM is assumed to have a Lorentzian line shape with a center frequency ω_L and a width of 0.5 cm^{-1}. The LVM-phonon interaction energy is $C = 1.5$ cm^{-1}. The temperature dependence of the LVM and phonon frequencies are given by

$$\omega_L = 581.6 - 0.014(T - 200) \tag{5.16}$$

$$\omega_P = 578.8 - 0.008(T - 200) \tag{5.17}$$

The theoretical and experimental spectra are plotted in Figure 5.5 for several temperatures. Note than unlike the case of AlSb:Se,H, the interaction is not strong enough to produce an anti-crossing. Instead, at high temperatures the LVM merges with the phonon band, resulting in an increased linewidth.

5.3 Conclusions

In conclusion, we have observed the first resonant interactions between LVMs and phonons in AlSb and GaAs. In AlSb, the Se-H stretch mode may interact with two different combinations of five optical phonons, resulting in three distinct peaks. How a 5-phonon mode could be so sharp, however, is an open question. In GaAs, the $^{12}C_{As}$ LVM interacts with a two-phonon mode, resulting in a sideband on the low energy side. Although it is unclear which phonons in the Brillouin zone interact most strongly with LVMs, the fact that resonant interactions are observed in two very different defects and hosts suggests that this is a general phenomenon.

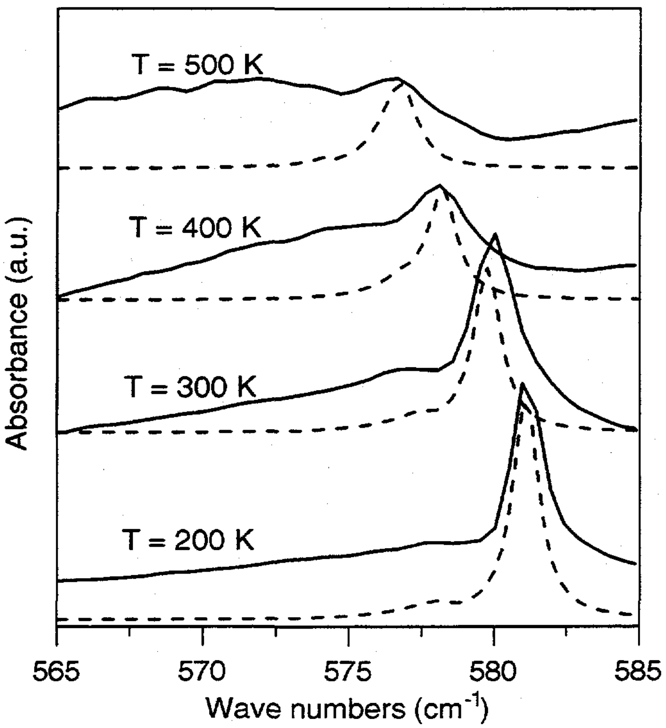

Figure 5.5. GaAs:$^{12}C_{As}$ LVM as a function of temperature. The dashed lines are plots of the theoretical model (Eq. 5.12-5.17).

6. Conclusions

I have discussed a number of hydrogen-related complexes in compound semiconductors. For group II acceptor-hydrogen complexes in GaAs, InP, and GaP, results from LVM spectroscopy show conclusively that hydrogen binds to the host anion in a bond-centered orientation, along a [111] direction, adjacent to the acceptor. As the atomic number of group II acceptors is increased from Be to Cd, the stretch mode frequency and isotopic frequency ratio $r = \nu_H/\nu_D$ increase. The increase in LVM frequency is due to the compression of the bonds. In addition, the temperature dependent shift of the LVMs are proportional to the lattice thermal energy $U(T)$, a consequence of the anharmonic coupling between the LVM and acoustical phonons.

In the wide band gap semiconductor ZnSe, epilayers grown by MOCVD and doped with As form As-H complexes. As is the case with the above mentioned systems, the hydrogen assumes a bond-centered orientation. A comparison was made between the GaAs:Zn,H and ZnSe:As,H complexes. It is clear that obtaining strongly p-type ZnSe grown by MOCVD is hindered at least in part by the formation of neutral acceptor-hydrogen complexes.

In AlSb, the Se and Te DX centers are passivated by hydrogen, which is introduced into the bulk by annealing in H_2 at a temperature of 900°C. The second, third, and fourth harmonics of Se-H and Se-D wag modes are observed and show splittings that are consistent with C_{3v} symmetry. Perturbation theory yields theoretical values of the wag modes that are in close agreement with experiment. In these complexes, the hydrogen attaches to a host aluminum atom in an antibonding orientation.

Although the Se-D complex has one stretch mode, the Se-H stretch mode splits into three peaks. The anomalous splitting is explained by a new interaction between the stretch LVM and multi-phonon modes of the lattice. The anharmonic interaction mixes the LVM and phonon states, producing a quasiparticle that we refer to as a *localon.* As the temperature is varied, we observe an anti-crossing between the LVM and phonon modes. By developing a new *in situ* pressure calibration, we also performed variable pressure spectroscopic measurements that showed a distinct anti-crossing between the LVM and the two multi-phonon modes.

7. Future Work

Since GaN and its alloys with InN and AlN are becoming important blue light-emitting materials, it is important to understand the role of hydrogen-related defects in these wide band gap semiconductors. LVM spectroscopy has been used to identify the Mg-H complex in GaN (Götz *et al.*, 1996). It is well established that in acceptor-hydrogen complexes in Si, GaAs, InP, and GaP, the hydrogen resides in a bond-centered position. In GaN:Mg, however, theoretical calculations (Neugebauer and Van de Walle, 1995) have indicated that hydrogen resides in an anti-bonding position. Donor-hydrogen complexes have not been detected in GaN, despite high concentrations (10^{19} cm^{-3}) of donors in MOCVD-grown epilayers. The investigation of donor- and acceptor-hydrogen complexes in GaN is a promising avenue of research.

LVM-phonon interactions will undoubtedly manifest themselves in other semiconductors. One unanswered question is: which phonons in the Brillouin zone interact most strongly with LVMs? The interaction between the defect and the lattice may arise from the deformation of the defect's environment by a lattice wave. In addition, optical phonons produce macroscopic electric fields that may interact with the dipole moment of a hydrogen-related complex. The combination of these factors and the multi-phonon density of states may yield sharp resonances that produce the distinct localons observed in AlSb:Se,H.

8. Appendices

Appendix A: Group Theory

A.1 Introduction

In examining the normal modes of a system, group theory is often employed as a method to determine the symmetries of the modes as well as their optical activity. The first step is to establish the symmetry of the complex. This is done by listing all the symmetry operations - rotations, reflections, and inversions - which leave the complex invariant. For systems such as perfect crystals which have translational invariance, space groups must be considered (Falicov 1966). In this thesis, however, I am concentrating on point defects, which necessarily break translational symmetry. All the operations are performed about a point, and a group of such operations is known as a *point group.*

The elements of a group can be represented by a basis of matrices. The identity element, for example, is a member of every group and in a two dimensional representation it is written

$$E = \begin{bmatrix} 1 & 0 \\ 0 & 1 \end{bmatrix}. \tag{A.8.1}$$

A rotation by 120° is written

$$C_3 = \begin{bmatrix} \cos 2\pi/3 & -\sin 2\pi/3 \\ \sin 2\pi/3 & \cos 2\pi/3 \end{bmatrix} \tag{A.8.2}$$

and a reflection about the x axis is written

$$\sigma_v = \begin{bmatrix} 1 & 0 \\ 0 & -1 \end{bmatrix}. \tag{A.8.3}$$

For a list of operations, groups and their labels, see Colton (1990).

The elements of a group can be represented by irreducible matrices of any dimension, so long as they obey the properties of the group. The properties of a group are:

1.) *Closure*. The product of any two elements in a group is another element in the group. Two successive rotations by 120°, for example, produce a rotation of 240°.

2.) *Identity*. The identity element, commonly labeled E, must be in any group.

3.) *Associativity*. $a(bc) = (ab)c$.

4.) *Reciprocity*. Every element a must have a reciprocal a^{-1} in the group, such that $aa^{-1}=E$.

A.2 Irreducible Representations

One can imagine creating any number of huge matrices which obey the four rules above. The requirement that the matrices be irreducible, however, limits the number of possible basis sets. A group of reducible matrices is defined as matrices which, upon a unitary transformation, can be written in block-diagonal form, such as:

$$A = \begin{bmatrix} [A_1] & 0 \\ 0 & [A_2] \end{bmatrix}. \tag{A.4}$$

The matrices which occupy the diagonal positions are themselves elements of the group and obey all the properties. If we find a set of matrices that cannot be reduced into this block-diagonal form, then they are said to be *irreducible*.

A.3 Character Table

Every group has a *character table*, in which the traces of the irreducible representations are listed. Each row corresponds to a different irreducible representation. The first row is simply filled with 1's, since the set of 1's obey all the properties of a group. Successive rows contain more interesting representations. Each column in the character table corresponds to a class of operations (e.g., rotations), and the number before the label refers to the number of elements in that class. The first column is E, the identity element, which has a trace equal to its dimension.

When a molecule begins to vibrate, its symmetry is lowered in a specific way which is given by the irreducible representation. As an important example, the character table of the C_{3v} (trigonal) group is shown in Table A.1. The chemists' notation is shown in parentheses. In addition to the identity element, the C_{3v} group has two threefold rotations (120° and 240°) labeled C_3 and three reflections about vertical planes labeled σ_v.

Table A.1. Character table of the C_{3v} group.

C_{3v}	E	$2C_3$	$3\sigma_v$
$\Gamma_1 (A_1)$	1	1	1
$\Gamma_2 (A_2)$	1	1	-1
$\Gamma_3 (E)$	2	-1	0

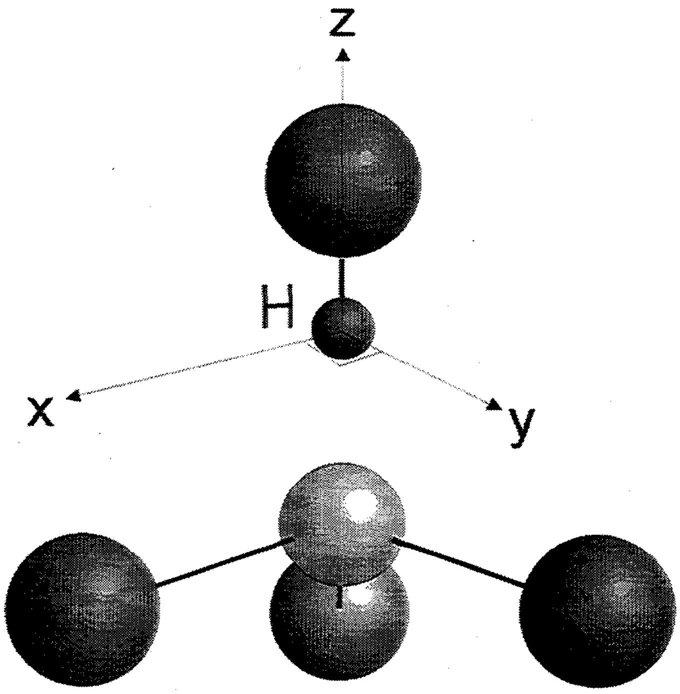

Figure A.1. Example of a hydrogen complex with C_{3v} symmetry.

A.4 Hydrogen Motion in C_{3v} Symmetry

Now we want to find the normal modes of a hydrogen atom in an environment which possesses C_{3v} symmetry. We choose the basis to be the Cartesian coordinates centered at the hydrogen atom (Fig. A.1), with the z axis pointing toward the nearest neighbor. To determine the normal modes, we use a *projection operator*, defined as

$$\hat{P}^j = \frac{l_j}{h}\sum_R \chi(R)^j \hat{R} \tag{A.5}$$

where j is the representation, l_j is the dimension of the representation, h is the order (number of elements) in the group, χ is the character, and R is the element. When the projection operator is applied to a function, only the part of the function which transforms as the representation j survives. When we apply $\hat{P}^{\Gamma_1}$ to the function z, we get

$$\hat{P}^{\Gamma_1}(z) = \frac{1}{6}(z+z+z+z+z+z) = z \tag{A.6}$$

Since z is invariant under all operations of the C_{3v} group, it belongs to the Γ_1 representation. If we operate on z with either $\hat{P}^{\Gamma_2}$ or $\hat{P}^{\Gamma_3}$, the result will be zero. The Γ_1 mode is called the hydrogen *stretch mode* and it corresponds to a vibration along the z axis.

Applying the $\hat{P}^{\Gamma_1}$ operator to x yields

$$\hat{P}^{\Gamma_1}(x) = \frac{1}{6}\left(x + \left(-\tfrac{1}{2}x + \tfrac{\sqrt{3}}{2}y\right) + \left(-\tfrac{1}{2}x - \tfrac{\sqrt{3}}{2}y\right) + x + \left(-\tfrac{1}{2}x - \tfrac{\sqrt{3}}{2}y\right) + \left(-\tfrac{1}{2}x + \tfrac{\sqrt{3}}{2}y\right)\right) = 0 \tag{A.7}$$

Similarly, applying the $\hat{P}^{\Gamma_2}$ operator to x yields zero. Applying the $\hat{P}^{\Gamma_3}$ operator to x

yields

$$\hat{P}^{\Gamma_3}(x)=\frac{2}{6}\left(2x-\left(-\tfrac{1}{2}x+\tfrac{\sqrt{3}}{2}y\right)-\left(-\tfrac{1}{2}x-\tfrac{\sqrt{3}}{2}y\right)\right)=x \tag{A.8}$$

The x function is therefore a member of the Γ_3 representation. Applying the $\hat{P}^{\Gamma_3}$ operator to y verifies that it also belongs to the E representation. Since x and y transform into each other under rotations and reflections, they are degenerate. Vibrations in the x-y plane are called *wag modes*.

A.5 Selection Rules

Group theory can determine which matrix elements are zero. Consider the matrix element

$$\langle\Gamma_k|\Gamma_l|\Gamma_m\rangle\equiv\int d^3r\,\Gamma_k(\mathbf{r})\Gamma_l(\mathbf{r})\Gamma_m(\mathbf{r}), \tag{A.9}$$

where the Γ_i's are functions with symmetries given by the Γ_i representations. Products of functions with certain symmetries will integrate to zero. For example, in an environment where parity is a good quantum number, the integral of two even functions times an odd function is always zero. The selection rules can be generalized by expressing the *direct product* $\Gamma_k\otimes\Gamma_l\otimes\Gamma_m$ as a direct sum of irreducible representations (Falicov 1966):

$$\Gamma_k\otimes\Gamma_l\otimes\Gamma_m=\Gamma_i\oplus\Gamma_j\oplus\ldots \tag{A.10}$$

To obtain the irreducible representations Γ_i, Γ_k, etc., we first multiply the characters of Γ_k, Γ_l, and Γ_m, column by column. Then, we find a set of representations which add up to the products. Those representations are Γ_i, Γ_j, etc. If one of the representations is Γ_1, the fully symmetric representation, then the integral may be nonzero. Otherwise, it is definitely zero.

As an example, consider the selection rules for an optical transition from the ground state to an excited vibrational mode. The ground state has the fully symmetric representation Γ_1. As described in the previous section, the stretch mode has a representation Γ_1. Light polarized along the z direction also has Γ_1 symmetry. The direct product is determined by multiplying the characters:

Table A.2.

C_{3v}	E	$2C_3$	$3\sigma_v$
$\Gamma_1 \otimes \Gamma_1 \otimes \Gamma_1$	1	1	1

By inspection,

$$\Gamma_1 \otimes \Gamma_1 \otimes \Gamma_1 = \Gamma_1, \tag{A.11}$$

so the transition is allowed. In a zincblende or diamond crystal, there are four equivalent [111] directions, so for randomly oriented complexes, light of any polarization will excite a stretch mode.

Next, consider a wag mode, which has Γ_3 symmetry. Light polarized in the x-y plane also has Γ_3 symmetry. Multiplying the characters yields

Table A.3.

C_{3v}	E	$2C_3$	$3\sigma_v$
$\Gamma_1 \otimes \Gamma_3 \otimes \Gamma_3$	4	1	0

By inspection, we find that

$$\Gamma_1 \otimes \Gamma_3 \otimes \Gamma_3 = \Gamma_1 \oplus \Gamma_2 \oplus \Gamma_3 , \tag{A.12}$$

which contains Γ_1, so the transition is allowed. We can also show that

$$\Gamma_1 \otimes \Gamma_1 \otimes \Gamma_2 = \Gamma_2 \tag{A.13}$$

$$\Gamma_1 \otimes \Gamma_3 \otimes \Gamma_2 = \Gamma_3 \tag{A.14}$$

so that the $\Gamma_1 \rightarrow \Gamma_2$ transition is dipole-forbidden.

A.6 Perturbation Theory

In second order perturbation theory, states can interact via a matrix element $\langle \Gamma_k | \delta H | \Gamma_l \rangle$, where δH is a perturbation due to the surrounding atoms and has symmetry Γ_1. The direct product is given by

$$\Gamma_k \otimes \Gamma_1 \otimes \Gamma_l = \Gamma_k \otimes \Gamma_l \tag{A.15}$$

The product will only contain Γ_1 if $\Gamma_k = \Gamma_l$. In other words, states only interact if they have the same symmetry.

Table B.1. Wag modes in C_{3v} symmetry.

N	Symmetry	Wavefunction(s)
0	Γ_1	$\lvert 0,0\rangle$
1	Γ_3	$\lvert 1,0\rangle;\lvert 0,1\rangle$
2	Γ_1	$\frac{1}{\sqrt{2}}\left(\lvert 2,0\rangle+\lvert 0,2\rangle\right)$
2	Γ_3	$\frac{1}{\sqrt{2}}\left(\lvert 2,0\rangle-\lvert 0,2\rangle\right);\lvert 1,1\rangle$
3	Γ_1	$\frac{1}{2}\left(\lvert 3,0\rangle-\sqrt{3}\lvert 1,2\rangle\right)$
3	Γ_2	$\frac{1}{2}\left(\lvert 0,3\rangle-\sqrt{3}\lvert 2,1\rangle\right)$
3	Γ_3	$\frac{1}{2}\left(\lvert 0,3\rangle+\sqrt{3}\lvert 2,1\rangle\right);\frac{1}{2}\left(\lvert 0,3\rangle+\sqrt{3}\lvert 1,2\rangle\right)$
4	Γ_1	$\sqrt{\frac{3}{8}}\left(\lvert 4,0\rangle+\lvert 0,4\rangle\right)+\frac{1}{2}\lvert 2,2\rangle$
4	$\Gamma_3^{(1)}$	$\frac{1}{\sqrt{2}}\left(\lvert 3,1\rangle+\lvert 1,3\rangle\right);\frac{1}{\sqrt{2}}\left(\lvert 4,0\rangle-\lvert 0,4\rangle\right)$
4	$\Gamma_3^{(2)}$	$\sqrt{\frac{1}{8}}\left(\lvert 4,0\rangle+\lvert 0,4\rangle\right)-\sqrt{\frac{3}{4}}\lvert 2,2\rangle;\frac{1}{\sqrt{2}}\left(\lvert 3,1\rangle-\lvert 1,3\rangle\right)$
5	Γ_1	$\frac{1}{4}\left(\sqrt{5}\lvert 5,0\rangle-\sqrt{2}\lvert 3,2\rangle-3\lvert 1,4\rangle\right)$
5	Γ_2	$\frac{1}{4}\left(\sqrt{5}\lvert 0,5\rangle-\sqrt{2}\lvert 2,3\rangle-3\lvert 4,1\rangle\right)$
5	$\Gamma_3^{(1)}$	$\sqrt{\frac{1}{8}}\left(\sqrt{5}\lvert 5,0\rangle+\sqrt{2}\lvert 3,2\rangle+\lvert 1,4\rangle\right);\sqrt{\frac{1}{8}}\left(\sqrt{5}\lvert 0,5\rangle+\sqrt{2}\lvert 2,3\rangle+\lvert 4,1\rangle\right)$
5	$\Gamma_3^{(2)}$	$\frac{1}{4}\left(\lvert 5,0\rangle-\sqrt{10}\lvert 3,2\rangle+\sqrt{5}\lvert 1,4\rangle\right);\frac{1}{4}\left(\lvert 0,5\rangle-\sqrt{10}\lvert 2,3\rangle+\sqrt{5}\lvert 4,1\rangle\right)$

Appendix B: Calculation of Wag Modes in C_{3v} symmetry.

B.1 Two Dimensional Wavefunctions

I now apply the results from Appendix A to wag modes in a C_{3v} potential. Wag modes are oscillations primarily in the x-y plane, and the wavefunctions are given by (Sec. 2.1.2)

$$\left|n_x\, n_y\right\rangle = \psi_{n_x}(x)\psi_{n_y}(y), \tag{B.1}$$

with an energy

$$E = (n_x + n_y + 1)\hbar\omega \equiv (N + 1)\hbar\omega, \tag{B.2}$$

where $N = n_x + n_y$ is the principal quantum number. For a perfectly parabolic potential, all states with the same N are degenerate. When a C_{3v} perturbation is introduced, however, the states split according to their symmetries. Using the methods outlined in Appendix A, I derived the states up to $N = 5$ (Table B.1). Different states with the same symmetry and N value are differentiated by a subscript in parentheses.

B.2 Anharmonic Terms

To quantitatively estimate the splittings, the C_{3v} potential is approximated by (Newman 1969; Sciacca *et al.*, 1995)

$$V(x,y) = \frac{1}{2}k\left(x^2 + y^2\right) + B\left(xy^2 - x^3/3\right) + C\left(x^2 + y^2\right)^2 + \cdots \quad , \tag{B.3}$$

where x and y are parallel to the $[1\bar{1}0]$ and $[11\bar{2}]$ crystallographic axes, respectively. The cubic term shifts the energy of a state $\left|N,\Gamma\right\rangle$ via second order perturbation theory:

Table B.2. Matrix Elements of cubic and quartic terms in Eq. B.3.

Cubic Terms	Quartic Terms
	$\langle N=0,\Gamma_1\vert V_4\vert N=0,\Gamma_1\rangle = 2$
$\langle N=1,\Gamma_3\vert V_3\vert N=2,\Gamma_3\rangle = 1/\sqrt{2}$	$\langle N=1,\Gamma_3\vert V_4\vert N=1,\Gamma_3\rangle = 6$
$\langle N=2,\Gamma_1\vert V_3\vert N=3,\Gamma_1\rangle = -\sqrt{3}$	$\langle N=2,\Gamma_1\vert V_4\vert N=2,\Gamma_1\rangle = 14$
$\langle N=2,\Gamma_3\vert V_3\vert N=3,\Gamma_3\rangle = -1$	$\langle N=2,\Gamma_3\vert V_4\vert N=2,\Gamma_3\rangle = 12$
$\langle N=3,\Gamma_1\vert V_3\vert N=4,\Gamma_1\rangle = \sqrt{3}$	$\langle N=3,\Gamma_1\vert V_4\vert N=3,\Gamma_1\rangle = 20$
$\langle N=3,\Gamma_3\vert V_3\vert N=4,\Gamma_3^{(1)}\rangle = \sqrt{3}$	$\langle N=3,\Gamma_2\vert V_4\vert N=3,\Gamma_2\rangle = 20$
$\langle N=3,\Gamma_3\vert V_3\vert N=4,\Gamma_3^{(2)}\rangle = \sqrt{3}$	$\langle N=3,\Gamma_3\vert V_4\vert N=3,\Gamma_3\rangle = 24$
$\langle N=4,\Gamma_1\vert V_3\vert N=5,\Gamma_1\rangle = -2\sqrt{3}$	$\langle N=4,\Gamma_1\vert V_4\vert N=4,\Gamma_1\rangle = 38$
$\langle N=4,\Gamma_3^{(1)}\vert V_3\vert N=5,\Gamma_3^{(1)}\rangle = -3/\sqrt{2}$	$\langle N=4,\Gamma_3^{(1)}\vert V_4\vert N=4,\Gamma_3^{(1)}\rangle = 36$
$\langle N=4,\Gamma_3^{(1)}\vert V_3\vert N=5,\Gamma_3^{(2)}\rangle = \sqrt{5}$	$\langle N=4,\Gamma_3^{(2)}\vert V_4\vert N=4,\Gamma_3^{(2)}\rangle = 30$
$\langle N=4,\Gamma_3^{(2)}\vert V_3\vert N=5,\Gamma_3^{(1)}\rangle = -\sqrt{2}$	
$\langle N=4,\Gamma_3^{(2)}\vert V_3\vert N=5,\Gamma_3^{(2)}\rangle = 0$	
$\langle N=5,\Gamma_1\vert V_3\vert N=6,\Gamma_1^{(1)}\rangle = 2\sqrt{3}$	$\langle N=5,\Gamma_1\vert V_4\vert N=5,\Gamma_1\rangle = 50$
$\langle N=5,\Gamma_1\vert V_3\vert N=6,\Gamma_1^{(2)}\rangle = \sqrt{15/2}$	$\langle N=5,\Gamma_2\vert V_4\vert N=5,\Gamma_2\rangle = 50$
$\langle N=5,\Gamma_2\vert V_3\vert N=6,\Gamma_2\rangle = \sqrt{15/2}$	$\langle N=5,\Gamma_3^{(1)}\vert V_4\vert N=5,\Gamma_3^{(1)}\rangle = 54$
$\langle N=5,\Gamma_3^{(1)}\vert V_3\vert N=6,\Gamma_3^{(1)}\rangle = 3$	$\langle N=5,\Gamma_3^{(2)}\vert V_4\vert N=5,\Gamma_3^{(2)}\rangle = 42$
$\langle N=5,\Gamma_3^{(1)}\vert V_3\vert N=6,\Gamma_3^{(2)}\rangle = 3$	
$\langle N=5,\Gamma_3^{(2)}\vert V_3\vert N=6,\Gamma_3^{(1)}\rangle = -\sqrt{5/2}$	
$\langle N=5,\Gamma_3^{(2)}\vert V_3\vert N=6,\Gamma_3^{(2)}\rangle = \sqrt{5/2}$	

The integrals of polynomials times Gaussians are given by the recursion relations:

$$\int_{-\infty}^{\infty} e^{-x^2}\,dx = \sqrt{\pi} \tag{B.7}$$

$$\int_{-\infty}^{\infty} x^{2n} e^{-x^2}\,dx = \frac{2n-1}{2}\int_{-\infty}^{\infty} x^{2n-2} e^{-x^2}\,dx$$

Using these formulae and *Mathematica*, I calculated the matrix elements listed in Table B.2.

B.4 Results and Comparison with Experiment

Combining these results, the energy eigenvalues are given by

$$E = \hbar\sqrt{k/\mu}(N+1) + \frac{B^2\hbar^2}{k^2\mu}N_1 + \frac{C\hbar^2}{k\mu}N_2, \tag{B.8}$$

where N_1 and N_2 are different for each state and are listed in Table B.3. It is immediately apparent that for $N = 2$, the Γ_1 mode is lower in energy than the Γ_3 mode, contradicting the assumption given by McCluskey *et al.* (1996b), and in agreement with experimental results by Zheng and Stavola (1995). The $N = 2$ modes are split by an amount given by

$$\Delta = \frac{5B^2\hbar^2}{2k^2\mu} - \frac{2C\hbar^2}{k\mu}. \tag{B.9}$$

For the $N = 3$ modes, the Γ_1 mode is higher in energy than the Γ_3 mode, and the splitting is 2Δ. This is in qualitative agreement with the experimental results, in which the $N = 3$ splitting is greater than the $N = 2$ splitting. However, the experimental ratio of the splittings is ~1.5, so clearly the approximation is somewhat crude. For the $N = 4$ modes, the Γ_1 and $\Gamma_3^{(1)}$ modes split by Δ, again in qualitative agreement with experiment. A schematic of the level splittings is shown in Figure 4.16. In the future, the inclusion of wag-stretch coupling terms in Eq. B.3 should help agreement between theory and experiment.

Eq. B.8 can be written in a simpler form:

$$E(\text{cm}^{-1}) = \sqrt{k/\mu}\,(N+1) + \frac{B'}{\mu}N_1 + \frac{C'}{\mu}N_2, \qquad \text{(B.10)}$$

where k, B', and C' are adjustable parameters and the reduced mass μ is given in units of amu. The hydrogen is assumed to be attached to an aluminum atom ($M = 27$). The parameters that yielded the best least squares fit are $k = 1.156 \text{ X } 10^6 \text{ cm}^{-2}$ amu, $B' = 8.915 \text{ cm}^{-1}$ amu, and $C' = 0.0674 \text{ cm}^{-1}$ amu. With only three adjustable parameters, the agreement between experiment and theory is fairly good (Table B.3).

Table B.3. Theoretical values of Se-H and Se-D wag modes in AlSb.

N	Symmetry	N_1	N_2	$0 \rightarrow N$ transition (cm^{-1})			
0	Γ_1	0	2	H (theory)	H(expt)	D(theory)	D(expt)
1	Γ_3	-1/2	6	342		247	
2	Γ_1	-3	14	666	666	484	478
2	Γ_3	-1/2	12	689	692	496	497
3	Γ_1	0	20	1040	1032	748	742
3	Γ_2	0	20	“		“	
3	Γ_3	-5	24	994	993	724	718
4	Γ_1	-9	38	1304	1316	955	948
4	$\Gamma_3^{(1)}$	-13/2	36	1327	1333	967	957
4	$\Gamma_3^{(2)}$	1	30	1396		1002	
5	Γ_1	-15/2	50	1665		1212	
5	Γ_2	-15/2	50	“		“	
5	$\Gamma_3^{(1)}$	-23/2	54	1629		1193	
5	$\Gamma_3^{(2)}$	0	42	1735		1247	

9. References

Ahlburn, B.T. and A.K. Ramdas, 1968, Phys. Rev. **167**, 717.

Alt, H. Ch. and B. Dischler, 1995, Appl. Phys. Lett. **66**, 61.

Ashwin, M.J., B.R. Davidson, K. Woodhouse, R.C. Newman, T.J. Bullough, T.B. Joyce, R. Nicklin, and R.R. Bradley, 1993, Semicond. Sci. Tech. **8**, 625.

Barker, A.S. Jr. and A. J. Sievers, 1975, Reviews of Modern Physics **47**, Suppl. No. **2**.

Becla, P., A. Witt, J. Lagowski, and W. Walukiewicz, 1995, Appl. Phys. Lett. **67**, 395.

Belak, J., R. Lesar, and R.D. Etters, 1990, J. Chem. Phys. **92**, 5430.

Bell, R.J., 1972, Introductory Fourier Transform Spectroscopy (Academic Press, New York).

Bergman, K., M. Stavola, S.J. Pearton, and J. Lopata, 1988, Phys. Rev. B **37**, 2770.

Betts, D.D., A.B. Bhatia, and M. Wyman, 1956, Phys. Rev. **104**, 37.

Boening, H.V., 1982, Plasma Science and Technology (Cornell Univ. Press, Ithaca, NY).

Bourret-Courchesne, E.D., 1996, Appl. Phys. Lett. **68**, 2481.

Braun, E. and S. MacDonald, 1978, Revolution in Miniature (Cambridge University Press), Ch. 8.

Briddon, P.R. and R. Jones, 1991, Physica B **170**, 413.

Brockhouse, B.N. and P.K. Iyengar, 1958, Phys. Rev. **111**, 747.

Cardona, M., 1982, in Light Scattering in Solids II, edited by M. Cardona and G. Guntherodt (Springer-Verlag).

Cardona, M. and F.H. Pollak, 1966, Phys. Rev. **142**, 530.

Chadi, D.J. and M.L. Cohen, 1975, Phys. Stat. Solidi B **68**, 405.

Chang, K.J., B.H. Cheong, and C.H. Park, 1992, Solid St. Comm. **84** 1005.

Chen, R.J. and B.A. Weinstein, 1996, Rev. Sci. Instr. **67**, 2883.

Chevallier, J., W.C. Dautremont-Smith, C.W. Tu, and S.J. Pearton, 1985, Appl. Phys. Lett. **47**, 108.

Chevallier, J., A. Jalil, R. Azoulay, and A. Mircea, 1986, Materials Science Forum **10-12**, 591.

Chevallier, J., B. Clerjaud, and B. Pajot, 1991, in Semiconductors and Semimetals, edited by J. I. Pankove and N. M. Johnson (Academic Press, Orlando), Vol. **34**, Ch. 13.

Cho, H.Y., S.-K. Min, K.J. Chang and C. Lee, 1991, Phys. Rev. B **44**, 1991.

Clerjaud, B., F. Gendron, M. Krause, and W. Ulrici, 1990, Phys. Rev. Lett. **65**, 1800.

Clerjaud, B., D. Côte, W.-S. Hahn, and W. Ulrici, 1991, Appl. Phys. Lett. **58**, 1860.

Clerjaud, B., D. Côte, W.-S. Hahn, and D. Wasik, 1992, Appl. Phys. Lett. **60**, 2374.

Cohen, M.L. and V. Heine, 1976, in Solid State Physics (Holt, Rinehart, and Winston, New York), 202.

Colton, F.A., Chemical Applications of Group Theory (3rd edition, John Wiley & Sons, 1990).

Cooley, J.W. and J.W. Tukey, 1965, Math. Computat. **19**, 297.

Darwich, R., B. Pajot, B. Rose, D. Robein, B. Theys, R. Rahbi, C. Porte, and F. Gendron, 1993, Phys. Rev. B **48**, 17776.

Debye, P., 1912, Ann. Phys. **39**, 789.

DeLeo, G.G. and W.B. Fowler, 1985, J. Elect. Mater. **14a**, 745.

Dischler, B., F. Fuchs, and H. Seelewind, 1991, Physica B **170**, 245.

Einstein, A., 1907, Ann. Phys. (4) **22**, 180, 800.

Elliot, R.J., W. Hayes, G.D. Jones, H.F. MacDonald, and C.T. Sennet, 1965, Proc. R. Soc. Lond. **A289** 1.

Estreicher, S.K., L. Throckmorton, and D.S. Marynick, 1989, Phys. Rev. B **39**, 13241.

Falicov, L.M., 1966, Group Theory and its Physical Applications (The University of Chicago Press).

Forman, R.A., G.J. Piermarini, J.D. Barnett, and S. Block, 1972, Science **176**, 284.

Frölich, H., H. Pelzer, and S. Zienau, 1950, Phil. Mag. **41**, 221.

Gasiorowicz, S., 1974, Quantum Physics (John Wiley & Sons), 127.

Götz, W., N.M. Johnson, D.P. Bour, M.D. McCluskey, and E.E. Haller, 1996, Appl. Phys. Lett. **69**, 3725.

Grosche, E.G., M.J. Ashwin, R.C. Newman, D.A. Robbie, M.J.L. Sangster, T. Pletl, P. Pavone, and D. Strauch, 1995, Phys. Rev. B **51**, 14758.

Haller, E.E., 1978, Phys. Rev. Lett. **40**, 584.

Haller, E.E., 1991, in Semiconductors and Semimetals, edited by J. I. Pankove and N. M. Johnson (Academic Press, Orlando, FL, 1991), Vol. **34**, Ch. 11.

Haller, E.E., 1994, in Handbook on Semiconductors, edited by S. Mahajan (North-Holland, Amsterdam), Vol. **3b**, Ch. 20, p. 1515.

Haller, E.E., 1995, in MRS Proc. Vol. **378**.

Haller, E.E. *et al.*, 1974a, IEEE Trans. Nucl. Sci. **NS-21**, No.1, 279.

Haller, E.E. and W.L. Hansen, 1974b, Solid State Commun. **15**, 687.

Haller, E.E. *et al.*, 1975, IEEE Trans. Nucl. Sci. **NS-22**, No.1, 127.

Haller, E.E. *et al.*, 1977, IEEE Trans. Nucl. Sci. **NS-24**, No.1, 48.

Haller, E.E., B. Jóos, and L.M. Falicov, 1980, Phys. Rev. B **21**, 4729.

Hamann, D.R., M. Schleuter, and C. Chiang, 1979, Phys. Rev. Lett. **43**, 1494.

Hayes, W., M.C.K. Wiltshire, and P.J. Dean, 1970, J. Phys. C **3**, 1762.

Herrero, C.P. and M. Stutzmann, 1988, Solid State Commun. **68**, 1085.

Herring, C., 1940, Phys. Rev. **57**, 1169.

Irwin, J.C. and L. LaCombe, 1974, Journal of Applied Physics **45**, 567.

Jackson, J.D., 1975, Classical Electrodynamics (2nd edition, John Wiley & Sons).

Jayaraman, A., 1983, Rev. Modern Phys. **55**, 65.

Jodl, H.J., H.W. Löwen, and D. Griffith, 1987, Solid St. Commun. **61**, 503.

Johnson, N.M., 1985, Phys. Rev. B **31**, 5525.

Johnson, N.M., 1991, Semiconductors and Semimetals, edited by N.M. Johnson and J.I. Pankove, **34** (Academic Press, Inc.), Ch. 7.

Johnson, N.M., R.D. Burnham, R.A. Street, and R.L. Thornton, 1985, Phys. Rev. B **33**, 1102.

Johnson, N.M., C. Herring, and C.G. van de Walle, 1995, in 22nd International Conference on the Physics of Semiconductors, edited by D.J. Lockwood, **3** (World Scientific, Singapore), 2227.

Joós, B., E.E. Haller, and L.M. Falicov, 1980, Phys. Rev. B **22**, 832.

Jost, W., M. Kunzer, U. Kaufmann, and H. Bender, 1994, Phys. Rev. B **50**, 4341

Kahn, J.M., L.M. Falicov, and E.E. Haller, 1986, Phys. Rev. Lett. **57**, 2077.

Kahn, J.M., R.E. McMurray, Jr., E.E. Haller, and L.M. Falicov, 1987, Phys. Rev. B **36**, 8001.

Kamata, A., H. Mitsuhashi, and H. Fujita, 1993, Appl. Phys. Lett. **63**, 3353.

Kaufman, F., 1969, in Chemical Reactions in Electric Discharges, edited by B.D. Blaustein (Amer. Chem. Soc., Washington, D.C.), Ch. 3.

Kerker, G., 1980, J. Phys. C **13**, L189.

Kittel, C. and A.H. Mitchell, 1954, Phys. Rev. **96**, 1488.

Kittel, C., 1966, in Phonons, edited by R.W.H. Stevenson (Plenum, New York), Ch. 1.

Kittel, C., 1986, Introduction to Solid State Physics (6th edition, John Wiley & Sons), 101.

Kogan, Sh. M. and T.M. Lifshits, 1977, Phys. Stat. Sol. (a) **39**, 11.

Kohn, W., 1957, in Solid State Physics, Vol. **5**, edited by F. Seitz and D. Turnbull (Academic Press, New York), 256.

Kozuch, D.M., M. Stavola, S.J. Pearton, C.R. Abernathy, and W.S. Hobson, 1993, Journ. Appl. Phys. **73**, 3716.

Krönig, R. de L. and W.J. Penney, 1930, Proc. Roy. Soc. London **A130**, 499.

Landolt-Börnstein, New Series III, 1987, Semiconductors: Intrinsic Properties of Group IV Elements and III-V, II-VI and I-VII Compounds, edited by O. Madelung, Vol. **22a** (Springer-Verlag, Berlin).

Lang, D.V. and R.A. Logan, 1977, Phys. Rev. Lett. **39**, 635.

Lannoo, M. and J. Bourgoin, 1981, Point Defects in Semiconductors I (Springer-Verlag, Berlin) 62.

Leitch, A.W.R., Th. Prescha and J. Weber, 1991, Phys. Rev. B **44**, 1375.

Li, M. Ming, D.J. Strachan, T.M. Ritter, M. Tamargo, and B.A. Weinstein, 1994, Phys. Rev. B **50**, 4385.

Lifshits, T.M. and F. Yd. Nad, 1965, Soviet Phys. Dokl. **10**, 532.

Louie, S.G., S. Froyen, and M.L. Cohen, 1977, Phys. Rev. B **26**, 1738.

Löwen, H.W., K.D. Bier, and H.J. Jodl, 1990, J. Chem Phys. **93**, 8565.

Luttinger, J.M. and W. Kohn, Phys. Rev. **97**, 869.

Mao, H.K., P.M. Bell, J.W. Shaner, and D.J. Steinberg, 1978, J. Appl. Phys. **49**, 3276.

McCluskey, M.D., E.E. Haller, J. Walker, and N.M. Johnson, 1994a, Appl. Phys. Lett. **65**, 2191.

McCluskey, M.D., E.E. Haller, J. Walker, and N.M. Johnson, 1994b, Inst. Phys. Conf. Proc. Ser. No 141:**Ch. 3** (Int. Symp. Compound Semicond., San Diego).

McCluskey, M.D., E.E. Haller, J. Walker, and N.M. Johnson, 1995, Phys. Rev. B **52**, 11859.

McCluskey, M.D., E.E. Haller, F.X. Zach, and E.D. Bourret-Courchesne, 1996a, Appl. Phys. Lett. **68**, 3476.

McCluskey, M.D., E.E. Haller, W. Walukiewicz, and P. Becla, 1996b, Phys. Rev. B **53**, 16297.

McCluskey, M.D., L. Hsu, L. Wang, and E.E. Haller, 1996c, Phys. Rev. B **54**, 8962.

McCluskey, M.D., W. Walukiewicz, E.E. Haller, and P. Becla, 1997, submitted to Phys. Rev. Lett.

McMurray, Jr., R.E., N.M. Haegel, J.M. Kahn, and E.E. Haller, 1987, Sol. State Commun. **61**, 27.

McQuaid, S.A., M.J. Binns, R.C. Newman, E.C. Lightowlers, and J.B. Clegg, 1993, Appl. Phys. Lett. **62**, 1612.

Medina, F.D. and W.B. Daniels, 1976, J. Chem. Phys. **64**, 150.

Merrill, L. and W.A. Bassett, 1974, Rev. Sci. Instr. **45**, 290.

Mills, R.L., B. Olinger, and D.T. Cromer, 1986, J. Chem Phys. **84**, 2837.

Mizuta, M., M. Tachikawa, H. Kukimoto, and S. Minomura, 1985, Jpn. J. Appl. Phys. **24**, L143.

Morimoto, K. and T. Fujino, 1993, Appl. Phys. Lett. **63**, 2384.

Morse, P.M., 1929, Phys. Rev. Lett. **34**, 57.

Moss, T.S., and T.D. Hawkins, 1962, Infrared Phys. **1**, 111.

Nakayama, M., 1969, Journ. Phys. Soc. Japan **27**, 636.

Nelson, R.J., 1977, Appl. Phys. Lett. **31**, 351.

Neugebauer, J. and C.G. van de Walle, 1995, Phys. Rev. Lett. **75**, 4452.

Newman, R.C., 1969, Adv. Phys. **18**, 545.

Newman, R.C. and W.W. Tyler, 1959, in Solid State Physics, Vol. **8**, edited by F. Seitz and D. Turnbull (Academic, New York) 49.

Nishimura, K., Y. Nagao, and K. Sakai, 1993, in Low pressure growth and nitrogen doping in metal organic vapor phase epitaxy of ZnSe, II-VI Conference.

Nosé, S. and M. Klein, 1983, Phys. Rev. Lett. **50**, 1207.

Ohkawa, K., T. Karasawa, and T. Mitsuyu, 1992, Jpn. J. Appl. Phys. **30**, L152.

Pajot, B., A. Chari, M. Aucouturier, M. Astier, and A. Chantre, 1988, Solid State Commun. **67**, 855.

Pankove, J.I., D.E. Carlson, J.E. Berkeyheiser and R.O. Wance, 1983, Phys. Rev. Lett. **51**, 2224.

Pankove, J.I., R.O. Wance, and J.E. Berkeyheiser, 1984, Appl. Phys. Lett. **45**, 1100.

Pankove, J.I., P.J. Zanzucchi, C.W. Magee, and G. Lucovsky, 1985, Appl. Phys.

Lett. **46**, 421.

Park, R.M., M.B. Troffer, C.M. Rouleau, J.D. DePuydt, and M.A. Haase, 1990, Appl. Phys. Lett. **57**, 2127.

Pearton, S.J., J.W. Corbett, and M. Stavola, 1992, Hydrogen in Crystalline Semiconductors, Springer Series in Materials Science **16** (Springer-Verlag).

Piermarini, G.J., S. Block, J.D. Barnett, and R.A. Forman, 1975, J. Appl. Phys. **46**, 2774.

Phillips, J.C., D. Brust, and F. Bassani, 1962, Proc. Int, Conf. Phys. Semicond., Exeter (The Institute of Physics, London) 564.

Polian, A., P. Loubeyre, and N. Boccara, 1989, Simple Molecular Systems at Very High Density (Plenum, New York).

Rahbi, R., B. Pajot, J. Chevallier, A. Marbeuf, R. C. Logan, and M. Gavand, 1993, J. Appl. Phys. **73**, 1723.

Rahbi, R., B. Theys, R. Jones, B. Pajot, S. Öberg, K. Somogyi, M.L. Fille, and J. Chevallier, 1994, Solid St. Comm. **91**, 187.

Reif, F., 1965, Fundamentals of Statistical and Thermal Physics (McGraw-Hill), 323.

Rosen, B., 1970, International Tables of Selected Constants, Vol. **17** (Pergamon Press, New York).

Sah, C.T., J.Y.C. Sun, and J.J. Tzou, 1983, Appl. Phys. Lett. **43**, 204.

Sakurai, J.J., 1985, Modern Quantum Mechanics (Addison-Wesley), 337.

Schiferl, D., D.T. Cromer, and R.L. Mills, 1978, High Temp. High Pressures **10**, 493.

Schiferl, D., S. Buchsbaum, and R.L. Mills, 1985, J. Phys. Chem. **89**, 2324.

Schiferl, D., R. LeSar, and D.S. Moore, 1989, in Simple Molecular Systems at Very High Density, edited by A. Polian, P. Loubeyre, and N. Boccara (Plenum, New York), p. 303.

Sciacca, M. Dean, A.J. Mayur, N. Shin, I. Miotkowski, A.K. Ramdas, and S. Rodriguez, 1995, Phys. Rev. B **51**, 6971.

Seager, C.H., 1991, Semiconductors and Semimetals, edited by N.M. Johnson and J.I. Pankove, **34** (Academic Press, Orlando), Ch. 2.

Seal, M., 1984, High Temp.-High Press. **16**, 573.

Seeger, K., 1989, Semiconductor Physics, 4th edition (Springer-Verlag, Berlin).

Shimanouchi, T., 1972, Tables of Molecular Vibrational Frequencies Consolidated Volume I, Nat. Stand. Ref. Data Ser., Nat. Bur. Stand. (U.S.), **39**.

Starkoff, T. and J.D. Joannopoulos, 1977, Phys. Rev. B **16**, 5212.

Stavola, M., S.J. Pearton, J. Lopata and W.C. Dautremont-Smith, 1987, Appl. Phys. Lett. **50** 1086.

Sterer, E., M.P. Pasternak, and R.D. Taylor, 1990, Rev. Sci. Instr. **61** 1117.

Tavendale, A.J., S.J. Pearton, A.A. Williams and D. Alexiev, 1990, Appl. Phys. Lett. **56**, 1457.

Thiéry, M.M., D. Fabre, M. Jean-Louis, and H. Vu, 1973, J. Chem. Phys. **59**, 4559.

Tryka, K.A., R.H. Brown, D.P. Cruikshank, T.C. Owen, T.R. Geballe, and C.

DeBergh, 1994, Icarus **112**, 513.

Tryka, K.A., R.H. Brown, and V. Anicich, 1995, Icarus **116**, 409.

Tuncel, E. and H. Sigg, 1993, Phys. Rev. B **48**, 5225.

Van Wieringen, A. and N. Warmoltz, 1956, Physica **22**, 849.

Veloarisoa, I.A., M. Stavola, D.M. Kozuch, R.E. Peale, and G.D. Watkins, 1991, Appl. Phys. Lett. **59**, 2121.

Ves, S., K. Strössner, and M. Cardona, 1986, Solid State Commun. **57**, 483.

Vetterhöffer, J., J.H. Svensson, J. Weber, A.W.R. Leitch, and J.R. Botha, 1994, Phys. Rev. B **50**, 2708.

Watkins, G.D., W.B. Fowler, M. Stavola, G.G. DeLeo, D. Kozuch, S.J. Pearton, and J. Lopata, 1990, Phys. Rev. Lett. **64**, 467.

Watts, R.K., W.C. Holton, and M. de Wit, 1971, Phys. Rev. B **3**, 404.

Williams, P.M., G.D. Watkins, S. Uftring, and M. Stavola, 1993, Phys. Rev. Lett. **70**, 3816.

Wilson, E.B., J.C. Decius, and P.C. Cross, Molecular Vibrations (Dover, 1980).

Wolk, J.A., M.B. Kruger, J.N. Heyman, W. Walukiewicz, R. Jeanloz, and E.E. Haller, 1991, Phys. Rev. Lett. **66**, 774.

Wolk, J.A., 1992, DX Centers in III-V Semiconductors under Hydrostatic Pressure, Ph.D. Thesis, Physics Dept., University of California at Berkeley, unpublished, and Lawrence Berkeley Laboratory, Report No. LBL-33379.

Wolk, J.A., J.W. Ager III, K.J. Duxstad, E.E. Haller, N.R. Taskar, D.R. Dorman, and D.J. Olego, 1993, Appl. Phys. Lett. **63**, 2756.

Yu, P.Y. and M. Cardona,1996, Fundamentals of Semiconductors (Springer-Verlag, Berlin).

Yuan, M.H., L.P. Wang, S.X. Jin, J.J. Chen and G.G. Qin, 1991, Appl. Phys. Lett. **58**, 925.

Zheng, J.-F. and M. Stavola, 1996, Phys. Rev. Lett. **76**, 1154.

Ziman, J.M., Principles of the Theory of Solids (2nd edition, Cambridge University Press, 1972), 30.

Zunger, A. and M.L. Cohen, 1978, Phys. Rev. B **18**, 5449.